Results from the QUIET Q-Band Observing Season

Robert Nicolas Dumoulin

Submitted in partial fulfillment of the
requirements for the degree of
Doctor of Philosophy
in the Graduate School of Arts and Science

COLUMBIA UNIVERSITY
2011

Abstract

Results from the QUIET Q-Band Observing Season

Robert Nicolas Dumoulin

The Q/U Imaging ExperimenT (QUIET) is a ground-based telescope located in the high Atacama Desert in Chile, and is designed to measure the polarization of the Cosmic Microwave Background (CMB) in the Q and W frequency bands (43 and 95 GHz respectively) using coherent polarimeters. From 2008 October to 2010 December, data from more than 10,000 observing hours were collected, first with the Q-band receiver (2008 October to 2009 June) and then with the W-band receiver (until the end of the 2010 observing season).

The QUIET data analysis effort uses two independent pipelines, one consisting of a maximum likelihood framework and the other consisting of a pseudo-C_ℓ framework. Both pipelines employ blind analysis methods, and each provides analysis of the data using large suites of null tests specific to the pipeline. Analysis of the Q-band receiver data was completed in November of 2010, confirming the only previous detection of the first acoustic peak of the EE power spectrum and setting competitive limits on the scalar-to-tensor ratio, r. In this dissertation, the results from the Q-band observing season using the maximum likelihood pipeline will be presented.

Contents

List of Figures

List of Tables

List of Abbreviations

- **Λ-CDM** – Λ **C**old **D**ark **M**atter
- **ADC** – **A**nalog-to-**D**igital **C**onversion
- **AIB** – **A**rray **I**nterface **B**oard
- **APEX** – **A**tacama **P**athfinder **EX**periment
- **AM** – **A**tmospheric **M**odel
- **ATM** – **A**tmospheric **T**ransmission of **M**icrowaves
- **BOOMERanG** – **B**alloon **O**bservations **O**f **M**illimetric **E**xtragalactic **R**adiation **an**d **G**eophysics
- **BICEP** – **B**ackground **I**maging of **C**osmic **E**xtragalactic **P**olarization
- **CAPMAP** – **C**osmic **A**nisotropy **P**olarization **MAP**per
- **CBI** – **C**osmic **B**ackground **I**mager
- **CES** – **C**onstant-**E**levation **S**can
- **COBE** – **CO**smic **B**ackground **E**xplorer
- **CMB** – **C**osmic **M**icrowave **B**ackground
- **DASI** – **D**egree **A**ngular **S**cale **I**nterferometer
- **DIRBE** – **D**iffuse **I**nfra**R**ed **B**ackground **E**xperiment

- **FFT – F**ast **F**ourier **T**ransform
- **FIRAS – F**ar-**I**nfra**R**ed **A**bsolute **S**pectrophotometer
- **FPC – F**lexible **P**rinted **C**ircuits
- **FPGA – F**ield-**P**rogrammable **G**ate **A**rray
- **FWHM – F**ull-**W**idth at **H**alf-**M**aximum
- **GPS – G**lobal **P**ositioning **S**ystem
- **GUT – G**rand **U**nified **T**heory
- **HDPE – H**igh-**D**ensity **P**oly**E**thylene
- **HEMT – H**igh **E**lectron **M**obility **T**ransistor
- **IR – I**nfra-**R**ed
- **KEK – K**ō **E**nerugī **K**asokuki Kenkyū Kikō
- **LDPE – L**ow-**D**ensity **P**oly**E**thylene
- **LNA – L**ow **N**oise **A**mplifier
- **MAB – M**odule **A**ttachment **B**oard
- **MCMC – M**arkov **C**hain **M**onte **C**arlo
- **MMIC – M**onolithic **M**icrowave **I**ntegrated **C**ircuit
- **ML – M**aximum **L**ikelihood

- **MPIfR – M**ax **P**lanck **I**nstitute **f**or **R**adio Astronomy
- **OMT – O**rtho-**M**ode **T**ransducer
- **PC – P**ersonal **C**omputer
- **PCL – P**seudo-C_ℓ
- **PID – P**roportional-**I**ntegral-**D**erivative
- **PTE – P**robability **T**o **E**xceed
- **PTFE – P**oly**T**etra**F**luoroethylen**E**
- **PWV – P**recipitable **W**ater **V**apour
- **QUaD – Q**UEST **a**t **D**ASI
- **QUIET – Q U I**maging **E**xperimen**T**
- **RMS – R**oot **M**ean **S**quare
- **SZA – S**unyaev**Z**el'dovich **A**rray
- **T**au **A – T**aurus **A**
- **UHMW – U**ltra-**H**igh-**M**olecular-**W**eight Polyethylene
- **WMAP – W**ilkinson **M**icrowave **A**nisotropy **P**robe

Acknowledgements

First and foremost, I would like to thank my advisor, Amber Miller. Amber has always taken great interest in the development of her graduate students, sharing her passion and enthusiasm for the field of CMB research; I am deeply indebted to her. I would also like to thank the QUIET Columbia team, which includes Seth Hilbrand, Michele Limon, Laura Newburgh, Ross Williamson and Jonathan Zwart; I have learned so much from all of you in the past years and it has been a pleasure to work so closely with all of you. Also, it has been a great pleasure to recently work with Derek Araujo, an incoming graduate student who will be taking over the QUIET analysis effort at Columbia. I would also like to thank my advisor Amber, Columbia University, and the NSF for providing funding for my research on the QUIET project.

QUIET is a large collaboration, and I would like to thank all of those who have made our project a great success, this includes: Kieran Cleary, Clive Dickinson, Tim Pearson, Simon Radford, Anthony Readhead, Rodrigo Reeves, Joey Richards and Martin Shepherd at the California Institute of Technology; Colin Bishoff, Alison Brizius, Immanuel Buder, Daniel Kapner, Akito Kusaka, Keith Vanderlinde and Bruce Winstein at the University of Chicago; Hogan Nguyen at Fermilab National Accelerator Laboratory; Charles Lawrence, Todd Gaier, Pekka Kangaslahti and Michael Seiffert at JPL; Yuji Chinone, Masaya Hasegawa, Masahi Hazumi and Osamu Tajima at KEK National laboratory in Japan; Dorothea Samtleben at the Max Planck Institute for Radio Astronomy in Bonn; Pedro G. Ferreira, Mike Jones and Joe Zuntz at Oxford University; Glen Nixon, Kendrick Smith and Suzanne Staggs at Princeton University; Sarah Church and Keith Thompson

at Stanford University; Leonardo Bronfman and Jorge May at Universidad de Chile; Lucio Piccirillo at the University of Manchester; Ricardo Bustos, Kevin Huffenberger, Josh Gundersen and Raul Monsalve at the University of Miami; Jeff McMahon at the University of Michigan; and Hans Kristian Eriksen, Sigurd Kirkevold Naess and Ingunn Wehus at the University of Oslo. Of course, there are many other undergraduate and graduate students, post-doctoral research fellows and researchers that have contributed to QUIET that I have not mentioned above; thank you all for your hard work. I would also like to extend my thanks and gratitude to the engineers working at the site in Chile: José Cortés, Cristobal Jara, Freddy Munõz, and Carlos Verdugo. I would like to give special acknowledgment to Bruce Winstein, who was the main PI of QUIET, and who recently died from cancer; Bruce is missed by all of us.

Last, and certainly not least, I would like to thank my mother and father (Patricia and Jean-Guy), and my sisters (Sarah and Katherine) for their support throughout my years as a graduate student. I would also like to thank Andrew Mugler for being the best friend that I could had had throughout my graduate studies, and my niece Ivy and my Irish Terrier Wendy for brightening my days in the past few years.

For my mother and father (Patricia and Jean-Guy),

my sisters (Sarah and Katherine),

my niece and nephew (Ivy and Graham),

and my dog (Wendy).

Chapter 1

The Cosmic Microwave Background

In 1929, observations by Hubble and Humason provided the first experimental evidence of an expanding universe. This discovery led to many important questions, such as: "Has our universe always been expanding? Does this expansion imply that the universe was once much smaller than it is today? When did our universe begin?" In 1931 Lemaître theorized that the expansion of our universe indicated that in the very distant past the entire mass of the universe must have been extremely compact; this theory would later be named the "Big Bang" model of the universe. Robert Dicke, a physicist from Princeton, would later predict that in this incredibly hot and dense state the universe would have acted as a blackbody, and would have left a signature background radiation signal in the microwave waveband. In 1964, the accidental discovery of the signature microwave background radiation signal confirmed certain predictions of the Big Bang model of the universe, and significantly changed both the future study and understanding of cosmology.

In the early 1960s, Bell Laboratories built a six meter horn antenna in Holmdel, NJ as part of a commercial satellite transmission system named "Echo". This antenna was used to collect and amplify radio signals that had travelled from far distances, by bouncing these signals off of metallic balloons high in the atmosphere. The launch of the Telstar communication satellite made the "Echo" system obsolete, freeing up the commercial Holmdel antenna for radio astronomy research. Two astronomers at Bell Laboratories, Arno Penzias and Robert Wilson, used the Holmdel antenna to measure radio signals in the spaces between galaxies [1].

When Penzias and Wilson began making observations they noted a background noise, constant in space and time, which they could not explain. At the same time, Dicke (and two fellow Princeton physicists, Jim Peebles and David Wilkinson) were in the process of preparing to search for the signature microwave background radiation signal predicted by Dicke. Penzias and Wilson recognized that the background noise they had measured could be the the theoretically postulated residual radiation left over from the explosion of the early universe, and called the Dicke team. The Princeton group identified the noise from the Holmdel antenna as the signature microwave signal. The groups jointly published their results in two notes in *The Astrophysical Journal Letters*, marking the first measurement of the cosmic microwave background (CMB) radiation. Penzias and Wilson received the Nobel Prize in Physics in 1978 for their discovery.

1.1 The Origins and Features of the CMB

During the time period of $\sim$10 seconds to 380,000 years after the beginning of the universe, the universe consists of a hot plasma of free protons, free electrons, and photons. During this epoch, the universe is optically thick, and the photons are continually absorbed and re-radiated by free electrons. Photons are coupled to electrons via Thomson scattering and electrons are coupled to protons via the electromagnetic force; this hot plasma is called a *photon-baryon* fluid. During this epoch, the universe is very hot and dense, and the photon-baryon fluid is at an extremely uniform temperature. The photon-baryon fluid acts as a black body, continually absorbing and re-radiating photons.

The initial conditions of the photon-baryon fluid are of a smooth density field with small random fluctuations. These random fluctuations, which are believed to be the result of an earlier epoch called inflation (discussed in §1.4) have a flat power spectrum. The random fluctuations lay the seeds for the structure of the universe; at much later times, large-scale structures (such as clusters) form in the currently dense regions of the photon-baryon fluid. The force of gravity acts to increase denser regions, pulling in surrounding matter; this effect is opposed by radiation pressure from the coupled photons, and the photon-baryon fluid undergoes acoustic oscillations. Fluctuations in the photon-baryon fluid density cause temperature anisotropies.

As the universe expands, it cools. When the universe cools to a temperature of $\sim$3000 K, it becomes energetically favorable for the protons and electrons to form Hydrogen

atoms. At this point, known as *recombination*, the photons are no longer coupled to electrons and are free to traverse the universe; it is this photon radiation that is referred to as CMB radiation. The temperature of the CMB radiation at this point is the same as the rest of the universe, and T_{CMB} $\sim$3000 K. As the universe expands, so does the wavelength of the CMB photons, and their temperature decreases as the universe evolves. At present time, the temperature of CMB radiation is $T_{CMB} \simeq 2.725$ K.

1.1.1 The (Near) Perfect Black Body and Temperature Anisotropies

In 1994, the Far-InfraRed Absolute Spectrophotometer (FIRAS, [2]) instrument on the COsmic Background Explorer (COBE) satellite demonstrated that the spectrum of CMB radiation produces a near-perfect fit to the theoretical curve of a black body emitter at a temperature of 2.725 K (shown in Figure 1.1). In addition, the Differential Microwave Radiometer (DMR, [3]) instrument on COBE demonstrated that although the observed CMB radiation is remarkably uniform (consistent to within one part in 100,000 in every direction), the CMB contains spatial temperature anisotropies. Many experiments have subsequently resolved these anisotropies at a much finer angular resolution ([4], [5], [6], [7]); at the time of writing, the Wilkinson Microwave Anisotropy Probe (WMAP, [8]) provides the most precise measurements to date. A celestial map which shows the spatial anisotropies of the CMB is shown in Figure 1.2.

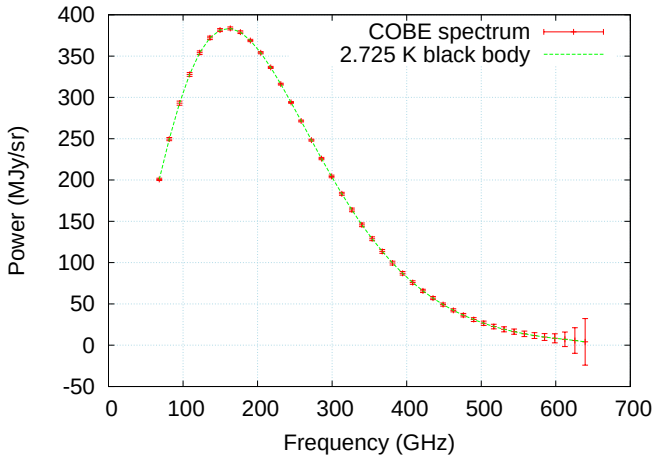

Figure 1.1: CMB spectrum observed by the FIRAS instrument on the COBE satellite [2]. The CMB spectrum, consistent with a 2.725 K black body, peaks at a frequency of 160 GHz. The vertical axis gives the spectrum of the CMB in MJy per steradian. The vertical error-bars measured by FIRAS on the CMB spectrum are so small that they are given at the 100 σ level in this figure.

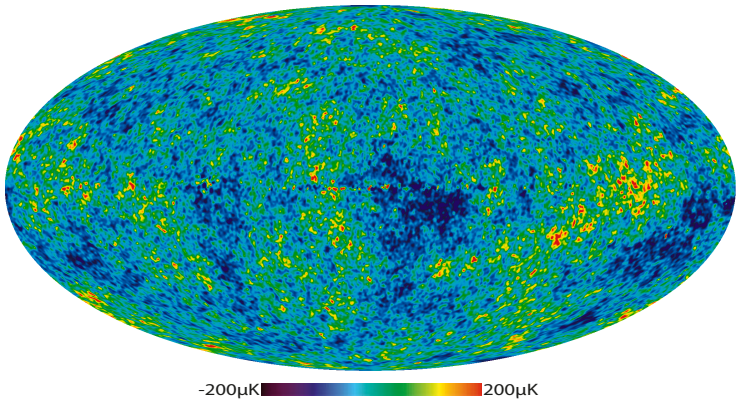

Figure 1.2: The 7-year WMAP celestial temperature map, showing the structure of the temperature anisotropies. The signal from the the Milky Way Galaxy is subtracted using multi-frequency data from WMAP. Image courtesy of the WMAP science team [8].

1.1.2 The Temperature Angular Power Spectrum of the CMB

The spectrum of the observed temperature anisotropies is analyzed in terms of spherical harmonics $Y_{\ell m}(\theta, \phi)$, using the equation

$$\frac{\Delta T\left(\theta, \phi\right)}{T} = \sum_{\ell m} a_{\ell m} Y_{lm}\left(\theta, \phi\right), \tag{1.1}$$

where a_{lm} are the multipole moments of each spherical harmonic. For each value of ℓ, there are $(2\ell + 1)$ independent harmonics m, with $-\ell < m < \ell$. The temperature angular power spectrum from the 7-year WMAP result, consisting of the ℓ power moments (summing over rotationally invariant combinations of m),

$$C_\ell^{TT} \;=\; \left\langle \sum_m a_{\ell m}^2 \right\rangle \;=\; \left\langle a_\ell^2 \right\rangle, \tag{1.2}$$

is shown in Figure 1.3, and clearly demonstrates that the temperature anisotropies seen in Figure 1.2 occur at characteristic angular scales[1]. The structure of the angular power spectrum is principally caused by two competing effects: *acoustic oscillations* and *diffusion damping*. The former effect is due to the heavy nature of baryon particles, which collapse into dense regions under the force of gravity; the latter effect is due to the passage of free photons from denser regions to less-dense regions, which tends to equalize temperatures across a characteristic diffusion scale and diminish the magnitude of the anisotropy. The acoustic peaks seen in Figure 1.3 are the result of adiabatic

[1]Because there are a finite number of m modes for each value of ℓ, C_ℓ is an imperfect estimate of the true variance from which the $a_{\ell m}$ values are drawn. This limitation is called cosmic variance, and indicates even a perfect measurement of the CMB across the entire sky has finite power to constrain theory.

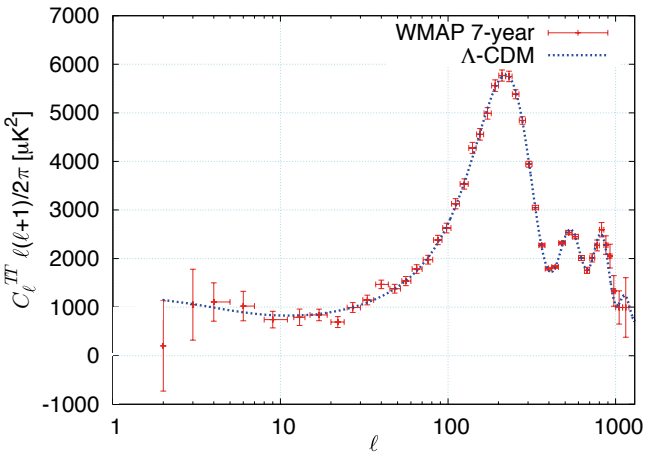

Figure 1.3: The angular power spectrum calculated from the 7-year WMAP celestial temperature map, and the expected temperature angular power spectrum from the Λ-Cold Dark Matter (Λ-CDM model) ([9], §1.2). The x-axis is the multipole ℓ (angular wavenumber), where the angular scale can be approximated by $\theta \sim 180/\ell$. The y-axis gives the power moments, scaled by a factor of $\ell(\ell+1)/2\pi$, so as not to obscure the power with the angular dependent drop in the multipole expansion.

compression of the photon-baryon fluid as it falls into gravitational potential wells.

1.2 Λ-CDM Cosmological Model for an Expanding Universe

If the Big Bang model is correct, the universe expanded from a very compact state and its evolution as a function of time should be able to be modeled. A simple cosmological model for an expanding universe is created using Friedman's equation for an expanding isotropic gas with the help of Hubble's Law. Friedman's equation gives

$$\left(\frac{\dot{a}}{a}\right)^2 = \frac{8\pi G}{3}\rho - \frac{k}{a^2} + \frac{\Lambda}{3}, \tag{1.3}$$

where a is the scale factor of the universe denoting the universal expansion rate, $\dot{a}$ is its derivative with respect to time, G is the gravitational constant, Λ is the *cosmological constant*[2], and k is a constant describing the geometry of the universe (where $k < 0,\ k = 0,\ k > 0$ represent hyperbolic, flat, and spherical geometries)[3]. When we combine this result with Hubble's law, which can be written as $\dot{a} = Ha$, we result with a time-evolution equation for Hubble's constant,

$$H^2 = \frac{8\pi G}{3}\rho - \frac{k}{a^2} - \frac{\Lambda}{3}. \tag{1.4}$$

[2]Einstein added Λ to his modified field equation in general relativity in order to achieve a stationary universe. After seeing data from Hubble's experiment, he would later refer to this as his "greatest blunder".

[3]This constant is unchanging in space or time, and has units of length^{-2}. The formal derivation is provided in Liddle [9].

By differentiating equation (1.3) with respect to time, and using the fluid equation

$$\dot{\rho} + 3\frac{\dot{a}}{a}\left(\rho + \frac{p}{c^2}\right), \tag{1.5}$$

where ρ is the density and p is the pressure, we produce the acceleration equation

$$\frac{\ddot{a}}{a} = -\frac{4\pi G}{3}\left(\rho + \frac{3p}{c^2}\right). \tag{1.6}$$

Equations (1.4) and (1.6) give us the basis for the Λ-CDM model of the expanding universe.

If density parameters Ω, and Ω_Λ are introduced, with

$$\Omega = \frac{8\pi G\rho}{3H^2}, \tag{1.7}$$

and

$$\Omega_\Lambda = \frac{\Lambda}{3H^2}, \tag{1.8}$$

then equation (1.4) can be rearranged to yield

$$\Omega + \Omega_\Lambda - 1 = \frac{k}{a^2H^2}. \tag{1.9}$$

In the event that $\Omega + \Omega_\Lambda$ is unity, $k = 0$ and the universe is geometrically flat.

1.3 Problems with the Big Bang Model

While the Big Bang model successfully predicts a signature microwave black body radiation in the universe, there are three major observations of the universe that it cannot explain:

1. The measured CMB temperature is constant throughout the universe. This is a predicament, as regions of the universe that are not in causal contact have the same temperature. Given that the fastest that information can travel is at the speed of light, this should not be possible. This is termed the *horizon problem*.

2. The universe is measured to be geometrically flat, which requires the critical density of the universe to be very finely tuned (this requires $\Omega + \Omega_\Lambda$ to be unity). The fact that the density takes a special value is known as the *flatness problem*.

3. There is an absence of heavy relic particles (such as the magnetic monopole), while it is predicted by the Grand Unified Theory (GUT) that an abundance of these particles would be created in a very hot and dense early universe.

1.4 The Inflation Paradigm

The theory of inflation is proposed (Guth, 1981 [10]) as an enhancement, rather than a replacement, to the Big Bang model of the universe. It states that when the universe is much less than a second old, a exponential super-luminal expansion of space-time occurred[4].

[4]Recent estimates [11] predict the inflationary epoch to have occurred during the time $10^{-34}\text{s} < t < 10^{-30}\text{s}$ after the universe started to expand.

During this time the acceleration of the scale factor would satisfy

$$\ddot{a}\left(t\right) \gg 0. \tag{1.10}$$

Going back to the acceleration equation (equation (1.6)), this requires the pressure at the point of inflation to be negative ($\rho c^2 + 3p < 0$). If the first two terms on the right-hand side of equation (1.4) are significant, the equation would become quite complex. However inflation rapidly reduces the first two terms to zero (as the universe rapidly expands, $\rho \rightarrow 0$ and a gets very large) and we are simply left with

$$H^2 = \frac{\Lambda}{3}. \tag{1.11}$$

Using $H = \dot{a}/a$, we determine the scaling factor to be

$$a\left(t\right) = \exp\left(\sqrt{\frac{\Lambda}{3}}t\right), \tag{1.12}$$

which provides exponential expansion at the time of inflation.

1.4.1 A Simple (Slow-Roll) Inflationary Model

The simplest inflationary models employ a homogeneous scalar field ϕ in a state of high potential energy V. If the inflationary model is restricted to be a "slow-roll" model ($\dot{\phi} \gg \ddot{\phi}$), then the potential is chosen such that the scalar field slowly returns to its poten-

tial minimum, at which point inflation terminates [12].

Inflationary models predict perturbations in the inflation field and the corresponding metric during the inflationary epoch. These perturbations can be transformed in Fourier space and decomposed into scalar perturbations and tensor perturbations. The amplitude of the ratio of the tensor perturbations to the scalar perturbations is denoted by r, and is called the tensor-to-scalar ratio. With a considerable amount of mathematics[5], the energy scale of the potential V at the time of inflation can be acquired, given by

$$V^{\frac{1}{4}} \sim 10^{16} \left(\frac{r}{0.01}\right)^{\frac{1}{4}} \text{ GeV}. \tag{1.13}$$

This indicates that if the tensor-to-scalar ration r is 0.01, the potential energy V of the early universe was $\sim 10^{16}$ GeV.

1.4.2 Resolving the Problems of the Big Bang Model

Review of the three problems identified in section §1.3 against the postulated rapid inflation model shows:

1. The horizon problem is explained by the observable universe being in causal contact before the inflationary period. When the universe undergoes inflation, spacetime expands at a super-luminous rate, resulting in regions of the universe that were once in causal contact no longer being; this explains how we are able to observe the same CMB temperature in all directions.

[5] See Liddle [12].

2. The flatness problem is explained if the inflationary model uses a perfect exponential expansion (in accordance with equation (1.10)). The expansion of inflation is so great that the curvature of spacetime is diluted and any remaining curvature in the observable universe after the inflationary period is negligible.

3. Heavy relic particles, which would have been created at the densest and hottest energies of the early universe, are now restricted to being created during the *very* short time ($t < 10^{-34}$ s) before the inflationary period began. This dilutes the creation of these exotic particles to such a point that the probability of ever observing one is negligible.

The inflationary model of the universe also explains anisotropies in the temperature spectrum of the CMB, as the density inhomogeneities in the photon-baryon fluid are "blown-up" from a quantum state to a macro state, preserving their quantum fluctuations (perturbations in the scalar field result with denser/less-dense regions in the photon-baryon fluid, which seeds clusters and galaxies).

It has been shown that the CMB, as well as displaying temperature anisotropies, contains a minute polarization signal (roughly two orders of magnitude smaller than the scale of temperature anisotropies). It is postulated that the explosive expansion of space during the inflationary period will have produced primordial gravity waves, ripples in the fabric of space-time; these gravity waves will have left a faint signature imprint in the polarization signal of the CMB. If this faint signature imprint is measured, we will be able to determine details of the inflationary period, when the universe was much less than a

second old.

1.5 CMB Polarization

The cosmic microwave background contains a faint polarization signal; the signal is difficult to measure due to its magnitude relative to the temperature of the CMB and atmosphere and the fact that it is obscured by foreground radiation sources (§1.5.4). We decompose this polarization into two types: E- and B- mode polarizations. E- and B- mode polarizations are named due to their analogous nature to electric and magnetic fields: E-modes are divergence-free polarization fields and B-modes are are curl-free polarization fields. A diagram depicting E- and B- mode polarizations is given in Figure 1.4. E-mode polarization is invariant upon reflection about the axis of the propagating wave vector $\vec{k}$; B-mode polarization flips sign upon a reflection about the axis of the propagating wave vector $\vec{k}$.

1.5.1 Sources of CMB Polarization

CMB polarization is generated by Thomson scattering between photons and electrons. A diagram, demonstrating the mechanism by which a photon is Thomson scattered by a free electron, is shown in Figure 1.5. When an unpolarized photon γ_1, traveling in the $\hat{x}$ direction, encounters a free electron, the electro-magnetic wave of the photon induces a

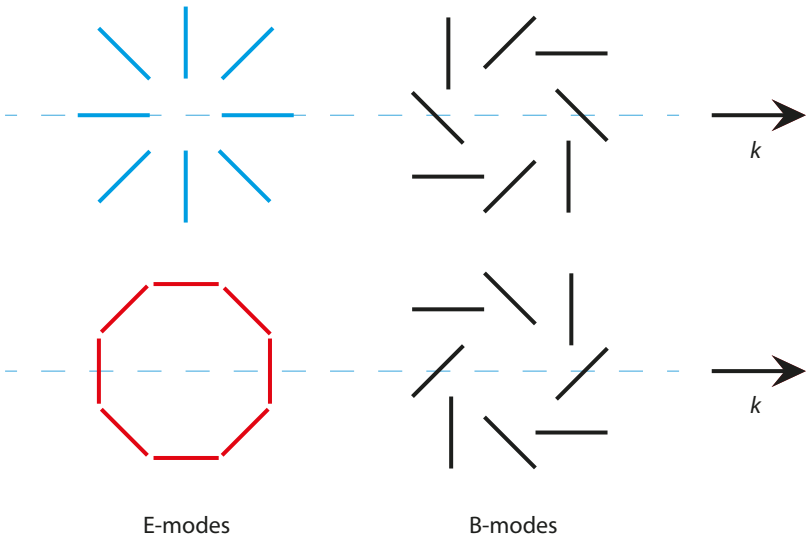

Figure 1.4: E- (left) and B- (right) mode polarizations. E-mode polarization is curl-free and invariant under reflection of the wave vector $\hat{k}$; the blue (red) polarization pattern represents E-mode polarization about a hot (cold) spot. B-mode polarization is divergence free and is reflected 180° by the wave vector $\hat{k}$; the top (bottom) shows left- (right-) handed helicity states.

Lorentz force on the electron. Given the periodic nature of the wave, the photon "shakes" the electron in the y-z plane and the electron reradiates the photon. Since the photon re-radiated by the free electron cannot be polarized along its direction of motion, only one linear polarization state gets scattered. In this example, the electron scatters linear polarization in the $\hat{y}$ direction.

By symmetry though, there is no preferential incoming direction for the photon γ_1, and the scattered linear polarization should be cancelled by a scattered linear polarization created from an incoming photon from the z-direction, γ_2. Therefore, a net polarization

should only be observed if the two photons incident on the free electron have different temperatures, causing a *quadrupole anisotropy*.

The fact that the generation of CMB polarization requires both Thomson scattering and quadrupole moment anisotropies restricts the generation of polarization to the era of recombination[6]. Before the era of recombination, the universe is optically opaque as Thomson scattering events are so frequent that photons are unable to travel significant distances; after the era of recombination there is no longer free electrons to Thomson scatter the photons.

Temperature perturbations in the photon-baryon fluid come from two geometrically distinct sources: scalar (compressional), and tensor (gravitational wave) perturbations. These perturbations respectively correspond to the $m = 0, \pm 2$ quadrupole ($\ell = 2$) spherical harmonics.

E-mode polarization is produced primarily by density (scalar) perturbations in the photon-baryon fluid: velocity gradients in the photon-baryon fluid generated the necessary quadrupole temperature anisotropies in the CMB in the rest frame of the electrons. At large angular scales ($\gtrsim 10^\circ$), velocity gradients in the photon-baryon fluid are driven by the thermody-

[6]CMB polarization is also formed during the era of *reionization*. Reionization occurs in the early universe when objects (such as stars) that are energetic enough to ionize neutral hydrogen gas are formed, approximately $\sim$0.1-1 billion years after the beginning of the universe. At this point though, the universe is much larger than it was during the era of recombination, and the generation of polarization during the reionization era is subdominant to that of the era of recombination (with the exception to very large angular scales, where $\ell \lesssim 10$ [13]).

namic temperature at the surface of last scattering, and the redshifting of photons (Sachs-Wolfe effect [14]) as they climb out of gravitational potential wells. The "effective" differential temperature across the sky (see Hu and White [15]) is expressed as

$$\left(\frac{\Delta T}{T}\right)_{eff} = \frac{\Delta T}{T} + \Psi, \tag{1.14}$$

where $\frac{\Delta T}{T}$ is the temperature differential on the surface of last scattering, and Ψ is the gravitational potential. Gradients in the effective temperature always create temperature flows from hot to cold effective temperature regions. At smaller angular scales, velocity gradients in the photon-baryon fluid are driven by gravitational potentials (collapse) and radiation pressure (expansion) and the photons undergo acoustic oscillations. These acoustic oscillations cause a periodic oscillation in the effective temperature. Figure 1.6 (a) shows the generation of E-mode polarization from a scalar field.

B-mode polarization arises from two sources: tensor perturbations and gravitational lensing. Tensor perturbations, shown in Figure 1.6 (b), occur due to the passing of a primordial gravity wave generated during inflation. As the gravity wave propagates, it stretches and compresses space, distorting the yellow ring of test particles. A photon traveling through a compressed (stretched) region of space will be blue (red) shifted, causing the photon to appear hotter (colder). These tensor perturbations should generate both E- and B- mode polarizations in roughly equal magnitudes, though the amount of polarization generated from the tensor perturbations is much less than that of scalar perturbations. B-modes are also predicted to be generated as a result of gravitational lensing: as E-mode polarization

is propagated from the surface of last scattering, it is lensed by massive gravitational potentials (such as super-clusters and clusters), distorting the E-mode signal into a B-mode signal.

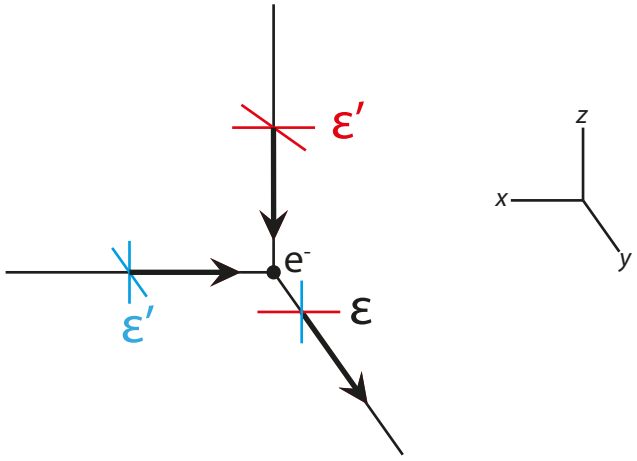

Figure 1.5: Temperature anisotropies generated via Thomson Scattering. A "hot" photon of temperature T_1 (blue), propagating in the $+\hat{x}$ direction, produces linear polarization in the $+\hat{y}$ direction when it is Thomson-scattered off of a free electron. A "cold" photon of T_2 (red), propagating in the $-\hat{z}$ direction, also produces linear polarization in the $+\hat{y}$ direction. When light is isotropic and uniform, these two linear polarization states are cancelled by one another. Quadrupole anisotropies are created during the era of recombination.

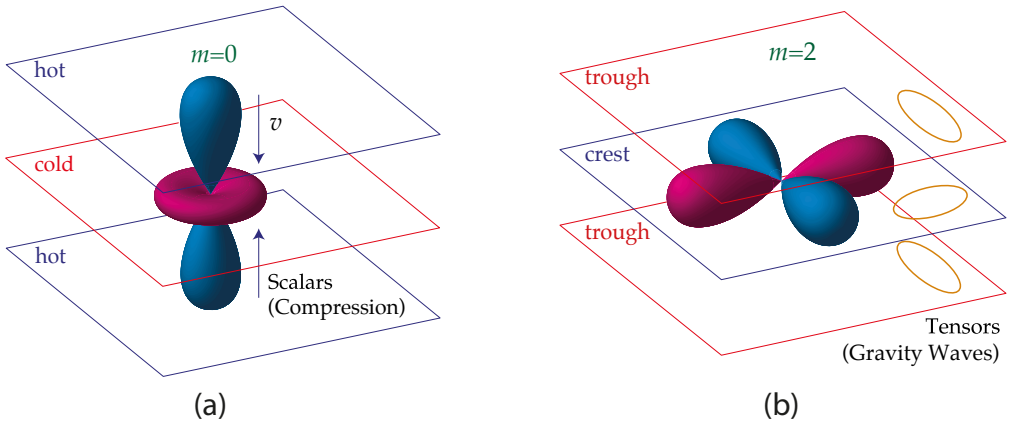

Figure 1.6: Figures (a) and (b) are taken from Hu and White [15], and are published with permission from the authors. (a) shows the scalar quadrupole moment $(\ell = 2, m = 0)$, which produces E-mode polarization during the era of recombination. Flows from hot (blue) to cold (red) regions, $\mathbf{v} \parallel \mathbf{k}$, produce the Y_2^0 pattern depicted here. (b) shows the tensor quadrupole moment $(\ell = 2, m = \pm 2)$, which produces B-mode (and E-mode) polarization; as a gravity wave disports space in the plane of the perturbation, a circle of test particles is turned into an ellipse, and the radiation acquires an $m = 2$ quadrupole moment.

1.5.2 Describing Polarization with Stokes Parameters

Stokes parameters, used to describe the polarization of electromagnetic waves, are denoted by four variables: **I**, the intensity of the field (equivalent to the temperature); **Q** and **U**, the linear polarization of the field; and **V** the circular polarization of the field. The real part of the mode k of a plane electromagnetic wave propagating in the $\hat{z}$ direction can be described using the equation

$$\mathbf{E}_k = \mathrm{E}_x \cos\left(kz - wt + \phi_x\right) \hat{x} + \mathrm{E}_y \sin\left(kz - wt + \phi_y\right) \hat{y}. \tag{1.15}$$

The tip of the vector $\mathbf{E}_k$ will trace out an ellipse in the x-y plane as a function of time. If we let the angle between the major axis of the ellipse (x') and the x-axis be the angle χ, we can describe the coordinate transformation as

$$\begin{pmatrix} x' \\ z' \end{pmatrix} = \begin{pmatrix} \cos\chi & \sin\chi \\ -\sin\chi & \cos\chi \end{pmatrix} \begin{pmatrix} x \\ z \end{pmatrix}. \tag{1.16}$$

Without loss of generality, we can pick a time such that $\mathbf{E}_k(t = 0)$ is purely in the x' direction. This yields

$$\mathbf{E}_k = \mathrm{E}_1 \cos(wt)\,\hat{x'} + \mathrm{E}_2 \sin(wt)\,\hat{y'}, \tag{1.17}$$

where

$$\mathrm{E}_1^2 + \mathrm{E}_2^2 = \mathrm{E}_x^2 + \mathrm{E}_y^2 = E_0^2. \tag{1.18}$$

We can now define an ellipticity angle β that determines the shape of the ellipse for $-\pi/2 < \beta < \pi/2$, where

$$\mathrm{E}_1 = \mathrm{E}_0 \cos\beta, \text{ and } \mathrm{E}_y = \mathrm{E}_0 \sin\beta. \tag{1.19}$$

When the ellipticity angle is $\beta = \pm\pi/4$, the vector $\mathbf{E}_k$ traces out a circle, and the wave is circularly polarized. When the ellipticity angle is $\beta = 0,\ \pm\pi/2$, the vector reduces to a line, and the wave in linearly polarized. Using the transformations deduced from the

above equations,

$$\begin{aligned}
\mathrm{E}_x \cos\phi_x &= \mathrm{E}_1 \cos\chi \quad &&= \mathrm{E}_0 \cos\beta \cos\chi, \\
\mathrm{E}_x \sin\phi_x &= -\mathrm{E}_2 \sin\chi &&= -\mathrm{E}_0 \sin\beta \sin\chi, \\
\mathrm{E}_y \cos\phi_y &= \mathrm{E}_1 \sin\chi \quad &&= \mathrm{E}_0 \cos\beta \sin\chi, \\
\mathrm{E}_y \sin\phi_y &= \mathrm{E}_2 \cos\chi \quad &&= \mathrm{E}_0 \sin\beta \cos\chi,
\end{aligned}$$

we write Stokes parameters as

$$\begin{aligned}
\mathbf{I} &\equiv \mathrm{E}_x^2 + \mathrm{E}_y^2 = \mathrm{E}_0^2, \\
\mathbf{Q} &\equiv \mathrm{E}_x^2 - \mathrm{E}_y^2 = \mathrm{E}_0^2 \cos 2\beta \cos 2\chi, \\
\mathbf{U} &\equiv 2\mathrm{E}_x\mathrm{E}_y \cos(\phi_y - \phi_x) = \mathrm{E}_0^2 \cos 2\beta \sin 2\chi, \\
\mathbf{V} &\equiv 2\mathrm{E}_x\mathrm{E}_y \sin(\phi_y - \phi_x) = \mathrm{E}_0^2 \sin 2\beta.
\end{aligned} \tag{1.20}$$

The parameters $\mathbf{Q}$ and $\mathbf{U}$ measure the orientation of the ellipse relative to the x-axis, and the polarization vector $\mathbf{P}$ is defined to be

$$\mathbf{P} = \sqrt{\left(|\mathbf{Q}|^2 + |\mathbf{U}|^2\right)}\hat{x}', \tag{1.21}$$

with polarization angle

$$\chi = \frac{1}{2}\tan\left|\frac{\mathbf{U}}{\mathbf{Q}}\right|. \tag{1.22}$$

Stokes $\mathbf{I}$, and $\mathbf{Q}/\mathbf{U}$ parameters are respectively used to describe the temperature and polarization spectra of the CMB, and will be seen routinely in this thesis. Given that we

only expect linearly polarized light in the early universe [12], Stokes $\mathbf{V} = 0$ as Thomson scattering cannot generate circular polarization from linear polarization.

While Stokes $\mathbf{I}$ (temperature) is invariant upon a rotation in the angle χ, Stokes parameters $\mathbf{Q}/\mathbf{U}$ (polarization) transform under rotation by an angle χ as

$$(\mathbf{Q} \pm i\mathbf{U}) = e^{\mp 2i\chi} (\mathbf{Q} \pm i\mathbf{U}) . \tag{1.23}$$

This can be expanded in terms of spin-2 spherical harmonics to obtain

$$(\mathbf{Q} \pm i\mathbf{U}) = \sum_{lm} a_{\pm 2 l,m} \, {}_{\pm 2}Y_{lm}. \tag{1.24}$$

1.5.3 Angular Power Spectra for E- and B- Mode Polarizations

In order to map the E- and B- mode polarization angular power spectra (denoted as EE and BB respectively), a process analogous to that used to obtain the temperature angular power spectrum is employed. Given the differences in E- and B- mode polarization behavior seen in §1.5, the spin-2 spherical harmonics ${}_{\pm 2}Y_{\ell m}$ are used to map the E- and B- mode polarization angular power spectra on the celestial sphere. For a multipole ℓ, E- and B- mode polarization angular moments are calculated using

$$a_{E_{\ell,m}} = - \left(a_{2_{\ell,m}} + a_{-2_{\ell m}} \right) /2, \tag{1.25}$$

and

$$a_{B_{\ell,m}} = i\left(a_{2_{\ell,m}} + a_{-2_{\ell,m}}\right)/2. \tag{1.26}$$

Calculating the polarization power moments (summing over rotationally invariant combinations of m) using

$$C_\ell^{EE} = \left\langle \sum_m a_{E_{\ell,m}}^2 \right\rangle = \left\langle a_{E_\ell}^2 \right\rangle, \tag{1.27}$$

and

$$C_\ell^{BB} = \left\langle \sum_m a_{B_{\ell,m}}^2 \right\rangle = \left\langle a_{B_\ell}^2 \right\rangle, \tag{1.28}$$

yields E- and B- mode polarization angular power spectra.

1.5.4 CMB Contamination from Foregrounds

The polarized signal from the CMB is primarily obscured by three foreground sources: the free-free foreground, radiation which results from the scattering of free electrons off of free ions in our galaxy; the synchrotron foreground, radiation which results from the acceleration of high-energy electrons traveling in the Galactic magnetic field; the Galactic dust foreground, radiation which results from interstellar dust located in the galaxy. Each foreground source has its own spectral index, which can be seen in Figure 1.7 (the spectral indices shown in this figure are for the CMB temperature foregrounds). Galactic foreground signals are distinguishable from CMB anisotropy due to their differing spectra; CMB observations are performed at various microwave frequencies, such that the CMB anisotropy signal can be differentiated from the Galactic foreground signals.

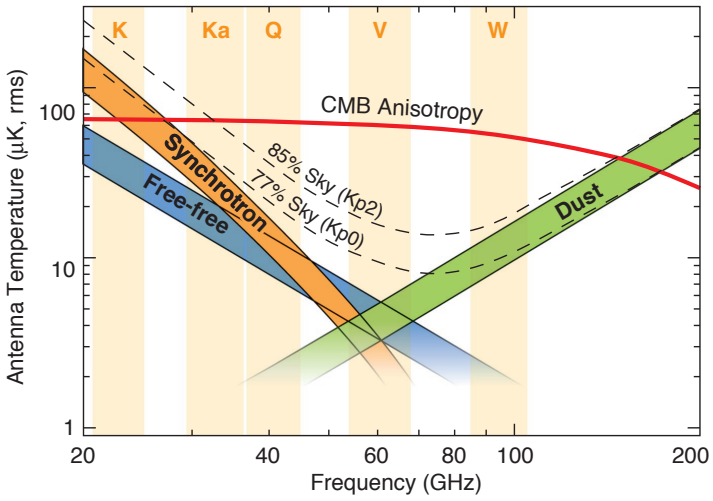

Figure 1.7: The spectral indices of the primary CMB temperature foreground emission contamination spectra are summarized. In the ∼30-150 GHz range, the antenna temperature is dominated by CMB anisotropies. Image courtesy of the WMAP science team [16].

1.6 The Current State of CMB Polarization Measurements

The E-mode polarization spectrum is approximately two orders of magnitude less than the temperature spectrum, and it was not until 2002 that the first detection was made with the Degree Angular Scale Interferometer (DASI, [17]) experiment. Since this initial detection, there has been great interest in confirming and refining these measurements, as well as searching for the elusive, and yet to be detected, B-mode spectrum. If detected, the B-mode polarization spectrum will confirm the validity of the inflationary model.

Figure 1.8 shows the E- and B- mode polarization spectra, as determined from recent CMB polarization experiments (as of the summer of 2010, from the BICEP [18], QUAD

[19], and WMAP [8] experiments), along with the fit from the Λ-CDM model. The E-mode spectra are in excellent agreement with the Λ-CDM model; as of yet, no instrument has detected the B-mode spectrum.

1.6.1 Measuring CMB Polarization with QUIET

The Q/U Imaging ExperimenT (QUIET) is a ground-based telescope designed to measure CMB polarization. The telescope consists of two receivers, with one in the Q- (43 GHz) and the other in the W- (95 GHz) radio frequency band. The primary science goals of QUIET are to measure the first three peaks of the E-mode power spectrum to unprecedented accuracy, to detect or place competitive upper limits on the B-mode power spectrum, and to constrain polarized foregrounds in the CMB fields QUIET observes.

The QUIET data analysis effort uses two independent pipelines, one consisting of a maximum likelihood (ML) framework and the other consisting of a Pseudo-C_ℓ (PCL) framework. The ML framework has long been used in CMB experiments (BOOMERanG [20], WMAP [21], CAPMAP [22]); the framework is computationally expensive, but provides optimal and unbiased maps. The PCL framework has more recently been used by CMB experiments (QUaD [23], BICEP [18], WMAP [24]) and is computationally efficient compared to the ML pipeline; the computational efficiency of the PCL pipeline allows many iterations of the data analysis and is used to determine systematic errors. My work has been on the ML pipeline and any analysis in this thesis (unless specifically mentioned otherwise), will pertain to the ML pipeline. The design and calibration of the

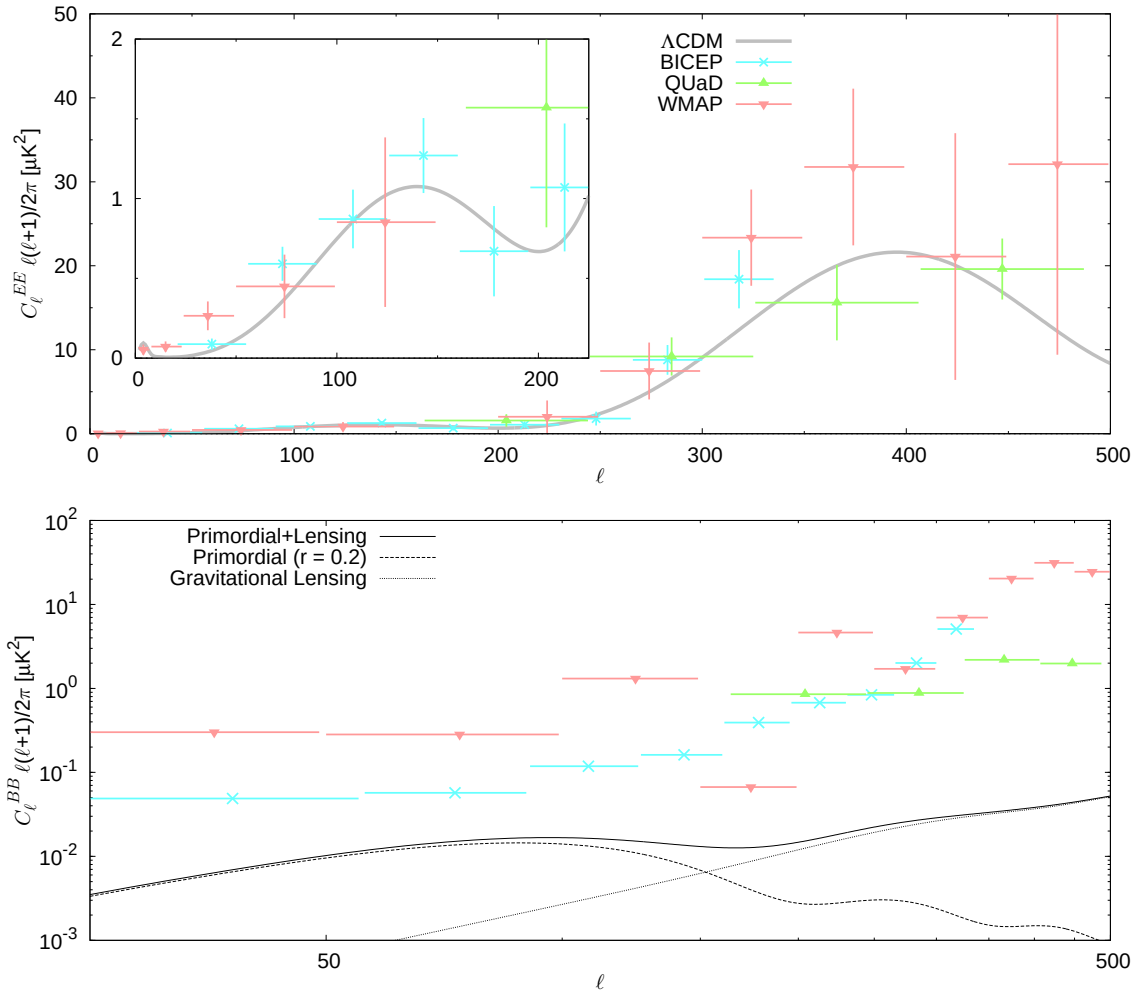

Figure 1.8: The E-mode power spectrum and upper limits on the B-mode power spectrum (95 % confidence limits), as measured from the BICEP, QUAD, and WMAP experiments, for multipole moments of $\ell < 500$. The top panel shows the E-mode power spectrum along with the fit from the E-mode Λ-CDM model. The bottom panel shows the upper limits on the B-mode power spectrum along with the fit from the primordial (long-dashed), lensing (short-dashed) B-mode, and summed B-mode Λ-CDM model.

QUIET experiment, the analysis and results from the Q-band observing season, and the current status of the W-band analysis are the subject of this thesis.

This thesis is organized as follows: chapter §2 details the QUIET instrument, and includes an overview of the site, optics, detectors, electronics and data acquisition software; chapter §3 provides a summary of observations, the CMB fields and calibration sources that QUIET observes; chapter §4 details how we characterize and calibrate the Q- and W- band instruments for analysis; chapter §5 describes data reduction and the analysis procedure, and quantifies systematic errors; and chapter §6 presents the results from the Q-band observing season.

Chapter 2

The QUIET Instrument

The QUIET instrument consists of two arrays of coherent detectors, operating in the Q and W frequency bands. Each array is located in a cooled receiver, with the signal from the CMB on the sky being directed into the array via Mizuguchi–Dragone optics. The receiver and optics are enclosed in a co-moving absorbing ground-screen, which is placed on a three-axis mount. A temperature-controlled enclosure, also placed on the mount, houses the electronics that are required to bias the array and record data.

This chapter, describing the complete physical instrument, is divided into five parts: §2.1 describes the QUIET mount; §2.2 details the optical path of CMB polarization to the QUIET polarimeters; §2.3 provides a detailed description of the QUIET polarimeters and how they rectify Stokes $\mathbf{Q}/\mathbf{U}$ signals; §2.4 describes the electronics required to process the signals from the QUIET polarimeters; and §2.5 provides a description of the QUIET data acquisition software. A summary of the salient characteristics of the QUIET instru-

ment is given in §2.6.

Emphasis is placed on particulars of the instrument which I either designed or to which I provided a major contribution; this includes: the QUIET outer thermometry system and the QUIET window (in §2.2), various custom electronics boards, including module attachment boards (MABs), array interface boards (AIBs) and cables (in §2.4), and peripheral control software (in §2.5).

2.1 The QUIET Mount

QUIET observes CMB polarization in specific fields (areas on the celestial sphere, whose centers are defined by particular right ascensions and declinations) by scanning back and forth over these fields in azimuth. Since the main science goal of QUIET is to measure the first three peaks of the E-mode power spectrum ($25 \lesssim \ell \lesssim 1000$), the instrument must be able to resolve polarization modes at angular scales of approximately $0.1^\circ \lesssim \theta \lesssim 10^\circ$. This requires that the QUIET mount be able to scan CMB fields fast enough such that the faint polarization mode signals are detectable above atmospheric or $1/f$ noise; fast scanning moves the measured signal into higher frequencies of the detector signal spectra, where $1/f$ noise is reduced. QUIET uses the three-axis mount from the Cosmic Background Imager (CBI) [25]. The mount has the capability to slew in azimuth, elevation, and about the antenna boresight (hereafter : deck), and is able to stably achieve azimuth speeds and accelerations of 6.3°/s and 4.5°/s^2 (in azimuthal coordinates): this is sufficiently fast to place the signal measured by the QUIET detectors above the instrumental $1/f$ noise.

A schematic of the mount is shown in Figure 2.1. This figure presents two views: one of the whole telescope from the side, and one of the deck platform from above. In the first view, the telescope and receiver (enclosed in an absorbing ground-screen), are shown on the deck platform, which is hinged to the azimuth platform. The elevation axis is driven by a 7.5 cm ball screw, which acts to open and close a hinge, and enables the telescope to be positioned at an angle of $43^\circ < \theta < 85^\circ$ from zenith. The azimuthal motor (located at the center of the conical base) is able to rotate the mount in azimuth through a 440° angle on a 1.7 m circular ball bearing, and the deck motor (located within the deck platform) enables rotation about the center of the platform (of which are assembled the telescope, receiver, electronics enclosure and ground-screen) through a 440° angle. An image of the mount, with the telescope, receiver, electronics enclosure, and part of the ground-screen atop is shown in Figure 2.2.

The azimuth, elevation and deck positions of the mount (both measured and requested) are recorded every 0.01 seconds; other parameters (quantities that monitor the health of the mount), are recorded approximately every minute. These data are recorded independently of the QUIET polarimeter data.

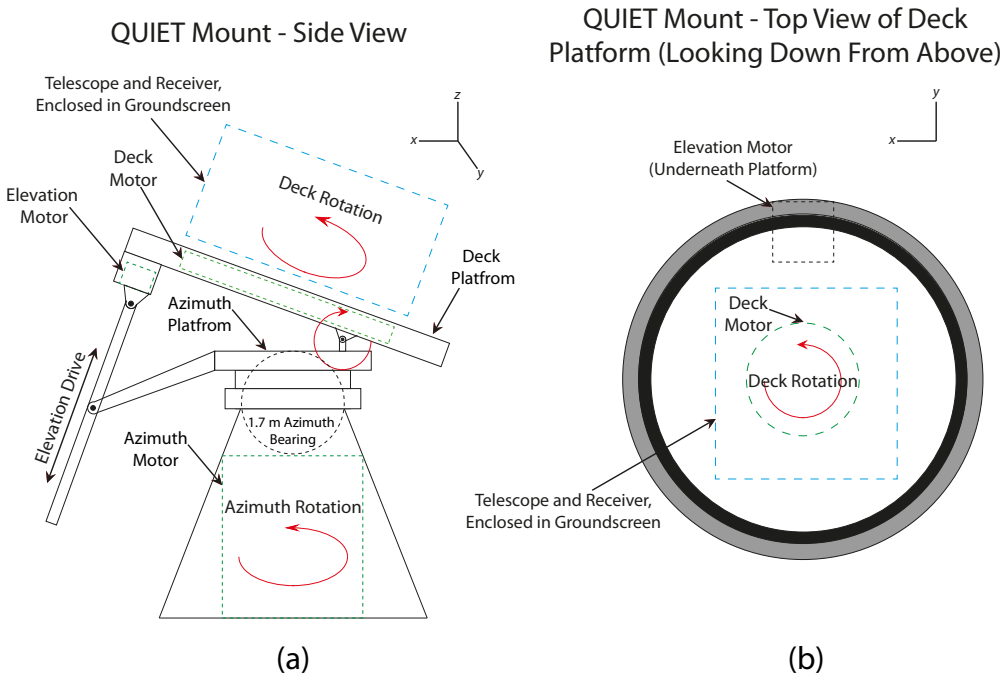

Figure 2.1: The QUIET mount. Motors are denoted by green dashed boxes, the telescope, receiver and ground screen assembly is denoted by a blue dashed box, and axes of rotation are denoted by red arrows. (a) A schematic of the QUIET mount from the ground (side view). (b) A schematic of the QUIET mount from above, looking down on the deck platform. In this view, the white section of the deck platform (which the telescope, receiver and absorbing ground-screen are located on), is able to be rotated about its center while the gray section of the deck platform remains fixed.

Figure 2.2: Photo of the QUIET Instrument. The W-band receiver is shown on the QUIET mount. At this point in the season, the upper ground-screen (§2.2.1.2) is not attached.

2.2 The Optical Path of CMB Polarization to the QUIET detectors

In this section, the optical path from the CMB polarization signal on the sky to the QUIET polarimeters is examined, and a description of the telescope, absorbing ground-screen, cryostat, and outer-thermometry system is provided. Figure 2.3 shows a design drawing of the cryostat and telescope in the frame of the absorbing ground-screen, all of which are sitting on the deck platform of the mount. Light is focused by a crossed-Mizuguchi-Dragone telescope, after which it is sent into the cryogenically cooled cryostat that houses the polarimeter array. The telescope and cryostat are discussed in §2.2.1 and §2.2.2 respectively.

2.2.1 Telescope

A description of the telescope, which includes the Mizuguchi-Dragonian optics, the absorbing ground-screen, and an outer-thermometry system used to monitor the temperature of various parts of the experiment is given below.

2.2.1.1 Mizuguchi-Dragone Optics

QUIET uses a side-fed crossed-Mizuguchi-Dragone telescope, which consists of paraboloidal primary and concave hyperboloidal secondary mirrors (see Figure 2.3). The design is selected because it is able to provide a wide field of view, while simultaneously mini-

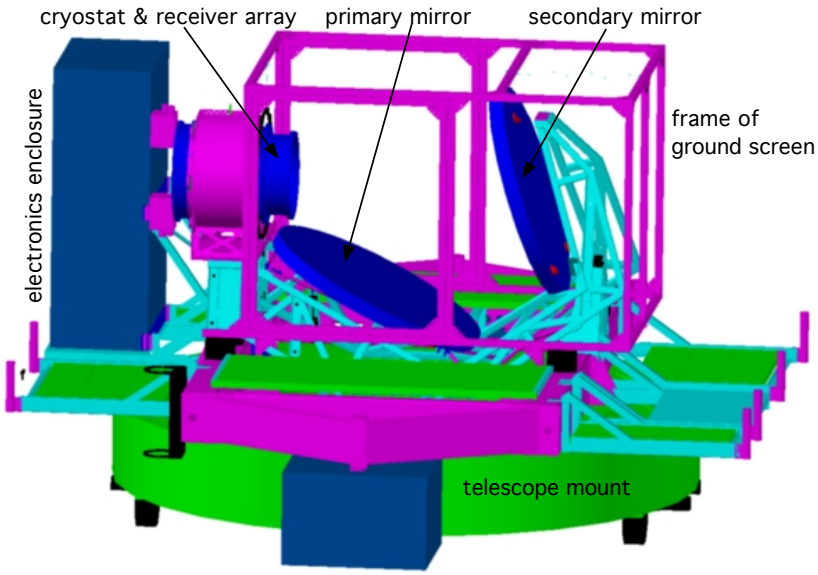

Figure 2.3: Design drawing of the cryostat, telescope, ground screen, and electronics enclosure, all on the deck platform of the QUIET mount. Design drawing courtesy of Keith Thompson.

mizing polarization systematic effects from the mirrors themselves. Mizuguchi-Dragone optics are excellent at maximizing *co-polarization* transmission (the fraction of light in a state (E_X,E_Y) that is transmitted in its original state after reflection by the mirrors), and minimizing *cross-polarization* transmission (the fraction of light in a state (E_X,E_Y) that is transmitted in its orthogonal state after reflection by the mirrors); experimental measurements have shown the cross-polarization transmission of a side-fed Dragonian dual-reflector to be $\sim$-57 db [26]. The QUIET beams are detailed in §4.5 and the resulting systematics are discussed in §5.3.

Light enters from above and is reflected off of the primary mirror to the secondary, and then into the cryostat. QUIET is the first CMB experiment to use a classical Dragonian telescope, but other upcoming CMB experiments plan to incorporate this type of optics (ABS, CMBPol). An effective diameter of $\sim$1.4 m is chosen for both mirrors, such that a beam size of 27.3' (12.2')[1] for the Q- (W-) band receiver is achieved, and thus enabling resolution of multipole moments from $\ell\sim$25 up to $\ell\sim$500 (1000). The low-ℓ limit is constrained by the area of the CMB observing fields QUIET observes[2]; the high-ℓ limit is constrained by the beam size and detector noise.

Each mirror is machined from a single piece of 6061 aluminum, and light-weighted in the back. The surface quality of the mirrors is specified to have distortions of less than $\pm$0.2 mm, and a surface RMS of 0.02 mm/cm; both the distortion and surface RMS magnitudes are much smaller than the wavelength of CMB radiation in the Q- and W- band radio frequencies. The fabricated QUIET mirrors meet the above specifications within 10%, which is good enough to achieve the desired performance from the instrument.

2.2.1.2 Absorbing Ground-Screen

Since the QUIET receivers are sensitive to emission from warm sources such as the earth, it is essential to shield the optical path from sources of unwanted radiation. The magnitude of the emission of unwanted radiation that is able to "spill-over" the mirrors and and

[1] This is the current best estimate for the W-band beam size. Analysis for the W-band season, at the time of writing, is incomplete.

[2] Detected polarization modes must be smaller than the observing fields themselves.

leak into the sidelobes of the QUIET beam is dependent on the azimuth and elevation of the mount[3] and the topography at the observing site.

In order to reduce the effect of spurious radiation leaking into the sidelobes of the QUIET beam, the cryostat and telescope are surrounded by a co-moving absorbing ground-screen. Spurious radiation leaking into the sidelobes of the QUIET beam on time or spatial scales that are of the order of the scan are called *scan-synchronous* contamination; this contamination is the most detrimental to the data collected, as it introduces systematic biases. The ground-screen consists of a metal frame that is covered with eccosorb (HR-10 by Emerson & Cuming), and acts to terminate spurious radiation. With the co-moving ground-screen attached, any spurious radiation that enters the telescope (which is not in the direct path of the optics) is terminated on the ground-screen. The spurious radiation re-radiated from the ground-screen adds to the thermal loading incident upon the receiver, but the re-radiated signal is unpolarized and uniform across the array.

The ground-screen consists of three parts: a bottom ground-screen that blocks spurious radiation from entering in between the mount and the telescope and between the two mirrors, and which is made of several separate pieces; a lower ground-screen, which is a right-angled parallelepiped enclosure that is large enough to fit the telescope and which has a circular cutout for the cryostat window; an upper ground-screen, which is an ex-

[3]To a lesser extent, ground emission that leaks into the sidelobes of the QUIET beam also depends on the position of the deck axis of the mount, given that the top section of the ground-screen (upper ground-screen) is not attached during the Q-band observing season and half of the W-band observing season, and the entrance to the ground screen is asymmetric (rectangular). This is shown in Figure 2.2.

tendable circular snout that limits spurious radiation from above by reducing the angle at which radiation can enter the optical path. Of these three parts only the lower ground-screen is shown in either the photo in Figure 2.2 or the design drawing in Figure 2.3.

For the Q-band observing season and for approximately half of the W-band observing season, the upper ground screen is not installed due to mechanical difficulties with the operation of the extendable snout. After the installation of the upper ground screen there is a significant reduction in the observed contamination leaking into the sidelobes of the QUIET beam. While performing the changeover between the Q- and W- band observing seasons, a few small apertures were noticed in the bottom ground-screen[4]. The closing of these small apertures also results with a noticeable, although much smaller, reduction in the observed contamination leaking into the sidelobes of the QUIET beam. Figure 2.4 shows scenarios where spurious radiation is able to enter the cryostat. Figure 2.5 shows the pattern of spurious sidelobe radiation leaking into the QUIET beam as a function of azimuth and elevation before and after the aforementioned improvements to the ground-screen.

2.2.1.3 Outer Thermometry System

An outer thermometry system, consisting of thirty-two thermometers placed on and around the telescope, ground-screen and cryostat, is used to monitor the temperatures of essential

[4]The bottom ground-screen is positioned between the telescope mount and the sled that holds the primary and secondary mirrors (see Figure 2.3), and consists of many separate sections (due to the shape of the sled and mount). Given that the bottom ground-screen is broken up in to many sections, it proves more difficult to ensure continuity, and a few small apertures where spurious radiation is able to leak into the optical path were found.

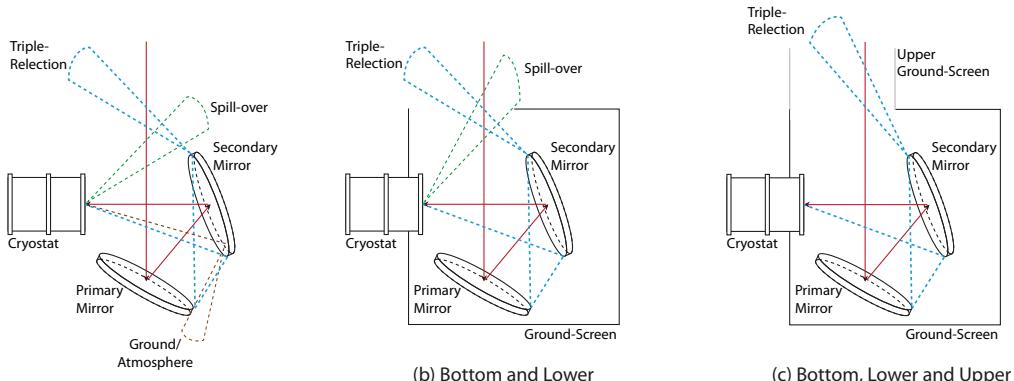

Figure 2.4: Examples of spurious signals entering in to the QUIET beam. In these examples, the optical path of the light to be observed is denoted by the solid red line. The optical path of spurious signals are denoted by the dashed brown, green and blue lines. **(a)** Without a ground-screen, any ground or atmospheric source has the possibility of entering the optical path of the telescope and injecting contamination into the signal. This could be contamination from the ground that is reflected into the cryostat (brown) "spill-over" contamination that passes from behind the mirrors (green), or triple-reflection contamination (blue) that comes in through the top of the upper ground-screen, and bounces off the telescope mirrors three times before entering the cryostat. **(b)** With the bottom and lower ground-screen in position, "spill-over" from the mirrors becomes the main source of contamination, with triple-reflection contamination and contamination from holes in the bottom ground-screen contributing to second order. **(c)** After installation of the upper ground-screen (the snout, shown in light grey), the angle at which triple-reflection and "spill-over" contamination can enter the optical path is reduced, and triple-reflection contamination becomes the dominant source of contamination.

components of the QUIET instrument. Three-terminal AD590 temperature-to-voltage transducers are selected for use in the outer thermometry system for three reasons: 1) AD590s are able to be used in temperatures between -50 Celsius and 150 Celsius, which is more than sufficient for measuring ambient temperatures at the site; 2) AD590s are robust active components that can be powered by a large range of voltages (4–30 V), and

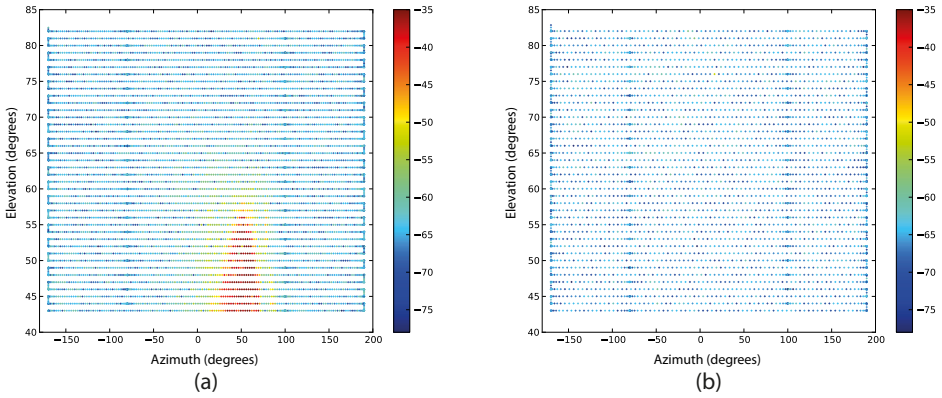

Figure 2.5: Study of spurious sidelobe radiation leaking into the QUIET beam, performed with the W-band receiver midway during the W-band observing season. A carrier-wave is directed towards the QUIET mount (after the sun is below the QUIET observing horizon), and the mount is rotated in azimuth (full rotation), elevation (between $43°<\theta<83°$ in $1°$ increments), and deck (between $0°<\theta<360°$ in $90°$ increments). The plots shown are for polarimeter RQ50 in the W-band array, at a deck of $90°$. The color-scale is logarithmic, though the units of intensity are arbitrarily set. (a) shows the spurious radiation (yellow and red flares) entering the optical path of the telescope before the apertures in the bottom ground-screen are closed and the upper ground-screen is installed. (b) shows the significantly reduced spurious radiation leaking into the sidelobes of the QUIET beam after the apertures in the bottom ground-screen are closed and the upper ground-screen is installed.

are designed to output a consistent and convenient response of 1 μA/Kelvin; 3) The grade of AD590s necessary for the experiment are cost-effective (the grade selected provides a 0.1 K precision).

Due to the difficulty of measuring a faint signal such as CMB polarization, it is undesirable to add an additional power supply inside of the electronics enclosure: the power supply for the AD590s is placed in a aluminum breakout box, bolted to the outside of the electronics enclosure. The AD590s are connected to components of the QUIET instru-

ment via twisted-shielded cables which are interfaced to the electronics breakout box. The locations of the AD590s are as follows: three thermometers are placed on the backs of each telescope mirror; 17 are placed on the bottom and lower ground screen; 3 are placed on the backside of the cryostat and one is placed at the front (near the window) of the cryostat; 2 are insulated from the telescope using G-10 composite material (a glass-reinforced epoxy laminate) and used as air temperature sensors; and the 4 remaining channels are left unused (such that the system can be expanded if desired). The AD590s are attached to their respective surfaces using a stycast resin.

A frequent measurement of the temperature of the outer components of the QUIET instrument allows detection of over-heating components (which gives a measure of the expected additional loading, albeit small, from the ground-screen and cryostat), or if there is a temperature gradient over the mirrors (differential temperatures across the mirrors can lead to polarization systematics across the array). The temperatures from the AD590 sensors are acquired every five minutes using two Sensoray 2608 analog cards, and recorded by the QUIET data acquisition software.

2.2.2 The QUIET Cryostat

A description of the cryostat, including all of the optical components that the incoming signal traverses on its way to the polarimeters (the window, the IR-blocking material, the feedhorns, and the septum polarizers) is given below. In order to achieve optimal performance from the QUIET polarimeters, it is necessary to cryogenically cool them to a

temperature of ∼20 Kelvin[5]. The Q- and W- band polarimeter arrays are each housed in their own cryostat under vacuum. The design of the Q- and W- band cryostats are similar, with only the physical dimensions and number of polarimeters changing between the two[6]. The cryostats are cooled using two Gifford-McMahon dual-stage refrigerators, (CTI-1020 refrigerators, each requiring their own water-cooled compressor), and are made up of three stainless steel sections: a lower section, where the refrigerators and electronic connectors are located; a middle section, where the electronics, polarimeters, septum polarizer ortho-mode transducers (OMTs) and feedhorns are located; and an upper section, which holds the optical window and is filled with an IR blocking material. Figure 2.6 (a) shows a design drawing of the W-band cryostat, and Figure 2.6 (b) shows a photograph of the Q-band cryostat.

The cryostats are designed with removable sections so that servicing any part of the array (in the case of a mechanical failure) is simplified. Each cryostat is outfitted with a pressure gauge and 12 cryogenic thermometers to monitor the vacuum of the cryostat and the temperature of the refrigerators, polarimeters and feedhorns.

2.2.2.1 Optical Window

The design of the cryostat window is driven by the requirement to maximize transmission while being capable of withstanding the vacuum pressure of the cryostat (pressure of ∼15

[5]This is a modest temperature compared to the ∼50-300 mK cryogenic temperature required for CMB polarization experiments that utilize bolometric detectors.

[6]The Q- (W-) band cryostat houses an array of 19 (91) polarimeters. The footprint of the Q-band polarimeter is ∼4 times that of a W-band polarimeter.

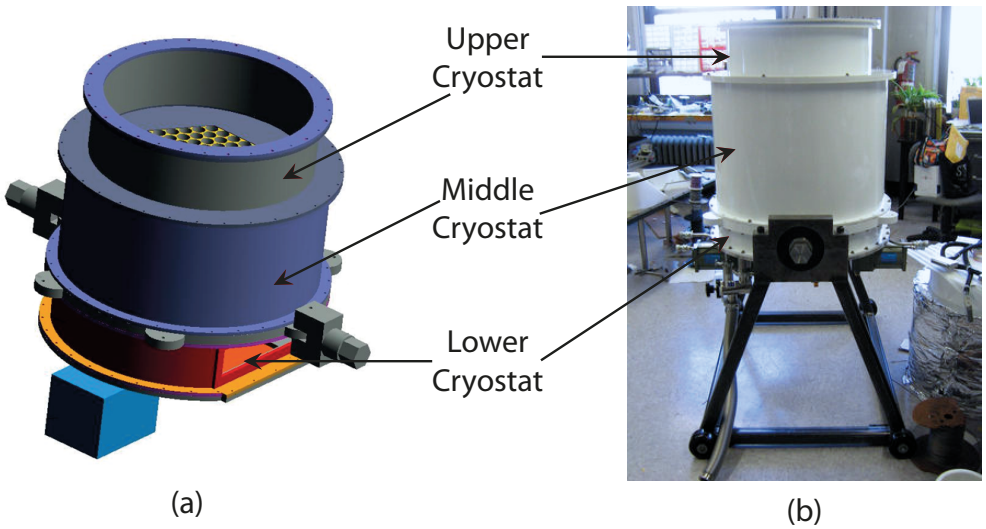

Figure 2.6: (a) Design drawing of the W-band cryostat. (b) Photo of the Q-band cryostat. Design drawing and photo courtesy of Laura Newburgh.

lbs/in^2) for a period of at least 3 years in time. The windows are about 22" in diameter, the largest of their kind to date. Ultra-high-molecular-weight polyethylene (UHMW), known for its durability and for its transparency in the microwave frequency bands, is used as the window material. The UHMW is then coated with an anti-reflective material in order to minimize the amount of stray light that can enter the cryostat.

In order to determine what material to use as an anti-reflective coating, the condition for zero reflection in a single layer film (see Hecht [27]) is used,

$$n_{AR}^2 = n_{air} n_{film}, \tag{2.1}$$

where n_{AR} is the index of refraction of the anti-reflective coating, n_{air} is the index of refraction of air, and n_{film} is the index of refraction of the window material. The index of refraction of UHMW is not available in literature[7], however the variation in the index of refraction of polyethylenes is small ($\simeq 2\%$), and therefore the index of refraction assigned to UHMW is the known value of high-density polyethylene (HDPE), $n_{film} = 1.525$. This requires the index of refraction of the anti-reflective material to be

$$n_{AR} \simeq 1.2. \tag{2.2}$$

The index of refraction of expanded teflon (PTFE) is $n_{PTFE} \simeq 1.22$, and PTFE is selected as the anti-reflective coating material.

2.2.2.2 Fabrication of the Optical Window

The cryostat windows are fabricated in the Columbia laboratory using a novel technique. PTFE, well-known for its "non-stick" surface properties, is fused to the surface of UHMW in a heat-press using low-density polyethylene (LDPE) as an adhesive[8]. Since it is desirable to have no air pockets between the UHMW and the PTFE during the fusion process, the setup is placed in a large vacuum chamber that is able to attain a vacuum of $\sim$1 Torr. A diagram of the apparatus used to fabricate windows in the vacuum chamber is shown in Figure 2.7 (a).

[7] At the time of writing, as far as we know.

[8] The window-making process is developed as part of a NASA filter development project.

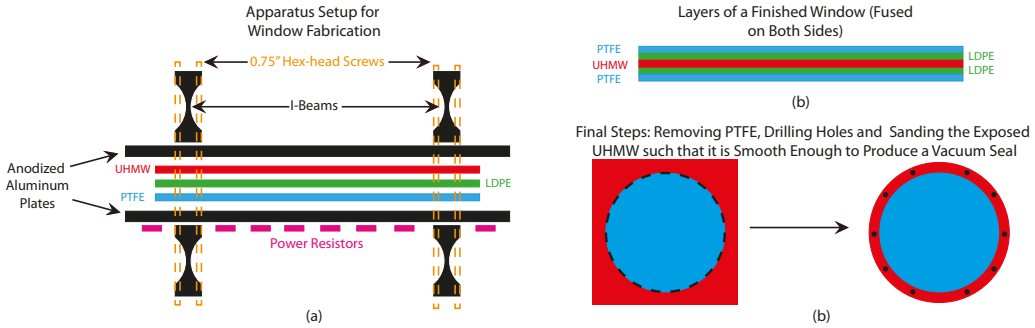

Figure 2.7: (a) Setup used for fabricating optical windows for the QUIET cryostats. (b) Layers of a QUIET window (fused on both sides). (c) Finishing touches that are applied before the window is ready to be put on the cryostat: removal of PTFE and sanding of UHMW from vacuum seal area, drilling holes such that the window can be fastened in the window holder, and removal of excess (square edges) UHMW.

An eight-step process is used to fabricate the QUIET windows:

1. A square piece of UHMW (length and width of 24" by 24") is roughed up using a power-sander for $\sim$1 hour on each side. This increases the surface area of the UHMW, which facilitates the adhering process.

2. A square layer of PTFE and LDPE are placed (in that order) on the bottom surface of the heat-press, followed by the piece of UHMW. The top layer of the heat press is placed on top and two pairs of I-beams (drilled, with tapped holes on the bottom) are fastened tightly using 3/4" diameter hex-head screws.

3. The chamber is evacuated, and the bottom layer of the heat-press is heated to $\sim$100° C by running a current through a set of 25 power resistors, evenly distributed on the bottom surface of the heat-press. Holding the plate at this temperature (which is hot

enough to melt the LDPE, but not hot enough to melt the PTFE or UHMW) for $\sim$3 hours, the first layer of PTFE is fused to one side of the UHWM.

4. The window is cooled down under vacuum, after which vacuum pressure is released, and the window is removed.

5. Steps 3) and 4) are repeated on the other face of the window.

6. The window now consists of a square piece of UHMW with PTFE fused on both sides. PTFE is porous and cannot hold a vacuum, so a ring of PTFE is removed on both sides, such that the material where the window makes surface contact with the window holder is UHMW (Figure 2.7 (b)).

7. The area of UHMW exposed for creating a vacuum seal is sanded down until it is smooth enough to be able to hold vacuum. This takes a considerable amount of time ($\sim$3-6 hours), given that the UHMW surface is originally roughed up to help adhere the PTFE to the UHWM.

8. After the area of UHMW to be exposed to the vacuum seal is smoothed, holes are drilled into the window so that the window could be fastened to the window holder, and the square piece of UHMW is trimmed down to a circular shape (Figure 2.7 (c)).

2.2.2.3 Window Material Specifications

Using the process mentioned in §2.2.2.2, windows for the Q- and W- band cryostats are fabricated. In order to maximize the amount of radiation transmitted through the win-

dow, the thickness of the UHMW is carefully chosen to be half or full integral multiples of the Q- and W- band wavelengths while ensuring that the window is strong enough to withstand the pressure of vacuum, and the thickness of the PTFE is determined from optimizing the transmission in laboratory tests. Table 2.1 gives the thicknesses of the materials selected for the Q- and W- band windows. The process for choosing these parameters is a compromise between strength and performance, and both windows transmit more than 98.6% of radiation in the desired frequency range. Transmission curves for Q-/W- band windows using the parameters given in Table 2.1 are shown in Figure 2.8.

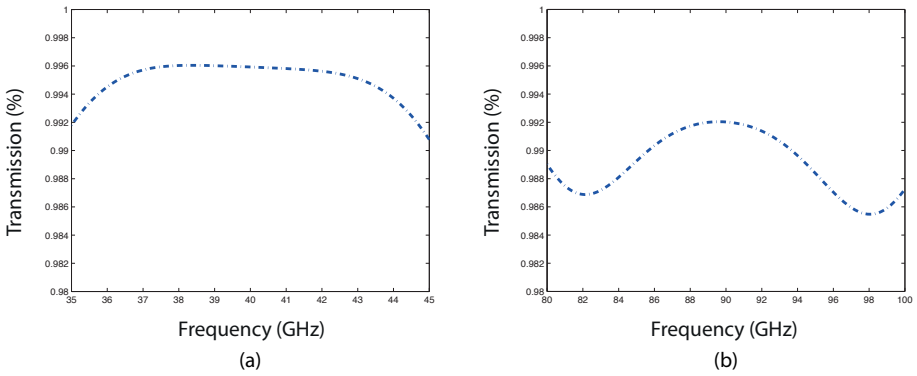

Figure 2.8: Simulated transmission curve for a: (a) Q-band frequency window; (b) W-band frequency window.

Even with a UHMW thickness of 3/8" (1/4") for the Q- (W-) band window, the window "bows" in about 3 inches under the pressure of vacuum. A simulation demonstrating the effect that a 3-inch bowing has on the transmission/reflection curves can be seen in Figure 2.9 (a). Teflon manufacturers often quote thickness tolerances to within $\pm 10\%$; a simulation, showing the effect of a 10% increase in the thickness of the teflon used for the

window can be seen in Figure 2.9 (b). Although these non-idealities (a 3-inch bowing of the window, or a 10% increase in the thickness of the teflon used for the AR coating) incur a visible change in the transmission coefficients seen in Figure 2.8, the variation is small, and the effect that this variation has on the acquired data is negligible.

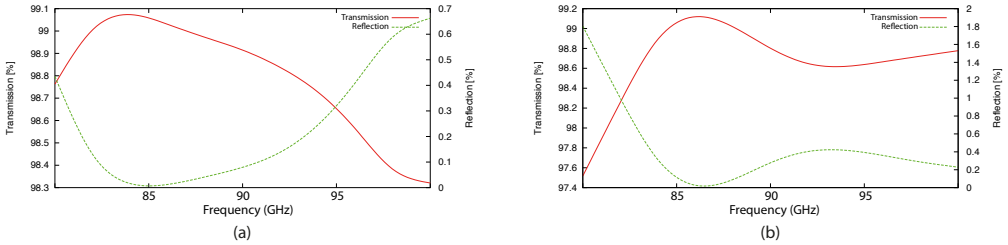

Figure 2.9: (a) Shows the transmission/reflection curves for an AR-coated W-band window when "bowed" in 3 inches. This corresponds to a known non-ideality that occurs when the cryostat is under vacuum. (b) Shows the transmission/reflection curves for an AR-coated W-band window, whose teflon thickness is 10% greater than desired. Both simulations yield transmission coefficients of greater that 98.3% in the W-band frequency range of interest (90-100 GHz).

Band	UHMW thickness (inches)	LDPE thickness (inches)	PTFE thickness (inches)
Q-	0.375	0.005	0.0625
W-	0.25	0.005	0.0213

Table 2.1: Window Properties Summary

2.2.2.4 IR Blocking Material

In the upper section of the cryostat, the volume inside the cryostat between the window and the middle cryostat is occupied by a layer of polystyrene foam, which acts as an IR blocker. The polystyrene foam block is a cylinder with a diameter of the size of the

window ($\sim$22 inches) and a height of 4-inches. The IR blocker reduces any incident IR radiation at 300 K to a temperature of $\sim$80K; the power of the IR radiation scales as σT^4, where T is the temperature of the radiation and σ is the Stefan-Boltzmann constant, thus decreasing the IR power by a factor of $(300)^4/(80)^4$.

2.2.2.5 The Array Engine

After the signal has passed the window/(IR blocker), it is then processed by the array engine, which consist of corrugated feedhorns, OMTs and QUIET polarimeters. For each QUIET polarimeter, a corrugated feedhorn transforms waves propagating through free space to a waveguide, which is bolted to an OMT, which is in turn bolted to an individual QUIET polarization detector. Figure 2.10 shows a schematic of the QUIET Q-band array engine. The corrugated feedhorns couple the incident plane wave to the OMT, which splits the incident plane wave into left and right circularly polarized light. These components are then piped into the QUIET polarimeter via waveguide inputs where they are processed such that Stokes **Q** and **U** polarizations can be measured.

2.2.2.6 Corrugated Feedhorns

In the Q- (W-) band cryostat, an array of 19 (91) feedhorns is placed in between the the window/(IR blocking material) and the OMTs. The feedhorns are used to couple the incident plane wave to the waveguide with as close to optimum impedance matching as possible. Each feedhorn is bolted to an individual OMT in the array, which is in turn bolted to an individual polarimeter in the array. Corrugated feedhorns are used in

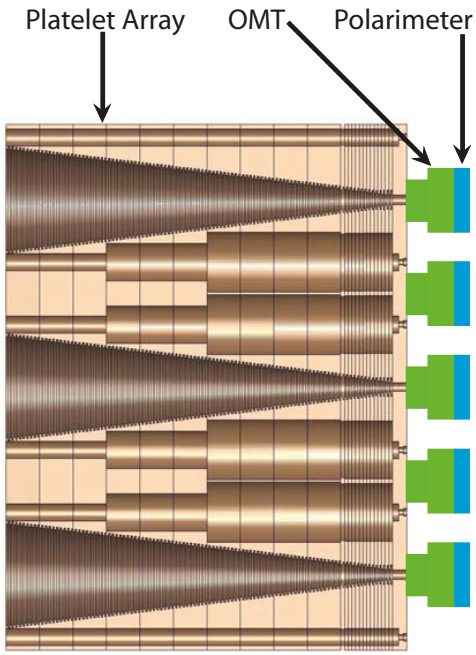

Figure 2.10: A schematic of the array engine for the Q-band receiver. The signal is transformed in free space by the corrugated feedhorn to a waveguide, after which it is split into left and right circularly polarized light by the OMT and piped into the QUIET polarimeter. This schematic presents a cross-section of the array engine, and only 5 polarimeters are visible (the Q-band array consists of 5 rows of polarimeters and the remaining polarimeters are behind those shown). Given the location of the polarimeters in the array, only three feedhorns are visible in this cross-sectional view. The stacked cylindrical regions (in between feedhorns) are machined out (light-weighting the platelet array), and serve to bolt screws embedded in the platelet array to an interface that attaches to the OMTs. Design drawing of platelet array courtesy of Joshua Gundersen.

microwave experiments because of their very low sidelobe radiation patterns, excellent impedance matching, low return loss and cross-polarization (generally $<$ -35 db), and high gain (generally $>$ 26 db).

The standard feedhorn used in CMB experiments to date has been the electroformed corrugated feedhorn. Standard electroformed corrugated feedhorns are individually fabricated (which results in high costs); an example of a corrugated feedhorn from the SunyaevZel'dovich Array (SZA) experiment is shown in Figure 2.11 (a). Given the large numbers of polarimeters in the QUIET arrays, an innovative and much less expensive method is employed to produce an array of corrugated feedhorns: instead of individually machining each corrugated feedhorn, a *platelet array* is formed from layers of metal plates, with each layer having several corrugations machined in it. These plates are then diffusion-bonded together, simultaneously making corrugated feedhorns horns for all of the polarimeters in the array. The Q-band platelet array is shown in Figure 2.11 (b). Laboratory measurements indicate that the diffusion-bonded platelet array of feedhorns performs up to the same standards as standard electroformed corrugated feedhorns.

2.2.2.7 Septum Polarizers

Before the CMB polarization reaches the QUIET polarimeters it passes through a septum polarizer OMT. The septum polarizer in the OMT consists of a thin piece of aluminum, with a "stepped"-profile. A diagram of the inside of an OMT is depicted in Figure 2.12 (a). Waves can be decomposed into two components: one that is polarized perpendicular to the septum (input 1, E_X-plane polarized) and one that is polarized parallel to the septum (input 2, E_Y-plane polarized). Figure 2.12 (b) shows the resulting action of the "stepped"-septum on a perfect E_X-plane and perfect E_Y-plane wave. The E_X-plane wave is split into two components, but the signal is unchanged in direction; the B-plane wave is rotated 90° on the left-hand side (or equivalently, E_Y is multiplied by a factor of i), and -90° on

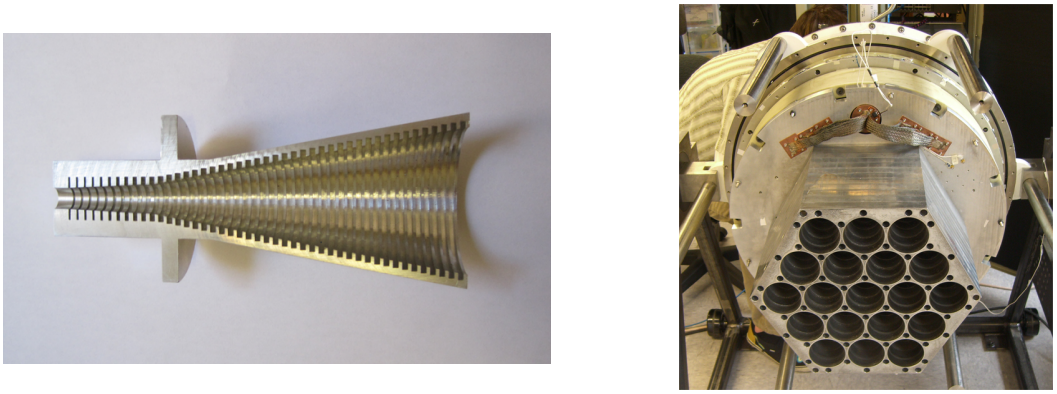

(a) (b)

Figure 2.11: (a) An image of a machined feedhorn (prototype from the SZA experiment). (b) The platelet array (all corrugated feedhorns together) for the Q-band cryostat. Photo of the platelet array courtesy of Laura Newburgh.

the right-hand side (or equivalently, E_Y is multiplied by a factor of $-i$). The resulting signals at the left and right output ports are

$$L = \frac{E_X + iE_Y}{\sqrt{2}}, \tag{2.3}$$

and

$$R = \frac{E_X - iE_Y}{\sqrt{2}}, \tag{2.4}$$

giving left- and right- circularly polarized light. The left- and right- circularly polarized light signals are each piped to a separate input to the polarimeter.

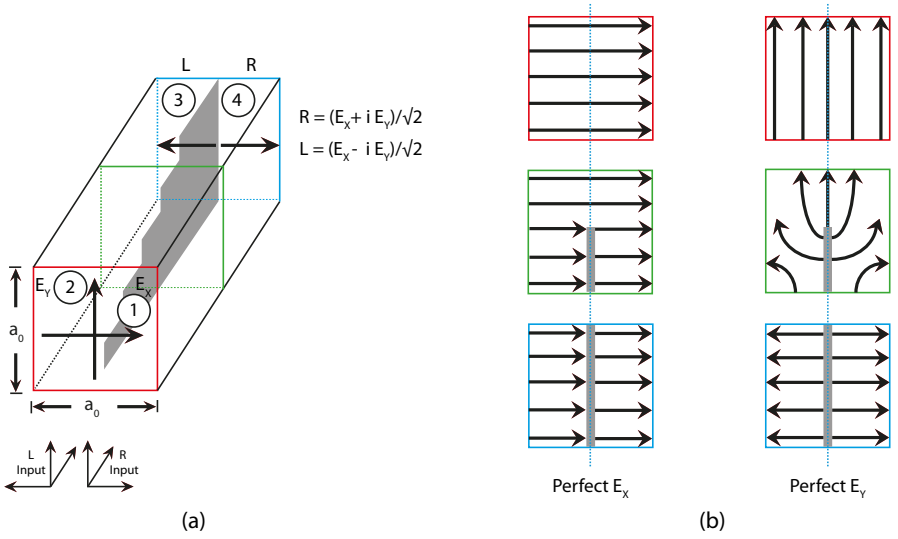

Figure 2.12: Septum polarizer diagram. The original digram (courtesy of Ed Wollack) has been modified and reproduced for this thesis: (a) input ports 1 (E_X) and 2 (E_Y), and output ports 3 (L) and 4 (R); (b) the behavior of a perfect E_X and E_Y components of an incident electromagnetic wave. The color of the box on the OMT in (a) corresponds to the signal shown in the E_X and E_Y boxes of the same color in (b). The diagram for the E_X and E_Y components is shown at three steps : 1) at the top of the OMT, before they have encountered the splitter ; 2) half-way down the OMT, when the septum polarizer has begun to act on the E_X and E_Y components; 3) the respective E_X and E_Y signal components that are output at the bottom of the OMT.

2.3 QUIET Polarimeters

This section provides a description of the QUIET polarimeters. Although the Q- and W-band polarimeters operate a different frequencies, the mechanism by which they operate

and detect CMB polarization is the same, and the provided description of their function is applicable to both.

After the light entering the cryostat is split by the septum polarizer into left ($L = E_X + iE_Y$) and right ($R = E_X - iE_Y$) circularly polarized components, these components are separately piped into the polarimeters via two rectangular waveguide inputs. The polarimeters amplify and process the L and R components, detecting Stokes $\mathbf{Q}/\mathbf{U}$ linear polarizations. The design of the Q- (W-) band polarimeter is such that the signal amplification and processing (by means of amplifiers, phase-switches, hybrid couplers, filters and detector diodes – all of which are connected by a stripline conductor) occurs within a 2" by 2" (1.4" by 1.4") brass casing: we refer to these assemblies as QUIET *modules*. Figures 2.13 and 2.14 respectively show a schematic and photo of a QUIET polarimeter.

Each of the polarimeter components is described in §2.3.1; the theory of their operation is detailed in §2.3.2; and the process by which a pair of QUIET polarimeters can be paired together to create a pair of total power assembly detectors is described in §2.3.3. Factors that are used to correct for instrument/polarimeter imperfections are discussed in §2.3.4.

2.3.1 Polarimeter Components

Figure 2.13 shows how left and right circularly polarized light enters the polarimeter via waveguide inputs A and B, and subsequently traverse amplifiers, phase-switches, hybrid couplers, power splitters, and filters before being detected as Stokes $\mathbf{Q}/\mathbf{U}$ linear polarizations at the QUIET detector diodes. This section details each of these components.

2.3.1.1 Amplifiers

QUIET polarimeters use three stages of monolithic microwave integrated circuit (MMIC) technology low-noise amplifiers (LNAs) to magnify the polarization signal from the CMB. The LNAs are able to amplify GHz radio frequency signals while preserving their phase. Each Q- (W-) band LNA has three (four) stages of high electron mobility transistors (HEMTs, fabricated from Indium Phosphide (InP)), which are set up in a cascading design and which share a common drain current and gate voltage. A schematic of a Q-band LNA is shown in Figure 2.15. The signal is initially input to the source terminal of the first transistor, is amplified, and is output to a capacitor. The output from the first transistor is composed of the alternating-current RF signal and the direct-current bias voltage. The direct-current bias is removed by the capacitor, and the output from the capacitor is input to the second transistor in the cascading chain. This process is repeated at the second and third stage transistors.

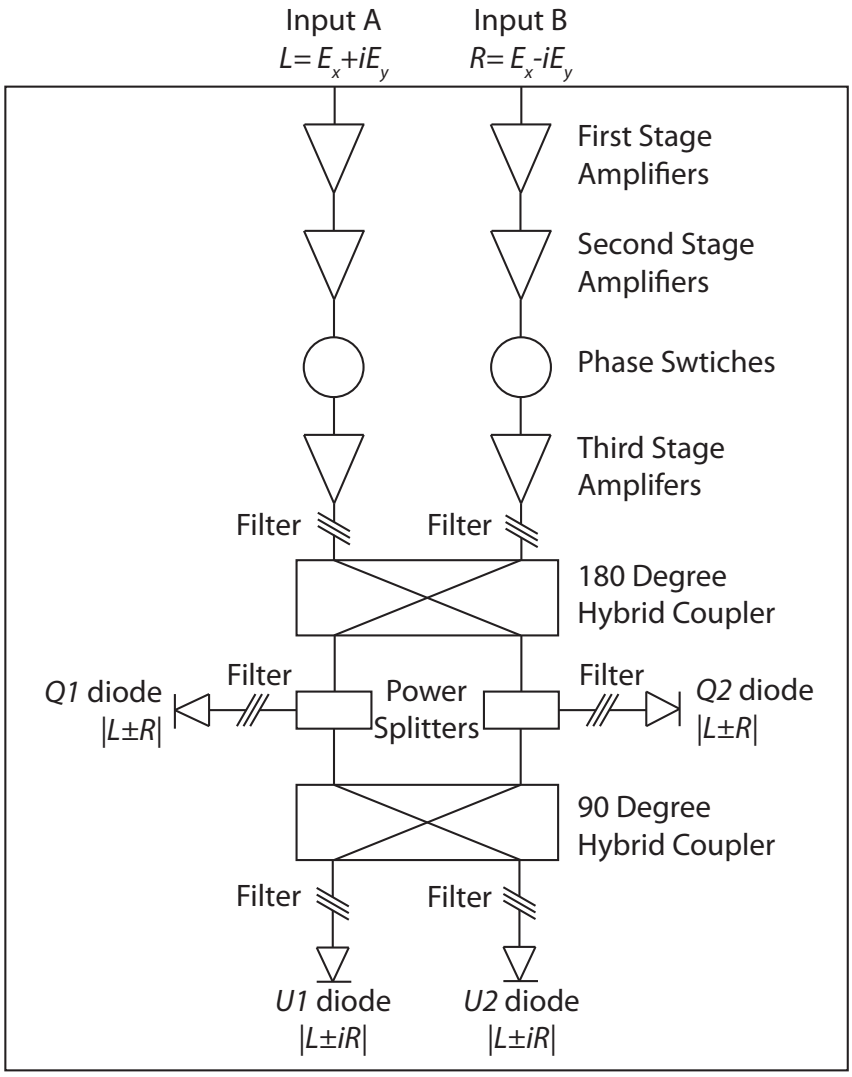

Figure 2.13: A schematic of the components in the QUIET polarimeter. Left and right circularly polarized light enter the polarimeter from two waveguide inputs. The signal is processed and each Stokes Q and U polarization is detected on a pair of detector diodes.

The first two stages of LNAs occurs directly after the signal enters the input of the module.

The signal is then phase-switched, and amplified a third time. Phase-switches are lossy

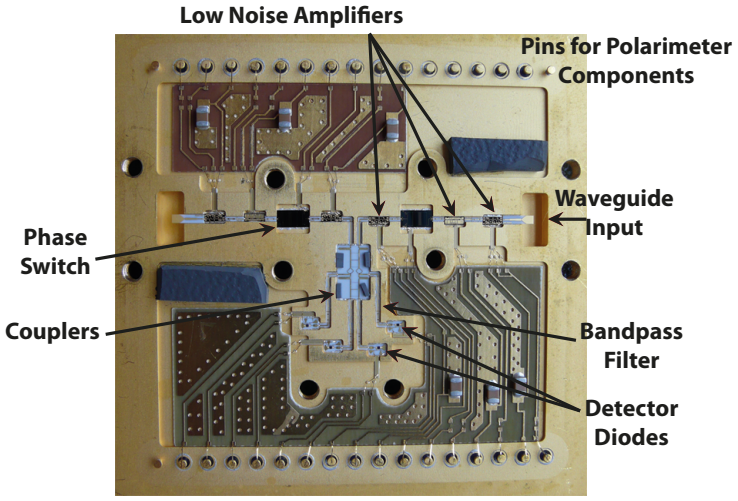

Figure 2.14: The inside of a QUIET Q-band polarimeter. With reference to the schematic given in Figure 2.13, one can trace the path of light from the waveguide inputs to the detector diodes. Photo of QUIET Q-band polarimeter courtesy of Laura Newburgh.

components, and the amplifier stages are arranged in this configuration as a compromise. The total noise (N_T) of a linear multi-component system can be described using

$$N_T = N_1 + \frac{N_2}{G_1} + \frac{N_3}{G_1 G_2} + \ldots, \tag{2.5}$$

where N_i and G_i are respectively the noise and gain of the i^{th} component. In order to minimize N_T, it is desirable to have the first component be low-noise and high-gain, as the noise from the first component is small and the noise from the second component (and components thereafter) is suppressed (due to dividing the noise of subsequent components by the gain of the first component). If all the LNAs are put after the phase-switch,

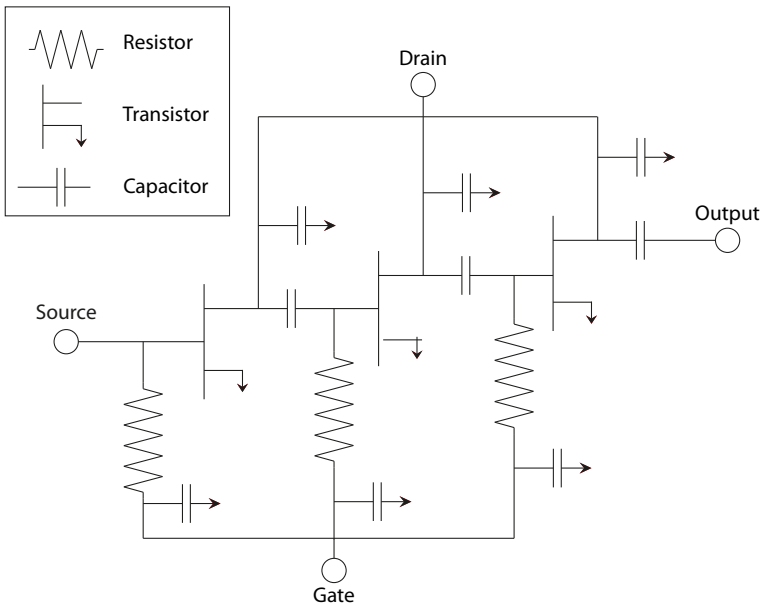

Figure 2.15: A schematic diagram of a Q-band LNA. The HEMT transistors are set up in a three-stage cascading design.

any loss in the signal due to the phase-switch will be amplified as noise; if all the LNAs are put before the phase-switch, the impedance change associated with the phase-switch will interact with the hybrid coupler, and the loss from the phase-switch will exacerbate any problems with compression (§2.3.4.4). For these reasons, it is determined that the optimal configuration to maximize the incoming signal is to have two LNAs before and a third LNA after the phase-switch.

Each LNA amplifier requires a bias current for its drain and a bias voltage for its gate. In order to achieve optimal noise performance from each amplifier, the amplifiers are

cryogenically cooled to $\sim$20 Kelvin, and the bias current and voltage of each amplifier is individually tuned. Each Q-band polarimeter has two more bias lines than the W-band polarimeter; this is because the drains for the W-band polarimeter's second and third stage amplifiers are tied together, whereas the respective Q-band drains are not.

2.3.1.2 Phase-Switches

Phase-switches are active components that are capable of altering the path length which a signal traverses. Each phase-switch consists of a long and short path (one open and one closed, depending on the bias current being applied to the phase-switch component at the time) that differ in length by a distance of $d = \lambda/2$, where λ is the wavelength of the signal.

If a wave that traverses the short path is

$$\psi = E_X + iE_Y, \tag{2.6}$$

then the wave that traverses the long path is

$$\psi' = -E_X - iE_Y. \tag{2.7}$$

In theory, if the signal is evenly split between the short and long paths, the signal will interfere destructively upon recombination and its magnitude will be zero. In practice, due to the open/closed nature of the phase-switch design, the signal only traverses one path at a time. A diagram showing the schematic for a phase-switch can be seen in Figure 2.16.

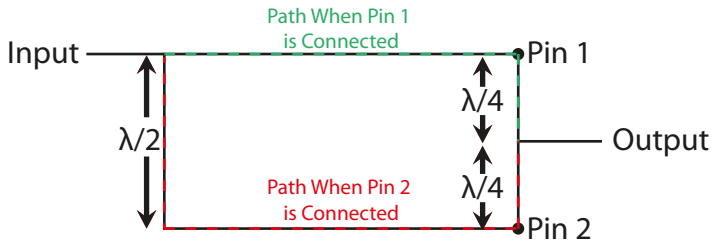

Figure 2.16: A schematic diagram of a phase-switch. When the phase switch is connected via pin 2, the incident wave travels an extra $\lambda/4$ down and up, giving a total path difference of $\lambda/2$ compared to when the phase switch is connected via pin 1.

Each polarimeter has a phase-switch that operates at a frequency of 50 Hz (input A), and a phase-switch that operates at a frequency of 4 kHz (input B)[9].

[9]The two phase-switches frequencies are chosen for the following reasons: 4 kHz modulation is fast enough to ensure that the observed polarization is not distorted by the scanning rate of the telescope or by moving weather patterns at the site, and acts to characterize drifts in the gains of the amplifiers; the 50 Hz modulation rate is set by the data acquisition rate of our electronic cards (which can process data at a maximum frequency of 800 kHz), and is used to remove imbalances in power from the two inputs.

2.3.1.3 Hybrid Couplers

Each QUIET polarimeter has two hybrid couplers. The hybrid couplers take the phase-switched signals from inputs A and B and transform them into $\mathbf{Q}/\mathbf{U}$ polarization signals to be detected by the QUIET detector diodes. The first (180°) hybrid coupler combines the input from inputs A and B of the QUIET polarimeter, and outputs a signal E_{180A} that is proportional to the signal from input A plus the signal from input B ($E_{180A} \propto E_A + E_B$), and a signal E_{180B} that is proportional to the signal from input A plus a 180° phase-shifted signal from input B ($E_{180B} \propto E_A - E_B$). Similarly, the second (90°) hybrid coupler combines the inputs from inputs A and B, and the coupler outputs a signal E_{90A} that is proportional to the signal from input A plus a 90° phase-shifted signal from input B ($E_{90A} \propto E_A + iE_B$), and a signal E_{90B} that is proportional to the signal from input A plus a 270° phase-shifted signal from input B ($E_{90B} \propto E_A - iE_B$). The derivation, showing how these signals represent Stokes $\mathbf{Q}/\mathbf{U}$ polarizations, is provided in §2.3.2.

2.3.1.4 Bandpass Filters

Bandpass filters are located immediately after the third-stage amplifiers, and immediately before the detector diodes. Bandpass filters are used to remove any spurious signals from reaching the detector diodes that are outside of the QUIET Q- (W-) band frequency range.

2.3.1.5 Power Splitters

After the signal passes through the 180° coupler, a 3 db power splitter divides the signal, with half of the signal going to a pair of detector diodes, and the other half continuing on

to the 90° coupler.

2.3.1.6 Detector Diodes

After the signal is processed by the LNAs, phase-switches, hybrid couplers and filters, it is terminated on one of the four detector diodes inside the polarimeter. The QUIET detector diodes are Agilent HSCH-9161 zero-bias Schottky diodes made from gallium arsenide (GaAs). The response of a Schottky detector diode is modeled (Pozar, [28]) using the equation

$$I = I_S \left(e^{\alpha(T)V} - 1 \right), \tag{2.8}$$

where I_S is the saturation current, and $\alpha(T)$ is a parameter that depends on the temperature T of the diode and the material from which it is constructed. A sketch of a typical $I(V)$ curve for a Schottky diode is shown in Figure 2.17. By rearranging equation (2.8), a formula for the voltage V is achieved:

$$V = \frac{\ln\left(I + I_S\right) - \ln\left(I_S\right)}{\alpha\left(T\right)}. \tag{2.9}$$

Furthermore, the voltage of a Schottky detector diode may be expressed using

$$V = V_0 + v\cos\left(\omega t\right), \tag{2.10}$$

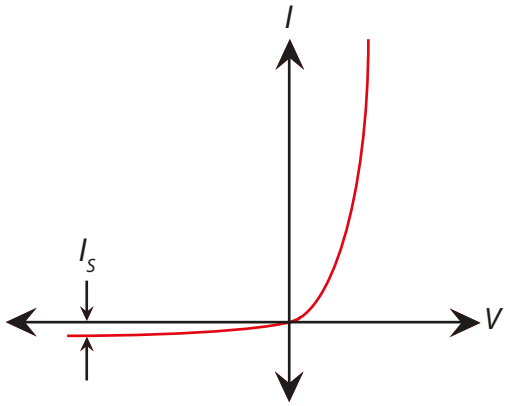

Figure 2.17: A sketch of a typical $I(V)$ curve of a Schottky diode, with the current I plotted in red as a function of the voltage V.

where V_0 is a DC bias voltage and $v\cos(\omega t)$ is a small signal RF voltage. By using a Taylor expansion about V_0, equation (2.8) becomes:

$$\begin{aligned} I(V) = I_0 + v\alpha(T) I_S e^{\alpha(T)V_0}\cos(\omega t) \; + \\ \frac{v^2}{2}\alpha(T)^2 I_S e^{\alpha V_0}\cos^2(\omega t) + O\left(v^3\right) + \ldots \end{aligned} \tag{2.11}$$

The first derivative of the current with respect to the voltage defines the junction resistance of the diode, R, at $V{=}V_0$ using

$$\begin{aligned} R = \frac{dV}{dI} &= \frac{1}{(I + I_S)\,\alpha(T)} \\ &= \frac{1}{I_S e^{(\alpha(T)V_1)}\alpha(T)}, \end{aligned} \tag{2.12}$$

and equation (2.11) is simplified to:

$$I(V) = I_0 + \frac{v}{R}\cos(\omega t) + \frac{v^2\alpha(T)}{2R}\cos^2(\omega t) + O\left(v^3\right) + \ldots \tag{2.13}$$

The voltage change on the diode (in the small signal limit) is its junction resistance R multiplied by the induced current, and the rectified voltage on a detector diode can then be expressed as

$$\begin{aligned}\Delta V &= R\left(\langle \Delta I\rangle - I_0\right)\\ &= \frac{v}{R}\langle\cos(\omega t)\rangle + \frac{v^2}{2R}\alpha(T)\langle\cos^2(\omega t)\rangle + O\left(v^3\right) + \ldots\\ &= \frac{v^2}{4R}\alpha(T) + O\left(v^4\right).\end{aligned} \tag{2.14}$$

This implies that the measured voltage on a detector diode is proportional to the square of the incident RF signal E applied to it, and hence

$$V_{measured} \propto E^2. \tag{2.15}$$

2.3.2 Theory of Operation – Transforming L/R into Q/U in the QUIET Polarimeter

This section provides an overview of how the QUIET polarimeters transform L and R circularly polarized light into Stokes **Q** and **U** polarizations. For simplicity, consider the phase-switch in input A to be static, and the phase-switch in input B to modulate the signal between 0° and 180° phase-shifted states at a frequency of 4 kHz.

First, it must be noted that the gains of the two inputs of the polarimeter are not equal. Although it would be ideal for each input to have the same gain g, each of the LNAs has its own characteristics, and the signal in each input is multiplied by a gain coefficient corresponding to the combined three stages of amplifiers. In this derivation, we include gain non-idealities but disregard any phase mismatches occurring between the two inputs, or any noise generated by the active components in the polarimeter. Input A has a signal

$$E_{Input\ A} = E_X + iE_Y = L \tag{2.16}$$

and input B has a signal of

$$E_{Input\ B} = E_X - iE_Y = R. \tag{2.17}$$

The signals in inputs A and B become

$$E_{Input\ A} = g_A L, \tag{2.18}$$

and

$$E_{Input\ B} = \pm g_B R, \tag{2.19}$$

where a ($\pm$) factor in equation (2.19) is applied due to the modulation of the phase-switch in input B.

After the signals are amplified and phase-switched, the signals from inputs A and B are recombined by the hybrid couplers. At this point, each signal is split by a 3 db power splitter: half of the signal that does not undergo any phase shift is terminated on the Q1 diode, and half of the signal that undergoes a 180° phase shift is terminated on the Q2 diode. That is, the RF signal incident on the Q1 diode is

$$E_{\mathrm{Q1}} = g_A L \pm g_B R, \tag{2.20}$$

and the RF signal incident on the Q2 diode is

$$E_{\mathrm{Q2}} = g_A L \mp g_B R. \tag{2.21}$$

The two remaining half signals from the splitters (one in phase and one 180° out of phase) are coupled by the 90° coupler, which outputs components that are $\pm$90° out of phase. The portion of the signal that undergoes a 90° phase shift is terminated on the U1 diode and the portion of the signal that undergoes a -90° phase shift is terminated on the U2 diode. Hence, the RF signal incident on the U1 diode is

$$E_{\mathrm{U1}} = g_A L \pm i g_B R, \tag{2.22}$$

and the RF signal incident on the U2 diode is

$$E_{\mathrm{U2}} = g_A L \mp i g_B R. \tag{2.23}$$

Equation (2.15) shows that the voltage measured by a detector diode is proportional to the square of its incident RF signal E. The voltage measured by the Q1 diode is therefore

$$\begin{aligned} V_{\text{Q1}} &= \left|E_{\text{Q1}}\right|^2 \\ &= E_{\text{Q1}} E_{\text{Q1}}^* \\ &= \left(g_A L \pm g_B R\right)\left(g_A L \pm g_B R\right)^* \\ &= g_A^2 LL^* \pm g_A g_B LR^* \pm g_A g_B RL^* + g_B^2 RR^* \\ &= g_A^2\left(E_X^2 + E_Y^2\right) \pm g_A g_B\left(E_X^2 + 2iE_X E_Y - E_Y^2\right) \\ &\quad \pm g_A g_B\left(E_X^2 - 2iE_X E_Y - E_Y^2\right) + g_B^2\left(E_X^2 + E_Y^2\right) \\ &= \left(g_A^2 + g_B^2\right)\left(E_X^2 + E_Y^2\right) \pm 2g_A g_B\left(E_X^2 - E_Y^2\right) \\ &= \left(g_A^2 + g_B^2\right)\mathbf{I} \pm 2g_A g_B \mathbf{Q}. \end{aligned} \tag{2.24}$$

Similarly,

$$\begin{aligned} V_{\text{Q2}} &= E_{\text{Q2}} E_{\text{Q2}}^* \\ &= \left(g_A L \mp g_B R\right)\left(g_A L \mp g_B R\right)^* \\ &= \left(g_A^2 + g_B^2\right)\mathbf{I} \mp 2g_A g_B \mathbf{Q}, \end{aligned} \tag{2.25}$$

$$\begin{aligned} V_{\text{U1}} &= E_{\text{U1}} E_{\text{U1}}^* \\ &= \left(g_A L \pm i g_B R\right)\left(g_A L \pm i g_B R\right)^* \\ &= \left(g_A^2 + g_B^2\right)\mathbf{I} \pm 2g_A g_B \mathbf{U}, \end{aligned} \tag{2.26}$$

and

$$\begin{aligned} V_{\mathrm{U2}} &= E_{\mathrm{U2}} E^*_{\mathrm{U2}} \\ &= (g_A L \mp i g_B R)\,(g_A L \mp i g_B R)^* \\ &= \left(g_A^2 + g_B^2\right)\mathbf{I} \mp 2 g_A g_B \mathbf{U}. \end{aligned} \tag{2.27}$$

These are the signals produced on the four detector diodes when one phase-switch is static, and one is modulated between a 0° and 180° phase state. As the phase-switch in input B is modulated, the signal at each detector diode steps between $\pm 2 g_A g_B \mathbf{Q}$ or $\pm 2 g_A g_B \mathbf{U}$. By measuring the difference in the voltage of each detector diode as a function of time, Stokes $\mathbf{Q}$ and $\mathbf{U}$ polarizations can be calculated. The magnitude of $\mathbf{Q}$ and $\mathbf{U}$ polarizations is expected to change as a function of time due the movement of the telescope and local weather conditions at the site. The speed of phase-switching in input B (4 kHz) ensures that data is acquired at a rate much faster than changes in $\mathbf{Q}$ or $\mathbf{U}$ polarizations on the sky due to the movement of the telescope or due to changing weather patterns at the site.

The introduction of a second phase-switch in the operation (the 50 Hz phase-switch in input A), acts to add and difference the measured voltages on the detector diodes; this process is called *double-demodulation*. When the second phase-switch is modulated between 0° and 180°, the first terms in equations (2.24), (2.25), (2.26) and (2.27) remain the same, whereas the second terms of these equations flips sign. If the voltage measured in the averaged state is denoted by a *av* subscript (the averaged data time-stream), and the voltage measured in the differenced state by a *de* subscript (the demodulated data time-

stream), when the second phase-switch is turned on, the resultant voltages on the detector diodes in the averaged state are

$$V_{\mathrm{Q1}_{av}} = V_{\mathrm{Q2}_{av}} = V_{\mathrm{U1}_{av}} = V_{\mathrm{U2}_{av}} = \left(g_A^2 + g_B^2\right)\mathbf{I}, \tag{2.28}$$

and the resultant voltages on the detector diodes in the differenced state are

$$V_{\mathrm{Q1}_{de}} = \pm 2 g_A g_B \mathbf{Q}, \tag{2.29}$$

$$V_{\mathrm{Q2}_{de}} = \mp 2 g_A g_B \mathbf{Q}, \tag{2.30}$$

$$V_{\mathrm{U1}_{de}} = \pm 2 g_A g_B \mathbf{U}, \tag{2.31}$$

$$V_{\mathrm{U2}_{de}} = \mp 2 g_A g_B \mathbf{U}. \tag{2.32}$$

It can be seen from the above equations that the Stokes $\mathbf{I}$ parameter can be calculated from the measured voltages incident on the detector diodes in the *averaged* state, and the Stokes $\mathbf{Q}$ and $\mathbf{U}$ parameters can be calculated from the measured voltages incident on the detector diodes in the *differenced* state. The *averaged* state allows the absolute temperature, rather than the polarization, on the sky to be measured.

Because the QUIET LNAs are predisposed to $1/f$ gain drifts (at timescales on the order of $\sim$1 kHz), the demodulation process is important: the 4 kHz switching differences gain drifts from our data at longer timescales, and $1/f$ noise is reduced by a factor of

$\sim 10^4$ in the differenced data stream compared to the averaged data stream. The "double-demodulation" process further reduces the $1/f$ noise. A plot showing the average noise as a function of frequency for no modulation; single 4 kHz modulation in one input of the polarimeter; and "double-demodulation", consisting of 4 kHz modulation in one input and 50 Hz modulation in the second input, is shown in Figure 2.18.

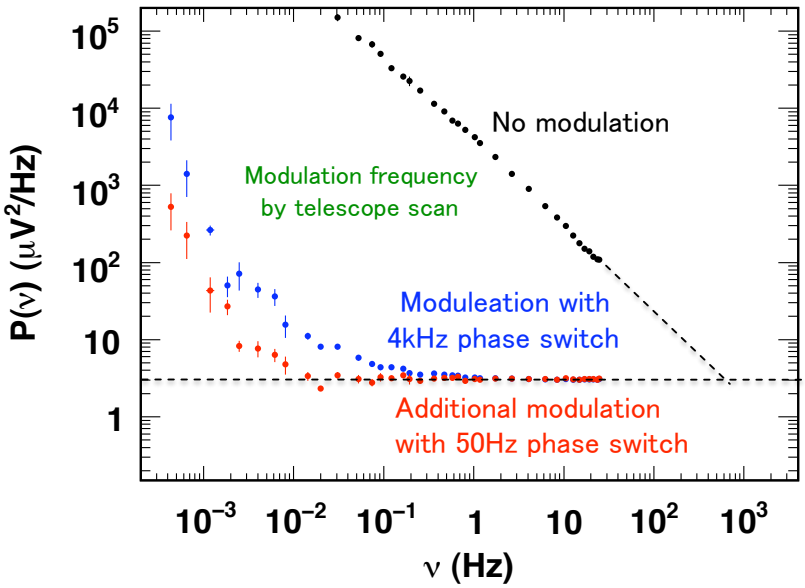

Figure 2.18: Typical noise spectrum for a W-band polarimeter. By itself, the single 4 kHz modulation reduces the $1/f$ noise by a factor of $\sim 10^4$ for a QUIET polarimeter; the "double-demodulation" (addition of the 50 Hz modulation) further reduces the $1/f$ noise in the polarimeter.

2.3.3 Total Power (Temperature) Assembly Detectors

As seen in §2.3.2, if the voltages on the polarimeter detector diodes are averaged, the resulting signal is proportional to Stokes parameter **I**. In practice, the averaged signal of the polarimeters is subject to large $1/f$ noise, making them ineffective at performing precision measurements of Stokes parameter **I**. Even though the main purpose of QUIET is to measure CMB polarization, the measured temperature signal of the CMB can be used for calibration (cross-checking the CMB temperature results with other experiments) and to assess many real-time observations at the site (such as the quality of the observing conditions at the site at a given time, since, the temperature signal fluctuates with weather conditions); for this reason, it is desirable to have a couple of polarimeters that are able to make high-sensitivity measurements of the CMB temperature signal.

QUIET polarimeters can be individually used to measure CMB polarization, or paired together to create total power assembly detectors which measure the difference in the absolute temperature observed between two adjacent horns. The Q- (W-) band array has 19 (91) polarimeters, with 1 (3) polarimeter pair(s) used to measure the absolute temperature differential of the sky, and the rest used to measure CMB polarization.

Instead of using an OMT septum polarizer that splits light into L and R components, an $X - Y$ OMT septum polarizer is used to split light into its X and Y components. After passing through the $X - Y$ OMT septum polarizer, the inputs to the hybrid-T are the following: the X polarization from the first feedhorn and the Y polarization from the

second feedhorn; and the Y polarization from the first feedhorn and the X polarization from the second feedhorn. The hybrid-T then outputs ($E_{Y1}+E_{X2}$) and ($E_{Y1}-E_{X2}$) to the first polarimeter and ($E_{Y2}+E_{X1}$) and ($E_{Y2}-E_{X1}$) to the second polarimeter. Once these inputs have been amplified and phase-switched in the polarimeter, the resulting demodulated signal is proportional to the difference in temperature seen by the two feedhorns, and a differenced measurement of Stokes $\mathbf{I}$ (no longer subject to high $1/f$ noise) is obtained. A diagram demonstrating the set-up of a pair of total power assemblies is shown in Figure 2.19.

Although the total power assemblies provide useful information for the Q- (W-) band analysis, they are not the focus of this thesis. The total power assemblies are occasionally mentioned in this thesis, but the results from the total power assemblies are not discussed.

2.3.4 The Imperfect (Actual) Polarimeter

§2.3.2 describes the theory of operation of an ideal polarimeter: the active components of the polarimeter do not produce any noise, the phase-switches perfectly modulate the signal between 0° and 180° phase states and do not incur loss, there is no $\mathbf{I} \rightarrow \mathbf{Q}/\mathbf{U}$ leakage, and the detector diodes do not suffer from compression. Actual polarimeters experience some or all of the above effects, and this must be taken into account in the analysis. This section describes how each of these imperfections are accounted for in the analysis. Each effect is treated as an independent effect that can be assessed separately.

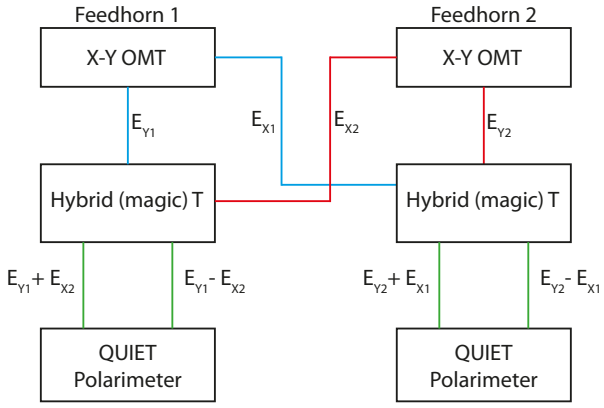

Figure 2.19: Diagram of a total power assembly detector pair setup, consisting of $X - Y$ OMTs, a hybrid-T, and two QUIET polarimeters.

2.3.4.1 Noise From Amplifiers and Active Components

Inputs A and B of a polarimeter will each have an associated intrinsic noise due to imperfections and their active components: the noise terms for inputs A and B are denoted as σ_A and σ_B respectively. For imperfect polarimeters these noise terms need to be added to the equations (2.18) and (2.19), (which are for ideal polarimeters) to produce

$$E_{Input\ A} = g_A L + \sigma_A, \tag{2.33}$$

and

$$E_{Input\ B} = \pm g_B R + \sigma_B, \tag{2.34}$$

This noise affects the signals incident on the Q1, Q2, U1 and U2 diodes, and therefore the voltages measured on these diodes. That is, for the imperfect polarimeter the relevant voltage equations are more complicated than shown in equations (2.24), (2.25), (2.26) and (2.27). The effect of this noise can be accounted for by characterizing the noise of each input using measurements taken over the course of the observing season[10].

2.3.4.2 Phase-Switch Imbalance

Phase switch imbalances occur when the difference between the signal that traversed the long path is not 180° out of phase with the signal that traversed the short path. Phase switch imbalances can occur if the path difference in path length between the two paths is not $\lambda/2$, or if imperfections in the instrument (such as impedance mis-matches at waveguide inputs) or if the amplifiers (which, while are supposed to preserve the phase, are not perfect) cause a phase change. If the phase difference between the two phase-switch states is not 180°, but rather (180+χ)° where χ is the deviation in the phase angle from 180°, then equations (2.18) and (2.19) become

$$E_{Input\ A} = g_A L, \tag{2.35}$$

[10]Given that the $\mathbf{Q}/\mathbf{U}$ polarization signals measured by the detector diodes are produced from a combination of inputs A and B, some of the amplifier noise sources are correlated, and corrections need to be computed and accounted for.

and

$$E_{Input\ B} = \pm e^{i\chi} g_B L. \tag{2.36}$$

In order to account for this effect, the polarization angle χ of each polarimeter diode is measured. The process by which the polarization angle is determined is outlined in §4.3.

2.3.4.3 I → Q/U Leakage

The description of the ideal polarimeter does not take into account that some of the Stokes **I** (temperature signal) from the sky/source is converted into Stokes **Q**/**U** polarizations due to non-idealities in the instrument. This effect is known as *leakage*. The method by which the leakage of each detector diode is measured is outlined in §4.4.

2.3.4.4 Compression

For ideal performance, the detector diodes should be operated in a linear regime; that is the measured detector diode voltage should increase linearly with the incident RF power.

Figure 2.20 shows a sketch of the output voltage of the detector diode as a function of the incident RF power, identifying regions where the detector diode behaves linearly and non-linearly. If the incident power is greater than I_0, then output voltage will not be related to the incident RF power by the normal linear relationship. and the measurement is affected by signal compression.

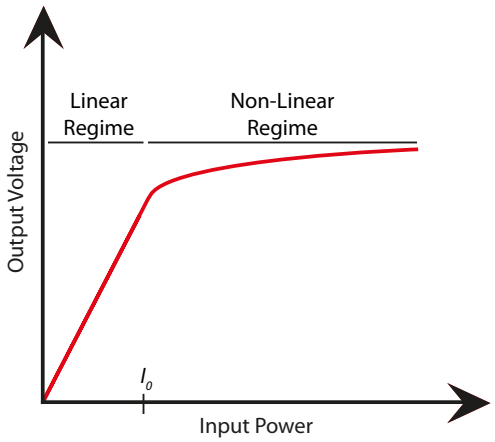

Figure 2.20: Sketch of the measured voltage on a detector diode as a function of the incident input power.

Throughout the Q-band season the effects of compression are not observed and therefore no data is removed from the analysis due to the effects of compression. Throughout the W-band season compression effects are significant and this affects polarimeter calibration. More on this subject is given in §4.2.3.

2.4 Signal Processing and Digitization

After a signal is measured on a polarimeter detector diode, it is transmitted from the cryostat to the electronics enclosure where it is processed by the electronics and data acquisition software. This section describes the electronics needed to bring the signal from the polarimeters in the cryostat to the processor; a diagram of the these electronics (for

the Q-band array) is shown in Figure 2.21.

QUIET polarimeters interface to module attachment boards (MABs, §2.4.1) inside the cryostat and the signals are transmitted to the outside of the cryostat via flexible printed circuits (FPCs, §2.4.2). The FPCs connect to array interface boards (AIBs, §2.4.3), placed in a shielded aluminum box directly outside of the cryostat, which in turn connect to AIB cables, which bring the signals from the AIBs to the electronics enclosure (§2.4.4).

The QUIET electronics enclosure has two back-planes: the bias back-plane and the ADC back-plane. The bias back-plane houses the electronics boards that bias the polarimeters (bias boards, §2.4.5), and the housekeeping board (§2.4.6), which records the bias voltages/currents of the active components in the polarimeter and the data from the peripheral devices. The ADC back-plane houses the ADC boards (§2.4.7)) that perform the analog-to-digital conversion or the signal, and the GPS timing board (§2.4.8) that synchronizes the acquired data.

Once the analog-to-digital conversion is complete, the data is processed by the data acquisition software.

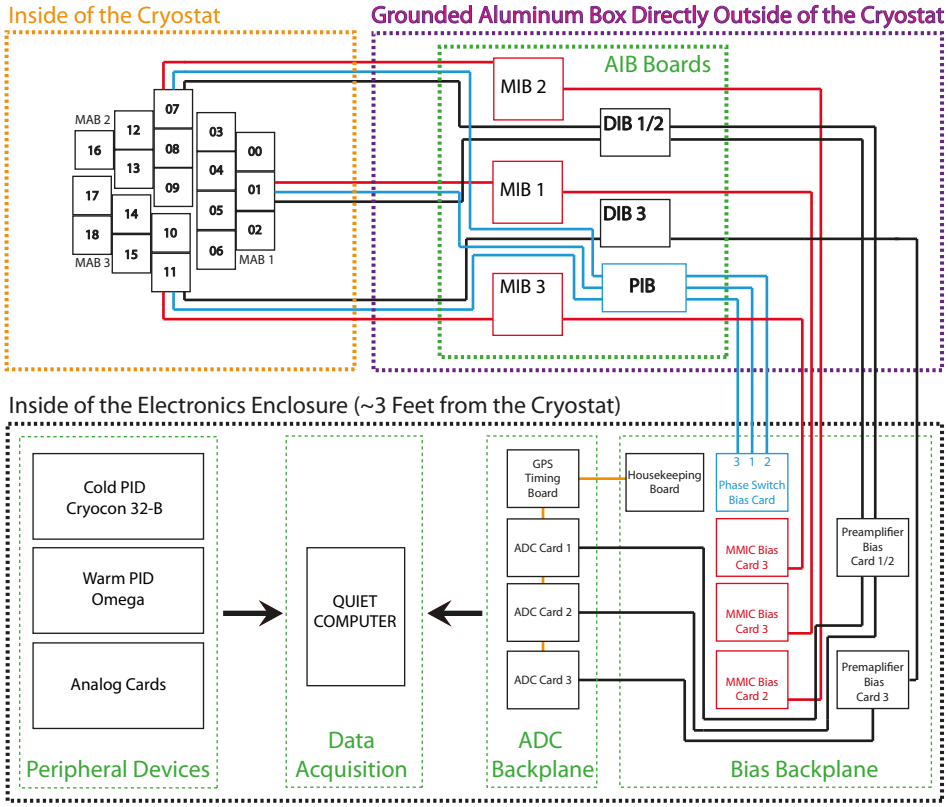

Figure 2.21: In this diagram, red lines represent LNA biases lines, blue lines represent phase-switch biases lines, black lines represent polarimeter diode biases/signals, and orange lines represent clock/timing signals. Boxes, in their respective colors, represent electronics boards associated with the particular bias/diode line mentioned. Biases from the LNA, phase-switch and preamplifier boards in the electronics enclosure are sent to the polarimeters in the cryostat via the MABs. The MABs also send the signals from the polarimeter diodes back to the electronics enclosure where they converted from analog to digital signals, and are acquired by the computer. In between the MABs and the electronics enclosure are the AIBs (MIBs, PIBs and DIBs – see §2.4.3). The signals between the MABs and AIBs are sent via FPCs; the signal between the AIBs and the electronics enclosure are sent via AIB cables.

2.4.1 Module Attachment Boards

Module attachment boards (MABs) provide the electronic interface between the polarimeters in the cryostat and the FPCs: the MABs connect the biases from the electronic bias boards in the electronics enclosure to the polarimeters and the measured voltages of the polarimeter detector diodes back to the electronics enclosure to be processed for data collection. The LNA and phase-switch components in the QUIET polarimeter can be broken or damaged from stray voltages or transients; for this reason, a set of protection circuitry for the LNA and phase-switch components is placed on the MABs. Each MAB supports six or seven polarimeters, and the grounds of each polarimeter on an MAB are tied to a common ground plane. The 19- (91-) element Q- (W-) band array consists of three MABs, each with a unique design (13 MABs, with five different designs). A diagram showing the MAB shapes for the Q-band array, and a photo of an MAB with polarimeters inserted in it is shown in Figure 2.22.

The protection circuitry for the LNA and phase-switch bias lines consists of a voltage clamp and a filtering capacitor. The voltage clamps ensure that transient signals (such as static shocks during assembly) do not cause LNA or phase-switch component failures. The W-band protection circuitry is similar to that for the Q-band, but the diodes, LEDs, resistors and capacitors are selected to meet the specifications of the W-band LNAs and phase-switches.

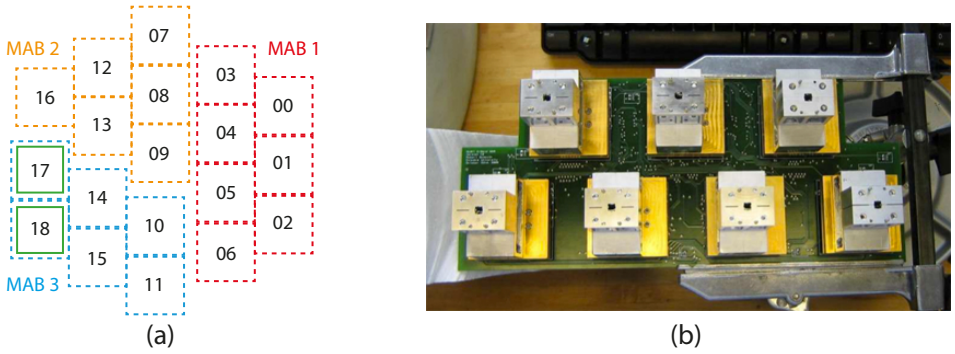

Figure 2.22: Q-band MABs. (a) The 19-element Q-band array is separated into three MABs (1: red, 2: orange, 3: blue), with the position of each polarimeter numbered from 00-18. The total power assembly detectors, in positions 17 and 18, are each denoted with an additional green box. (b) A photo of 7 Q-band polarimeters (with septum polarizers attached) inserted into MAB 1. Photo of MAB and polarimeters courtesy of Ross Williamson.

2.4.1.1 Gate and Drain Bias Protection

The gate and drain bias protection consist of a voltage clamp, which limits the bias to the gates and drain of the polarimeter ([-0.4:0.4] V and [-0.6:1.5] V respectively) and a 1 μF shunt capacitor to protect against fast transients ($>$ 100 Hz).

2.4.1.2 Phase-Switch Protection

The phase-switch is protected using a voltage clamp, which limits the bias to the phase-switch of the polarimeter ([-3.0, 1.43] V), and a low-pass RC filter (with a 1 pF capacitor) to protect against fast transients ($\gtrsim$ 1 MHz).

2.4.1.3 MAB interface to Flexible Printed Circuits

Zero-insertion force (ZIF) connectors (40-pin surface mount connectors, purchased from HiRose) are used to interface the MABs to the FPCs.

2.4.2 Flexible Printed Circuits

Flexible printed circuits carry the diode signals and bias lines from the MABs inside the cryostat to the AIBs directly outside of the cryostat. Each Q- (W-) band MAB has two FPCs dedicated to carrying diode signals, three (two) FPCs dedicated to carrying LNA biases[11], and one FPC dedicated for carrying phase-switch biases. The FPCs interface with the ZIF connectors on the MAB (at a temperature of $\sim$20 Kelvin) and are routed through hermetic connectors to the AIBs (at a temperature of $\sim$270 Kelvin) on the back of the cryostat. FPCs consist of copper traces set in between layers of Kapton; Kapton is chosen due to the large range of temperatures that the material can withstand. The FPC's are 32" long, the length required to connect the MABs inside the cryostat to the AIBs outside of the cryostat.

2.4.3 Array Interface Boards and Cables

Protection circuitry located on the MABs provides protection of the LNA and phase-switch components of the polarimeter from transient signals during the integration and

[11]The Q-band MAB has an additional FPC for carrying LNA biases due to the additional third-stage drain bias lines.

set-up of the QUIET receivers. When the Q- or W- band array is cooled down, so are the MABs and protection circuitry. The diodes and LEDs used for the MAB protection circuitry are not specified to operate at the cryogenic temperature of the array ($\sim$20 Kelvin), so if a transient signal is to propagate into the array when it is cold, it can damage a LNA or phase-switch. In order to provide additional protection to the LNAs and phase-switches of the QUIET polarimeters, the voltage clamps from the MAB protection circuitry are replicated on the array interface boards (AIBs) on the outside of the cryostat (in an environment for which the voltage clamps are specified to operate). The AIBs take the signals from the FPCs and output them to AIB cables. Three types of AIBs are constructed: MMIC (LNA) interface boards (MIBs) provide additional protection to the gates and drains of the LNAs; phase-switch interface boards (PIB) provide additional protection to the phase-switch components; and diode interface boards (DIBs) interface the FPCs to the AIB cables.

AIB cables transfer the signals from the AIBs to the backplane of the electronics enclosure, and consist of two custom-made rigid printed circuit boards (one attaching to the AIBs, and the other attaching to the electronics enclosure) connected to one another using shielded ribbon cable.

2.4.4 The Electronics Enclosure

The electronics enclosure is located on the QUIET mount, in close proximity ($\sim$3 feet) to the cryostat. The electronics enclosure houses the electronics required to bias the polarimeter array and record their data, and the devices used to monitor/regulate the array and enclosure: the bias and ADC backplanes, to which the preamplifier, LNA bias, phase-switch bias, housekeeping, GPS and auxiliary timing, and ADC boards are attached (all of which are 6U VME boards); the QUIET computer, which is used for data acquisition; and peripheral devices, including the cold PID, which regulates the temperature of the cryostat, the warm PID, which regulates the temperature of the electronics enclosure; and the analog boards, which record the data from the outer temperature sensors. The electronics enclosure is approximately 7' $\times$ 2' $\times$ 3', and is water- and weather- proof and thermally controlled.

2.4.5 Bias Boards

The preamplifier boards have the capability to bias the polarimeter diodes for operation, and to amplify the output signal before it is processed by the analog to digital conversion boards. The signal is amplified by a factor of $\sim$130, which is selected in order to be capable of exploiting the full range of the analog to digital converter chips on the ADC electronics boards. Each preamplifier board is capable of servicing two MABs.

The LNA bias boards provide the bias to the gates and drains of the LNAs. The LNA bias board is divided into two halves, with each half ideally being capable of biasing

seven polarimeters (or a single MAB). Because the third LNA of each Q-band polarimeter requires an individually tuned drain current, each Q-band MAB uses one half of the LNA bias board to bias the third-stage drains of the polarimeters of an MAB, and the other half to bias the rest of the gates and drains of the polarimeters of an MAB.

The phase-switch bias boards provide bias to the phase-switch components in the polarimeter, simultaneously providing a forward bias to one input of the phase-switch and a reverse bias to the other. When the biases to the phase-switch are flipped, the resulting phase change in the signal is 180°. In normal operation, a QUIET polarimeter will have one input being phased-switched at 50 Hz and the other at 4 kHz. Each phase-switch bias board is capable of servicing three MABs.

2.4.6 Housekeeping Electronics Board

The biases produced by the LNA bias and phase-switch bias cards are measured as a voltage. The housekeeping electronics boards records these voltages, the voltages from 12 silicon diode temperature sensors in the cryostat and 12 thermistors in the electronics enclosure, as well as the voltage from the pressure sensor (capacitance manometer) attached to the cryostat. There are a total of 491 (1774) voltages to be measured for the Q- (W-) band receiver. The housekeeping board multiplexes these voltages and converts them to digital signals using an on-board analog-to-digital converter. The multiplexer operates at a frequency of 497 Hz, which results with a sample frequency of $\sim$1 Hz ($\sim$0.3 Hz) for

the Q- (W-) band receiver for each voltage recorded.

2.4.7 Analog to Digital Conversion Boards

The Analog to Digital Conversion boards, along with the GPS timing board, are attached to the ADC back-plane and are housed in a Wiener Series 6000 VME crate. In order to interface with the ADC boards, the Wiener crate requires a crate computer VME board (GE vmivme-7700). The ADC boards are built around an Altera field-programmable gate array (FPGA), which gathers and processes data from 32 successive-approximation 18-bit ADCs[12]; the quickness of the successive-approximation algorithm allows an 800 kHz sampling rate of each polarimeter detector diode.

The ADC cards are set up in a master-slave configuration; each card is identically manufactured, but the master is altered by the addition of jumper pins. The Q- (W-) band receiver requires one master ADC board and two (twelve) slave ADC boards. Although all of the ADC boards produce clock signals, it is the clock from the master ADC board that is used for time-stamping the data, as well as providing the clock signal for the ADC on the housekeeping board.

Radiometer data are acquired by the ADCs using a program on the ADC PC called adc_server which acquires data from the polarimeters at a rate of 800 kHz. Because the

[12] A successive-approximation ADC is one that converts an analog signal into a digital one by employing a binary search ($O(\log n)$ comparisons needed, using a divide-and-conquer algorithm) to determine the appropriate number of "bits" in a measured signal.

phase-switch operates at 4 kHz, 200 measurements are received from the first phase state and 200 measurements are received from the second phase state for each phase-switch cycle. The FPGA acquires an 800 kHz sample for all channels and passes them to a registrar in the CPU for storage, where for each channel an *averaged* (or *total power*) data time-stream is calculated (by returning the average of the first and second 200 samples), as is a *differenced* (or *demodulated*) data time-stream (by returning the difference of the sum of the first and second 200 data samples). The total power and demodulated time-streams are produced at a frequency of 100 Hz and stored in data files. Each ADC board is capable of servicing the data acquired from a single MAB.

2.4.8 GPS Timing Board

Data from the telescope and receiver are acquired independently. In order to synchronize the telescope and receiver data streams, a GPS timing board (Symmetricom TTM635VME) and a custom-made auxiliary timing board are used to synchronize the timestamps from the telescope and receiver. The telescope control sends a timestamp to the GPS timing card, which in turn sends a clocking signal to the auxiliary timing board; this clocking signal is then communicated to the back-plane and is received by the ADC boards.

2.4.9 Summary of Required Electronics

A summary of the electronics boards required for the Q- and W- band array is provided in Table 2.2

Board	Number of Boards Required	
	Q-band	W-band
MAB	3	13
MIB AIB	3	7
PIB AIB	1	5
DIB AIB	2	7
LNA bias	3	7
Phase-switch bias	1	5
Preamplifier	2	7
Housekeeping	1	1
ADC	3	13
GPS timing	1	1

Table 2.2: Electronics Boards Summary

2.5 Data Acquisition Software

The QUIET receiver PC, located in the electronics enclosure, runs the custom-built QUIET software to acquire data from the ADC cards in the VME crate (data_compilation, §2.5.1), bias the polarimeters (bias_server, §2.5.2), control the peripheral devices (peripheral_server, §2.5.3), and send commands to bias_server and peripheral_server (receiver_control, §2.5.4). This section describes the functionalities of the above programs. A schematic demonstrating how the receiver PC interfaces with the VME crate and peripheral devices is shown in Figure 2.23. The process by which the receiver and telescope data is processed at the site, stored, and sent from the site to the scientists for analysis is discussed in §2.5.5.

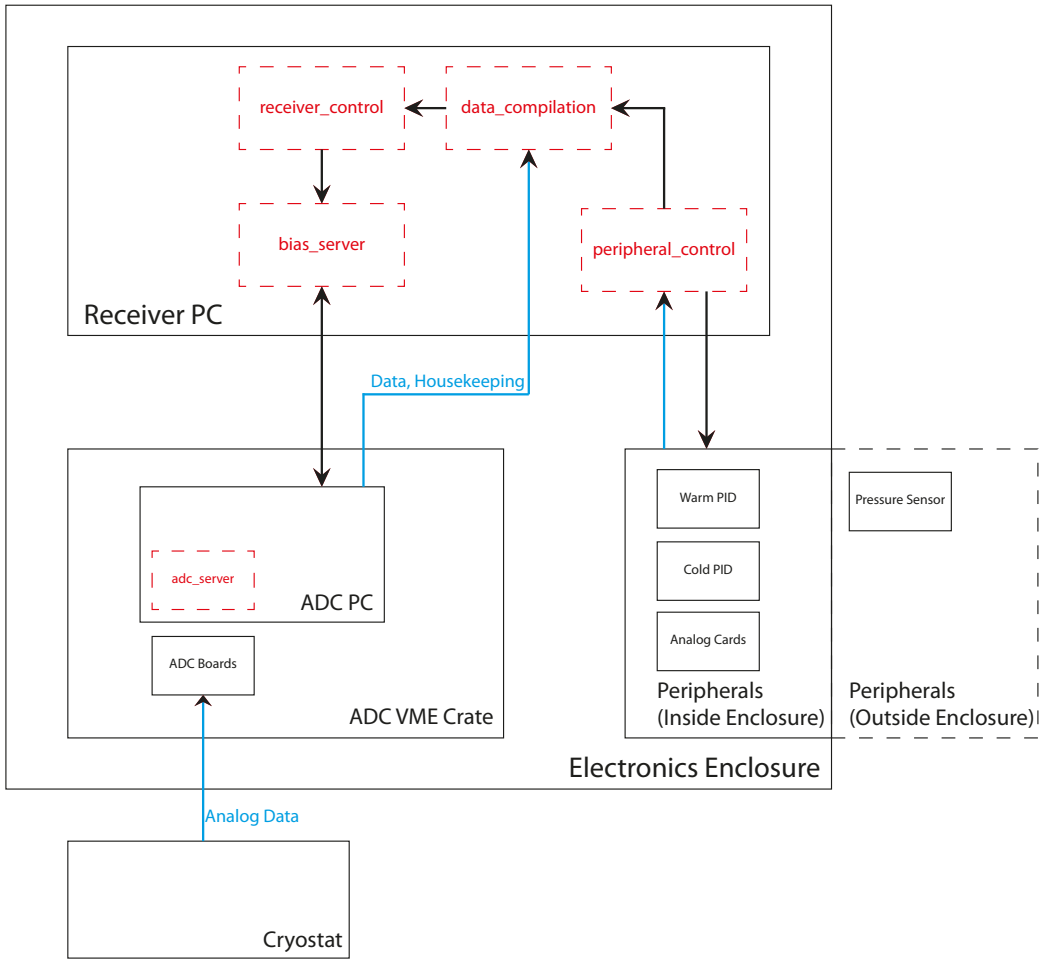

Figure 2.23: A schematic outline that summarizes the data flow. Boxes made of dashed red lines indicate a executable program, blue arrows represent data being sent, and black arrows represent commands being sent.

2.5.1 data_compilation

The data_compilation program is used to acquire data from the ADC PC (which collects data from the ADC boards) and peripheral devices. data_compilation acquires radiometer data at a rate of 100 Hz, and housekeeping and peripheral data at a rate of $\sim$1 Hz. Data is acquired from the ADC PC and is stored in archive registers and subsequently written to a data file on the receiver PC. Once the data in the archive registers have been stored, the completion of the action is communicated to the ADC PC and the data is deleted from the memory of the ADC PC.

2.5.2 bias_server

bias_server receives bias and housekeeping commands from receiver_control and sends them to the ADC PC. Bias commands are processed by the ADC PC and communicated to the LNA bias, phase-switch bias, and preamplifier boards, which adjust the biases to the polarimeters. In order to cycle through the housekeeping biases and temperature values, housekeeping commands are processed by the ADC PC and sent to the multiplexer on the housekeeping board; the multiplexer adjusts the address which it is pointing to, such that the requested bias/temperature can be measured.

2.5.3 peripheral_server

peripheral_server is used to acquire data and send commands to the peripherals. peripheral_server communicates with the Wiener VME crate; the PID that regulates the temperature of the cryostat fridges (the cold PID, which is operated using a Cryocon 32 B cryogenic temperature controller); the PID that regulates the temperature of the electronics enclosure (the warm PID, which uses a fan and heater that are operated by an Omega CNi16D22-El temperature controller); and the analog boards, which record the data from the outer temperature sensors.

All the peripherals, are capable of sending data to and receiving commands from peripheral_server. Data from the peripherals is acquired at a frequency of $\sim$1 Hz.

While most of the peripheral devices rarely exhibited communication failures, a monitor program is used to test whether or not the peripherals are properly functioning, and to automatically restart peripheral_server when needed.

2.5.4 receiver_control

Commands sent to bias_server and peripheral_server are interfaced via a command-line prompt called receiver_control. These servers execute their main programs, and periodically check to see whether or not a command has been sent. If a command is sent, the server will execute the command and send the updated results/parameters back to

data_compilation.

2.5.5 Data Processing and Data Transmission

Once a file is stored on the receiver PC, the file is sent via ethernet to the mount PC. The mount PC, located in the control room at the site, has enough hard-disk storage space to be able to store several months (several weeks) of Q- (W-) band receiver data. At this stage the receiver data, which is not yet synchronized with the telescope data, is said to be in level-0 format.

Once the data is stored on the mount PC, the copy of the receiver data is deleted on the receiver PC to free up hard-disk space for newly recorded receiver data (the receiver PC is only able to store a few days of receiver data at a given time). The level-0 receiver and telescope data is subsequently burned to disc and sent to the United States via mail. The data is then stored on a $\sim$10 TB array at the University of Chicago, and a level-1 format file is processed, synchronizing the receiver and telescope data. The data is then backed up at KEK in Japan, MPIfR in Germany, and at the University of Oslo. After the data is stored and backed up, the data is deleted from the mount PC at the site. For observations that need expedited analysis, level-1 processing is performed on the mount computer at the site and the resulting level-1 data files are sent to the United States via ethernet connection. Due to bandwidth limitations, this method of transfer is not feasible for a large percentage of data.

2.6 Salient Characteristics of the QUIET Instrument

Table 2.3 summarizes the salient characteristics of the QUIET instrument.

Band	Q	W
Frequency/GHz	43	95
# of Detectors	17 Pol. & 2 TT	84 Pol. & 6 TT
Telescope	Cross-Dragone	
Angular Resolution/arcmin	27.3	12.2
ℓ range	$25-475$	$\sim 25-1000$
Instrument Sensitivity/$\mu\mathrm{K}\sqrt{s}$	64	85

Table 2.3: Salient Characteristics of the QUIET Instrument

Chapter 3

Observations

This chapter describes the QUIET site (§3.1), the Q- and W- band observing seasons (§3.2), and the fields and calibration sources QUIET observes (§3.3 and §3.4 respectively).

3.1 The QUIET site

QUIET observations are performed on the Chajnantor Plateau in the Atacama Desert of Northern Chile (67 deg 45′ 42″ W, 23 deg 1′ 42″ S), using the site and facilities from the former CBI experiment (hereafter QUIET site and facilities). The site is located at an altitude of 5080 m (∼16700 ft) above sea level, and the typical optical depth of the atmosphere in the QUIET Q- and W- frequency bands is about 0.01 - 0.02 (shown in Figure 3.1). The extreme aridity of the desert combined with the high altitude of the site yield very little water vapor in the atmosphere and generally calm weather patterns. This results in excellent conditions for performing CMB polarization measurements, and makes the

Atacama Desert one of the world's premiere sites for radio-astronomy observation.

A weather station, capable of measuring the local real-time relative humidity, atmospheric pressure, ambient temperature, and the speed and direction of the wind is set up at the site. QUIET uses precipitable water vapor (PWV) measurements from the 183 GHz line radiometer of the Atacama Pathfinder EXperiment (APEX) weather station, which is located at a similar altitude and within 2.5 km of the QUIET site.

Apart from short periods of poor weather (usually lasting up to a few days) during the hotter and wetter summer months (late December to early March), weather conditions at the site permit year-round observations; QUIET observations are performed 24 hours a day, except when interrupted by mechanical failures or poor weather. In the event of an interruption, the QUIET instrument is covered by a retractable dome, which shields the instrument from harsh weather, and the receiver and telescope from direct exposure to the Sun.

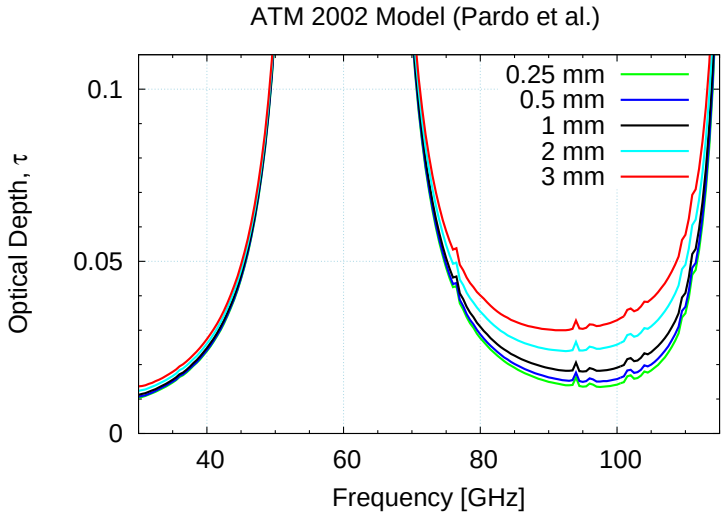

Figure 3.1: Optical depth at the Chajnantor Plateau (5000 m) for a ground temperature of T=273 K at various values of PWV, calculated using the ATM atmospheric model [29].

3.2 Q- and W- Band Observing Seasons

A test integration of the telescope, absorbing ground screen, and Q-band receiver was conducted at the California Institute of Technology in April–June 2008. The experiment was then shipped to the QUIET site, arriving in late July 2008. The Q-band receiver, which had been shipped in an assembled state, was re-tested at the site and the instrument was subsequently deployed. During the Q-band observing season, 2008 October – 2009 June, approximately 3500 observing hours were recorded, including more than 2650 hours of CMB field observations. During the Q-band observing season the mean PWV at the site was 1.2 mm. In July 2008 a suite of end-of-the season calibration measurements was performed prior to removal of the Q-band receiver from the mount and the installation of the W-band receiver.

After on-site testing and installation, the W-band receiver was deployed. During the W-band observing season, 2009 August – 2010 December, approximately 7600 hours of observations were recorded, including more than 5360 hours of CMB field observations. During the W-band observing season, the mean PWV at the site was 1.0 mm. A histogram of the recorded PWV from the APEX weather station during the Q- and W- band observing seasons (each histogram is normalized in time over its respective observing season) is shown in Figure 3.2.

A summary of the integration times on each CMB field during the Q- and W- band

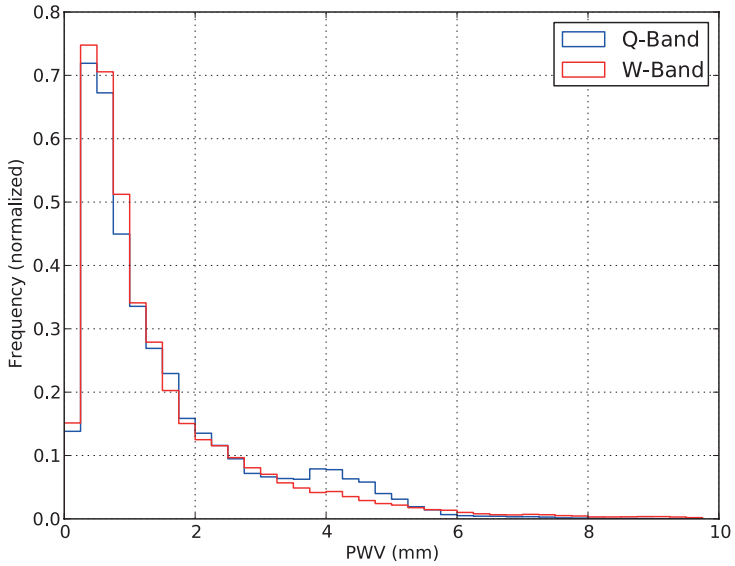

Figure 3.2: Normalized Histogram of PWV values over the duration of the Q- and W-band observing seasons.

observing seasons is provided in Table 3.1.

Field	Q-band (hours)	W-band (hours)
CMB-1	905	1869
CMB-2	703	1464
CMB-3	837	1382
CMB-4	223	652
Total	2668	5367

Table 3.1: Summary of CMB field Observations.

3.3 Observing Fields

QUIET observations are performed on four CMB fields and two Galactic fields, with each field having an area of approximately $15^\circ \times 15^\circ$ on the sky; this provides a total CMB field coverage close to 1000 square degrees. The number of CMB fields is selected to be the smallest number to provide continuous (24-hour) CMB coverage, such that at least one CMB field is in the observing horizon[1] at any time, while minimizing the amount of observed foreground radiation. The QUIET observing fields are shown on the celestial sphere in Figure 3.3; the physical locations of the fields are given in Table 3.2. The Galactic fields are not the subject of this thesis and will not be discussed further.

[1] As seen in §2.1, the elevation of the mount is restricted to $43^\circ < \theta < 85^\circ$.

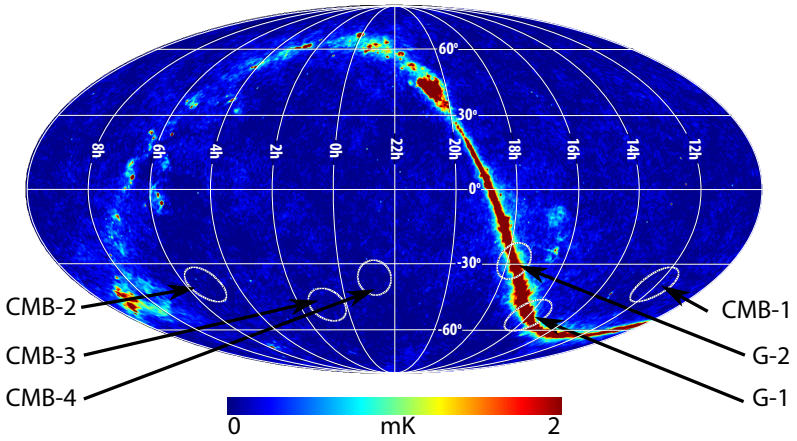

Figure 3.3: CMB and Galactic fields observed by QUIET, superimposed on an equatorial coordinate Q-band all-sky WMAP 7-year temperature map (data courtesy of the WMAP Science Team). The Galactic-plane temperature signal saturates the color-scale of this map. G-2 is at the Galactic center, and CMB-1 is the CMB field closest to to the Galactic center.

Field	RA	Dec.
	(J2000)	
CMB-1	12^h04^m	$-39°\ 00'$
CMB-2	05^h12^m	$-39°\ 00'$
CMB-3	00^h48^m	$-48°\ 00'$
CMB-4	22^h44^m	$-36°\ 00'$
G-1	16^h00^m	$-53°\ 00'$
G-2	17^h46^m	$-28°\ 56'$

Table 3.2: Observing Field Locations.

3.3.1 Scan Strategy

In order to scan the CMB fields though a constant atmospheric depth, a constant-elevation scan (CES) is employed. A CES involves scanning back and forth in azimuth at a fixed elevation (and fixed deck) as the field drifts through the scan region by sidereal motion. The amplitude of each azimuth scan is 7.5° on the sky, with each scan having a period

of 10–22s. The elevation of the mount is set to be 7.5° above or below the field to be observed (depending on whether the patch was rising or setting) and these azimuth scans are repeated for 40–90 minutes, the time taken for the field to drift through 15° in elevation on the sky. Once the CES is complete, the elevation is changed and a new CES is begun. During the Q- (W-) band season, CMB fields are observed using four (seven) deck angles, spaced at 45° increments: a 45° rotation on the sky rotates Stokes $\mathbf{Q}$ into Stokes $\mathbf{U}$ parameters. By stepping the deck at 45° increments, the signal seen in a $\mathbf{Q}/\mathbf{U}$ detector diode of a polarimeter is rotated into its other detector diodes: this strategy is implemented to reduce systematic errors. Diurnal sky rotations and weekly deck rotations provide uniform parallactic-angle coverage of the fields.

3.4 Calibration Sources and Methods

The following calibration parameters are obtained from celestial sources in the sky, the atmosphere, and a polarizing wire-grid: the responsivity of the detector diodes, the relation between the voltage measured by the detector diode and the temperature of the source that it is observing (for both the averaged and differenced data time-streams); the polarization angle of each detector diode (with respect to Stokes parameters $\mathbf{Q}$ and $\mathbf{U}$); and the observed leakage from Stokes $\mathbf{I}$ intensity to Stokes $\mathbf{Q}$ and $\mathbf{U}$ polarizations ($\mathbf{I} \rightarrow \mathbf{Q}/\mathbf{U}$).

QUIET calibration sources are divided into two types: absolute and relative. Absolute calibrators are those used to determine the absolute magnitudes of the calibration parameters. Relative calibrators are those used to relate the calibration parameters of a given

polarimeter diode to that of a reference diode: for each array, the reference diode is the Q1 diode on polarimeter 09 and 45 for the Q- and W- band arrays respectively.

3.4.1 Absolute Calibration Sources

Absolute calibration of the total power assembly detectors and polarization detectors is accomplished using bright compact sources (Jupiter, RCW 38 and Venus for the total power assembly detectors, and Taurus A for the polarization detectors). Each absolute calibration source, and the calibration parameters obtained from it, is described in this section.

3.4.1.1 Total Power Assemblies

Over the Q- band frequency range, the interpolated antenna temperature of RCW 38 is 45 ± 1.4 mK[2], and the interpolated temperature of Jupiter and Venus, due to the varying distances of the planets from the Earth, are 40-75 mK and 40-300 mK respectively[3]. Jupiter/(RCW 38)/Venus measurements are referenced to the (five-year WMAP [30])/(CBI [31])/(VSA [32]) result[4]. The QUIET beam sizes at the Q- and W- band frequencies are $27'.3$ and $12'.2$ respectively. Since the angular area of each of the sources is much smaller than both the Q- and W- band beam sizes, they are modeled as compact point sources in

[2]The antenna temperature differs slightly from diode to diode, depending on the specific diode central frequency and bandwidth.

[3]Errors on Jupiter/Venus are at most 1%/3% at any time. At the time of writing, W-band analysis of the Jupiter/(RCW 38)/Venus antenna temperatures is incomplete, and therefore omitted.

[4]Since the QUIET Q-band frequency is different than that of WMAP, VSA and CBI, the results are linearly interpolated to the QUIET Q-band frequency.

the beam; RCW 38 has the largest angular area of the three sources, measuring $\sim 1.8' \times 1.8'$ [31].

Each source is observed (roughly once a week) using a *raster scan*. The raster scan takes $15 - 30$ minutes to complete and involves scanning back and forth over the source in azimuth 3°, while stepping 0.1° at the end of each azimuth scan: this concentrates the observing time on an individual horn (or subset of horns), allowing sufficient sensitivity for our calibration purposes in the available integration time. The demodulated responsivity of a source and $\mathbf{I} \rightarrow \mathbf{Q}/\mathbf{U}$ leakage are obtained by binning the differenced time-ordered data from the observation to create a map, and by fitting separate two-dimensional Gaussian fits to the positive and negative peaks of the map (total power assembly detectors (§2.3.3), which measure the absolute temperature difference observed by a pair of polarimeters, observe a positive and negative peak in each map). A fit is performed on the map $\mathcal{F}_{\mathcal{S}}$ created from the differenced data time-stream of the total power assembly detector diodes using

$$\mathcal{F}_{\mathcal{S}} = R_S \left(T_S e^{\left(-\frac{\tau}{\sin\theta}\right)} \right) + \mathcal{F}_{\mathbf{I}\rightarrow\mathbf{Q}/\mathbf{U}}, \tag{3.1}$$

where R_S is the responsivity of the detector diode to the source, T_S is the physical temperature of the source, τ is the opacity of the sky, θ is the elevation angle of the QUIET telescope, and $\mathcal{F}_{\mathbf{I}\rightarrow\mathbf{Q}/\mathbf{U}}$ is an offset parameter denoting the $\mathbf{I} \rightarrow \mathbf{Q}/\mathbf{U}$ leakage.

3.4.1.2 Polarization Sensitive Detectors

Taurus A (Tau A, the Crab Nebula), the brightest extra-solar polarized radio source in the frequency bands of the QUIET instrument, provides the absolute polarized calibration for the QUIET instrument. Tau A measurements are referenced to the seven-year WMAP result [33]: for the QUIET Q- (W-) band frequency, the polarization flux density of Tau A is 22.12 ± 0.6 Jy (16.52 ± 0.4 Jy), which yields a total polarization temperature of 5.12 ± 0.14 mK (4.32 ± 0.26 mK). The polarization emission from Tau A comes from a region of $2' \times 2'$, so we model Tau A as a compact point source [34]. Because the temperature in the QUIET beam resulting from the Tau A source polarization flux is relatively small, and the fact that Tau A only rises above the QUIET observing horizon (43° elevation) for $\sim$1-2 hours a day, there is insufficient time to perform an observation of the whole array using a CES.

During Q-band observations, a single Tau A observation is performed each day. The central polarimeter is measured every second day, with one of the non-central polarimeters observed in between central polarimeter measurements (cycling through each polarimeter in the array). During W-band observations, two Tau A observations are performed each day. Every second day, the central polarimeter is measured with one of the two Tau A observations, and the other observations cycle through the non-central polarimeters[5]. Each Tau A observation consists of four to six $\sim$6-minute raster scans, with the deck of the telescope rotated by 45° between each scan. The change in deck angle allows a simulta-

[5]Because the number of polarization detectors in the W-band array (84) is significantly greater than in the Q-band array (17), two Tau A measurements are performed each day during the W-band observing season in order to ensure that a measurement is performed with each non-central polarimeter.

neous fit for the responsivity, leakage and polarization angle of each diode.

We model Tau A as a point source with an amplitude in the map plane described by a two-dimensional Gaussian. For each Tau A observation, a maximum-likelihood fit of the map plane for the azimuth, elevation and deck angles of the telescope is performed with respect to the differenced data time-stream. From this fit, the responsivity, polarization angle, and leakage parameters are obtained from the map $\mathcal{F}_{TauA}$ created from the differenced data time-stream using

$$\mathcal{F}_{TauA} = A\cos 2\left(\gamma - \chi\right) + \mathcal{F}_{\mathbf{I}\rightarrow\mathbf{Q}/\mathbf{U}}, \tag{3.2}$$

where A is the amplitude of the two dimensional Gaussian fit, γ is the deck angle, χ is the polarization angle of Tau A relative to the detector diode, and $\mathcal{F}_{\mathbf{I}\rightarrow\mathbf{Q}/\mathbf{U}}$ is an offset parameter that represents the $\mathbf{I}\rightarrow\mathbf{Q}/\mathbf{U}$ leakage in the Tau A map. The absolute responsivity (of the differenced data time-stream) from each Tau A measurement, R_T, is determined using

$$R_T = \frac{A}{T^{pol}_{TauA}}, \tag{3.3}$$

where T^{pol}_{TauA} is the temperature of the polarization flux of Tau A in the QUIET beam. A Q-band map of Tau A, constructed from observations of the Q1 diode of the central polarimeter, is shown in Figure 3.4. The map is normalized to its maximum value.

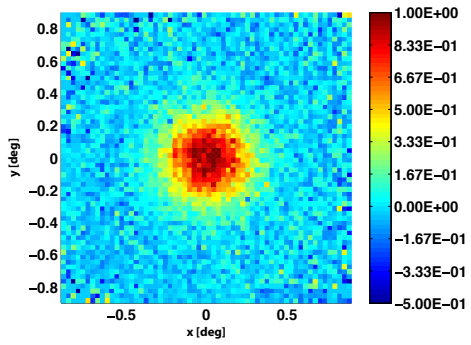

Figure 3.4: Normalized Tau A map using the Q1 diode of the central polarimeter in instrumental coordinates. Tau A map courtesy of Raul Monsalve.

3.4.2 Relative Calibration Sources and Methods

Relative calibration is accomplished using the Moon[6], a polarizing wire-grid and sky-dips. Each relative calibration source, and the calibration parameters obtained from it, is described in this section.

3.4.2.1 Moon

The amplitude of the signal from the Moon is large compared to other calibration sources, making it a desirable relative calibration source in cases where the dynamic range is sufficient to handle bright sources[7]; the polarized emission of the Moon can be detected with a signal-to-noise ratio of greater than 1000 in one second of observation. During Q- and W-band observations, the Moon is observed on an approximately weekly basis. For the most

[6] Although the Moon is principally used as a relative calibrator, its polarization angle measurements are used for absolute calibration during the Q-band observing season.

[7] The Q-band peak polarization temperature of the Moon is about 1K, which is large compared to the $\sim$5 mK polarization temperature of Tau A. The W-band array suffers from compression, and the bright signal from the Moon proves to not be useful for calibration purposes.

part, the Moon is observed using a drift scan (an approximately 45-minute long CES) of 5 degrees in amplitude, scanning all elements in the focal plane[8].

A simple physical model for the Moon is used, assuming it to be a dielectric sphere[9] at a uniform temperature, and this results with a radial polarization pattern [35]. When visualized as Stokes $\mathbf{Q}$ and $\mathbf{U}$ polarizations, the radial pattern on the Moon is represented by a pair of quadrupoles, oriented at an angle of 45° to one another; this can be seen in Figure 3.5 (a). The map $\mathcal{F}_M$ created from the differenced data time-stream is fit using

$$\mathcal{F}_M = R_M \left[\mathbf{Q}\cos\left(2\chi\right) + \mathbf{U}\sin\left(2\chi\right)\right] + \mathcal{F}_{\mathbf{I}\rightarrow\mathbf{Q}/\mathbf{U}} + \mathcal{F}_0, \tag{3.4}$$

where R_M is the amplitude of the responsivity, $\mathbf{Q}$ and $\mathbf{U}$ are the polarized Stokes parameter signals from the Moon, χ is the polarization angle of the Moon relative to the detector diode, $\mathcal{F}_{\mathbf{I}\rightarrow\mathbf{Q}/\mathbf{U}}$ represents the amount of $\mathbf{I}\rightarrow\mathbf{Q}/\mathbf{U}$ leakage into the differenced data time-stream, and $\mathcal{F}_0$ is an offset parameter.

To calibrate the absolute responsivity using Moon measurements, the following effects need to be characterized:

1. Change in temperature of the Moon with its lunar phase;

[8]Occasionally, when the Moon is transiting (there is little elevation change in the Moon's observed elevation during transiting periods), a ∼30 minute raster scan is employed to make a Moon observation over a single row of polarimeters in the array.

[9]The angular diameter of the Moon is slightly larger than the beam size in the QUIET Q and W frequency bands. This model thus overlooks temperature variations across the surface of the Moon and treats any effects such as these as systematic errors.

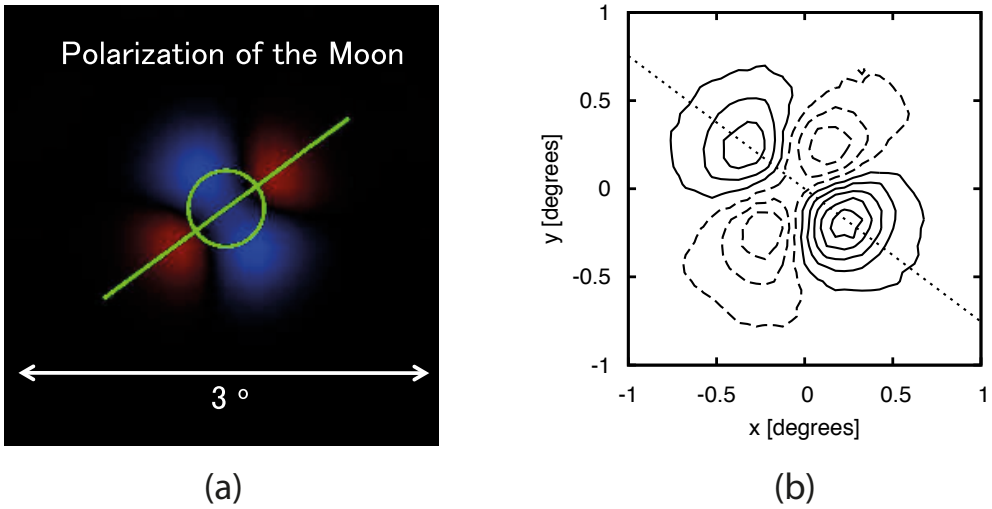

Figure 3.5: (a) Image of Moon polarization using a typical Q-band detector diode. (b) Contour map of the polarization of the Moon (in instrumental coordinates) from a typical Q-band detector diode. The amplitude of the quadrupole polarization in this image is ≈400 mK, with each contour representing 100 mK (negative values are represented by dashed lines). Both figures courtesy of Colin Bischoff.

2. Change in **Q** and **U** polarizations over the face of the Moon;

3. The angular diameter of the the Moon (mean value of 31.6′). Care must be taken as the Q- (W-) band beam size is ∼27.3′ (12.2′).

Since these effects are somewhat complicated to characterize and Tau A provides a more accurate absolute calibration reference, the Moon measurements are used primarily as a relative rather than absolute calibrator to normalize the calibration parameters of a given polarization diode to the reference diode. The Moon measurements are also used to obtain a scaling factor relating the averaged signal to the differenced signal[10]. These factors are

[10]As seen in §2.3.2, the averaged data time-stream is proportional to the gains of inputs A and B by a factor of $\left(g_A^2 + g_B^2\right)$, whereas the differenced data time-stream are proportional by a factor of $(g_A g_B)$. This

obtained by averaging the ratio of the average data time-stream to that of the differenced data time-stream over the duration of the Moon measurement for each detector diode.

However, the Moon is used to obtain the absolute polarization angle of each detector diode: while the magnitude of the polarization changes over the face of the Moon, the $\simeq$400 mK quadrupole polarization temperature pattern observed by the QUIET detectors allows an accurate reference for the polarization angle. This is shown in Figure 3.5 (b).

3.4.2.2 Polarizing Wire-Grid

A polarizing wire-grid is used to determine the calibration parameters of a detector diode relative to the reference diode. The wire-grid consists of a planar array of fine, parallel metallic wires. Wire-grid measurements are performed at the end of the Q- and W- band observing seasons by rotating the wire-grid directly in front of the cryostat window, with the plane of the wire-grid parallel to the plane of the cryostat window. The differenced data time-stream $\mathcal{F}_{WG}$ is fit using

$$\mathcal{F}_{WG} = R_W W_0 \sin\left(2\left(\omega t - \chi\right)\right) + \mathcal{F}_{\mathbf{I}\rightarrow\mathbf{Q}/\mathbf{U}} + \mathcal{F}_0, \tag{3.5}$$

where R_W is the demodulated responsivity of the detector diode, W_0 is the polarization power from the wire-grid, ω is the angular frequency at which the wire-grid is being rotated (2ω is the angular frequency of the polarization rotation, as the wire-grid is 180° symmetric), t is the time, χ is the polarization angle of the wire-grid relative to the de-

results with different responsivity values for the averaged and differenced data time-stream, and ends up being important for the QUIET responsivity models (§4.2).

tector diode, $\mathcal{F}_{\mathbf{I}\rightarrow\mathbf{Q/U}}$ is a parameter that represents the $\mathbf{I} \rightarrow \mathbf{Q}/\mathbf{U}$ leakage, and $\mathcal{F}_0$ is an offset parameter.

3.4.2.3 Skydips

Skydip measurements consist of three nods in elevation (about 6 degrees in amplitude, peak-to-peak, taking 30 seconds per nod), during which the change in brightness temperature of the atmosphere between the two elevations is measured. Skydips are performed before each CES in order to track any changes in responsivity with time. Figure 3.6 shows the telescope elevation and averaged data time-stream as a function of time for a typical Q-band skydip.

The responsivity R_s is obtained for each skydip measurement by fitting the averaged data time-stream $\mathcal{F}_s$ using

$$\mathcal{F}_s = R_s T_B + \mathcal{F}_0, \tag{3.6}$$

where T_B is the brightness temperature of the atmosphere, and $\mathcal{F}_0$ is a an offset parameter. The brightness temperature of the atmosphere is described by

$$T_B = T_{atm}\left(1 - e^{-\frac{\tau_0}{\sin(\theta)}}\right), \tag{3.7}$$

where T_{atm} is the physical temperature of the atmosphere, τ_0 is the zenith opacity of the atmosphere at the site (which is a function of the PWV and ground temperature at the

site), and θ is the elevation angle of the telescope. Given that the averaged data time-stream responsivity (R_s), and the brightness temperature of the sky (T_B) are unknown, a degeneracy between these two values exists. This degeneracy can be broken by determining the brightness temperature of the atmosphere using Jupiter measurements from the total power assembly detectors.

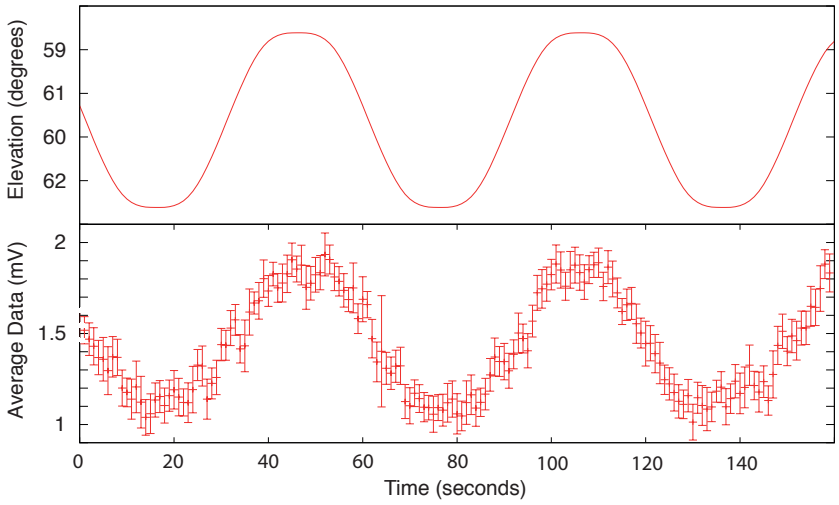

Figure 3.6: Typical Q-band skydip. Example shown is for the Q1 diode of the central horn. As the elevation of the mount oscillates, so does the amplitude of the averaged data time-stream. As the elevation angle increases (zenith is at 90°), the total amount of atmospheric column that the telescope observes decreases.

3.4.3 Summary of Calibration Sources and Methods

A summary of the calibration sources is given in Table 3.3.

Source	Frequency of observation		(Total Power)/	Absolute/
	Q-band	W-band	Polarization	Relative
Tau A	every 1-2 days		polarization	absolute
Jupiter	weekly		total power	absolute
RCW 38	weekly		total power	absolute
Venus	every second week		total power	absolute
Moon	weekly		both	both
Wire-grid	once; end-of-season		both	relative
Skydips	$\sim$ every 1.5 hours		both	relative

Table 3.3: Summary of QUIET calibration sources

Chapter 4

Characterization & Calibration

This chapter outlines the characterization and calibration of the QUIET receivers. Characterization of the instrument (measured at each detector diode) is described in terms of a bandpass, a sensitivity, and a detected noise level and is outlined in §4.1. The responsivity models, polarization angles, $\mathbf{I} \rightarrow \mathbf{Q}/\mathbf{U}$ leakages, and beam profiles for each detector diode (obtained from the calibration source observations (§3.4)) are respectively described in sections §4.2, §4.3, §4.4, and §4.5. The pointing model is discussed in §4.6. Emphasis is placed on the descriptions of the responsivity models as this formed a major part of my thesis work.

4.1 Instrument Characterization

4.1.1 Bandpass Measurements

The bandpass is a measure of the frequency band to which a polarimeter (or instrument) is sensitive. The bandpass of the instrument, measured for each diode, is characterized by a central frequency ν_c and a bandwidth $\Delta\nu$, defined as:

$$\nu_c = \frac{\sum I\nu}{\sum I} \text{ GHz}, \tag{4.1}$$

and

$$\Delta\nu = \frac{[\sum I^2]\,\Delta\nu}{\sum I^2} \text{ GHz}, \tag{4.2}$$

where I is the measured intensity from a detector diode, ν is the frequency, and $\Delta\nu$ is the frequency step used to discretize the frequency band.

For the Q-band receiver, the bandpasses are measured during the testing of the receiver in the laboratory, and these measurements are confirmed with an end-of-season calibration measurement performed during instrument operations. In the laboratory, bandpasses are measured by injecting a polarized carrier-wave signal, swept over the spectrum of a 35-50 GHz signal generator, into the cryostat. As this sweep is performed, the intensity (or voltage) of each detector diode is measured as a function of frequency. This measurement is performed for each polarimeter diode at least eight times, with the module in a variety of different phase-switch states.

At the site, with the Q-band instrument on the QUIET mount, it proved difficult to set up the signal generator in such a way as to not disturb the telescope and cryostat, and the signal generators carrier-wave had to be bounced off of an aluminum plate onto the primary mirror to be directed into the cryostat. The end-of-season measurement of the bandpass frequency ranges is consistent with the measurements recorded in the laboratory, but the associated systematic errors for the measurements are larger, so these are used for confirmation purposes only. Because the biases used to power the active components of the Q-band polarimeters are similar in the laboratory and at the site, the laboratory and site bandpasses are expected to be consistent with one another.

A more sophisticated apparatus for measuring the bandpasses at the site is used for the W-band observing season, alleviating the large systematic errors in their measurement during the Q-band observing season, and site measurements are used to describe the W-band bandpasses. The output from the signal generator is swept between 72-120 GHz, mounted at a position 1-m off-center from the edge of the secondary mirror.

For the Q-band array, the mean central frequency of the detector diodes is $\nu_c = 43.1 \pm 0.4$ GHz, and the mean bandwidth is $\Delta\nu = 7.6 \pm 0.5$ GHz; for the W-band array, the mean central frequency of the detector diodes is $\nu_c = 94.5 \pm 0.8$ GHz, and the mean bandwidth is $\Delta\nu = 10.7 \pm 1.1$ GHz. The stated errors on the central frequency and bandwidth are dominated by the variation in the central frequency and bandwidth between individual polarimeters, and do not reflect the error on the measurement of each individual parame-

ter. A complete set of Q-band bandpass measurements can be seen in Laura Newburgh's Ph.D. thesis [36].

4.1.2 Sensitivity

The sensitivity (or smallest detectable signal) S_i of a QUIET polarimeter i in an integrated observing time τ, is described by the radiometer equation (Kraus, 1986) [37]

$$S_i = \frac{\mathbf{k}\left(\mathbf{T_{rec}} + \mathbf{T_{load}}\right)}{\sqrt{\tau \Delta\nu}}\ \mu\mathrm{K}\sqrt{\mathrm{s}}, \tag{4.3}$$

where $\mathbf{k}$ is constant dependent on the properties of the detector, $\mathbf{T_{rec}}$ is the noise temperature of the receiver (including the noise temperature from the array engine, as well as the window), $\mathbf{T_{load}}$ is the temperature of the source (CMB and atmosphere), and $\Delta\nu$ is the bandwidth of the polarimeter (averaged over the four detector diodes).

The sensitivity of the array, S_{array}, is

$$S_{array} = \sqrt{\frac{\sum_i S_i^2}{N}}\ \mu\mathrm{K}\sqrt{\mathrm{s}}, \tag{4.4}$$

where N is the number of polarimeters.

For the Q-band receiver the sensitivity of the array is 64 $\mu\mathrm{K}\sqrt{\mathrm{s}}$ giving an average polarimeter sensitivity of $\sim$250 $\mu\mathrm{K}\sqrt{\mathrm{s}}$; for the W-band receiver the sensitivity of the array is 85 $\mu\mathrm{K}\sqrt{\mathrm{s}}$ giving an average polarimeter sensitivity of $\sim$750 $\mu\mathrm{K}\sqrt{\mathrm{s}}$.

4.1.3 Noise

The noise detected by a polarimeter diode (including the noise from the detector diode itself, as well as the noise that the detector diode observes from the instrument), is modeled as a function of frequency ν using

$$N(\nu) = \sigma_0 \left[1 + \left(\frac{\nu}{\nu_{knee}}\right)^{\alpha}\right] \quad \frac{\mathrm{V}}{\sqrt{\mathrm{Hz}}}, \tag{4.5}$$

where σ_0 is the white-noise level, ν_{knee} is the knee frequency, and α is the slope of the low frequency spectrum. A sketch of a $1/\nu$ spectrum can be seen in Figure 4.1. For the

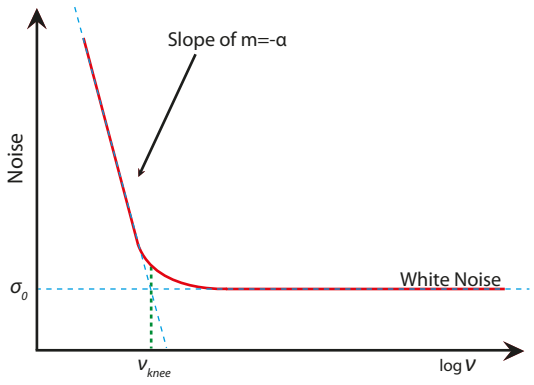

Figure 4.1: Sketch of a $\frac{1}{\nu}$ noise spectrum, created using equation (4.5).

Q-band array, the mean white-noise level and mean knee frequency of the array (including all detector diodes) are $\sigma_0 = (7.4 \pm 2.1) \times 10^{-6}$ V/$\sqrt{\mathrm{Hz}}$, and and $\nu_{knee} = 11.6 \pm 19.2$ mHz. At the time of writing, a full analysis on the W-band noise spectrum is incomplete, so the results are not reported.

4.2 Responsivity Models

4.2.1 Responsivity Calibration of the Q-band Array

For the Q-band array, the variation in the responsivity with time for each QUIET receiver, measured by each detector diode can be modeled primarily in terms of the temperature of the electronics used to bias the QUIET detectors (hereafter : temperature of the electronics), T_{elec}. For each detector diode, whether on a total power assembly detector or a polarization detector, we compute both averaged and demodulated time-ordered data, so we thus compute both averaged and demodulated responsivities. The responsivity (both averaged and demodulated) of the instrument, measured by each detector diode is individually characterized using [38]

$$R\left(T_{elec}\right) = R_0\left(1 + \beta\left(T_{elec} - T_0\right)\right), \tag{4.6}$$

where $R\left(T_{elec}\right)$ is the responsivity measured by a detector diode, R_0 is the magnitude of the responsivity when the temperature of the electronics is T_0, β is the percentage change in responsivity per degree K change in the temperature of the electronics, and T_0 is a reference temperature (universal to all detector diodes) for the temperature of the electronics. Typical values of R_0 and β range from $1 < R_0\ [\mathrm{mV/K}] < 4$, and $0 < \beta\ [\%/\mathrm{K}] < 4$ for a reference temperature of the electronics of $T_0 = 25^\circ$ Celsius. During normal operation,

the responsivity measured by a detector diode can fluctuate by as much as $\sim$5-10% over a period of several hours, and this is accounted for in the analysis.

Averaged and demodulated responsivities depend on the gains g_A and g_B of the LNAs in inputs A and B of the QUIET polarimeter (see §2.3 for details). The averaged responsivity is proportional to a linear combination of g_A^2 and g_B^2 and the demodulated responsivity is proportional to the product $g_A g_B$. While the averaged and demodulated responsivities (R_0, at the reference temperature T_0) of a particular diode will be different, as long as the temperature dependences of the gains (from inputs A and B) are similar in magnitude the averaged and demodulated responsivities will have the same dependence on enclosure temperature, β. Although both averaged and demodulated responsivities are calculated for each detector diode, it is the demodulated responsivities that are used to analyze QUIET data for CMB polarization maps.

4.2.2 Q-Band Responsivity Calibration

A general outline of the responsivity calibration strategy for the Q-band array is given below. Table 3.3 summarizes the calibration sources, the frequency of observation of each source, whether it is used to calibrate total power assembly detectors or polarization detectors, and whether it is used as an absolute or relative calibrator. Analysis of the calibration sources is used to determine a single value of R_0 and β (see equation (4.6)) for the entire season for each detector diode, such that the demodulated responsivity of any detector diode is described as a function of the temperature of the electronics, and can be

calculated as frequently as the sampling of the temperature of the electronics ($\sim$1 Hz). This section will outline how the demodulated responsivity of the total power assembly and polarization detector diodes are modeled for the Q-band array.

4.2.2.1 Total Power Assembly Calibration Overview

- Responsivity measurements for demodulated Jupiter, RCW 38 and Venus observations provide the absolute calibration for the total power assemblies. Jupiter is the brightest unpolarized compact point-source that QUIET observes and is used as the principal calibrator, with RCW 38 and Venus being used as consistency cross-checks. 28 Jupiter measurements, obtained over the course of the Q-band observing season (roughly one every seven days), are used to set the absolute scale of the demodulated responsivity.

- In order to account for short-term fluctuations in the responsivity with respect to the temperature of the electronics, the frequent skydip responsivity measurements are employed, using the averaged data time-stream[1]. Skydip measurements, performed approximately every 1.5 hours (before each CES) over the course of the Q-band observing season, are used to provide short time-scale tracking of the demodulated responsivity.

- In order to compare demodulated responsivities from Jupiter/(RCW 38)/Venus with those from averaged skydip responsivities, an averaged-to-demodulated scaling factor, obtained from measurements of the Moon (§3.4.2.1), is applied to the skydip

[1]The averaged data time-stream is used because the atmosphere is essentially unpolarized and we don't observe a signal corresponding to the skydip in the demodulated data time-stream.

responsivities. Corrective factors, including Ruze scattering and opacity factors, are also applied to the skydip responsivities.

4.2.2.2 Total Power Assembly Responsivity Model

Skydip observations are used to provide a measure of the product of the averaged data time-stream responsivity and of the brightness temperature of the atmosphere at the site (see §3.4.2.3, this product is hereafter denoted by Δ). The Δ for each skydip is fitted for using

$$\Delta = R_s T_B \tag{4.7}$$

where R_s is the measured responsivity of a skydip and T_B is the corresponding brightness temperature of the sky. The Δ values are separated into a responsivity for each diode that varies only with temperature of the electronics, and a brightness temperature of the atmosphere that is a function of the PWV and T_{ground} at the site, hence

$$\Delta = \left(R_0^s + \beta\left(T - T_0\right)\right) T_B\left(\mathrm{PWV}, T_{ground}\right), \tag{4.8}$$

where R_0^s is the responsivity of a skydip at the reference temperature T_0.

Two atmospheric models, AM [39] and ATM [29], are used to provide values of the brightness temperature of the Chajnantor sky as a function of PWV and T_{ground}. Although the AM and ATM models predict different zenith brightness temperatures of the atmosphere for a given PWV and T_{ground}, the changes in brightness temperature estimated

by the two models as a function of PWV and T_{ground} are consistent with one another in the frequency and PWV ranges of interest for the QUIET Q-band array. The variation in the brightness temperature of the atmosphere is described by the ATM model[2], but the absolute scale of the brightness temperature is set by QUIET data. QUIET obtains PWV and T_{ground} measurements from the APEX weather station every minute.

Skydip measurements (§3.4.2.3) are scaled by the following factors in order to compare responsivities from averaged data time-streams to those from demodulated data time-streams:

1. Each skydip responsivity is scaled by the mean ratio of the averaged-to-demodulated data time-streams from the Moon measurements.

2. Ruze scattering [40], a loss effect due to the roughness of the telescope surface, scatters away source radiation. The correction factor employed for this effect does not change significantly over the bandpass of the Q-band detectors, and a corrective factor of 0.97 is applied to each skydip responsivity.

3. Opacity correction due to the optical depth of the atmosphere at the site. The atmosphere scatters away radiation from astronomical sources (Jupiter/(RCW 38)/Venus) along the path from the source to the telescope. Skydips, which measure the temperature of the observed atmospheric column, are unaffected by this scattering. An

[2]Given that the change in brightness temperature as a function of PWV and T_{ground} is consistent between the AM and ATM models for the QUIET frequency and PWV ranges of interest, changing from the ATM model to the AM model results in a difference of $<1\%$ in the values of R_0 and β for each diode. The selection of the ATM model is arbitrary.

opacity correction factor of 0.98, to account for the amount of radiation scattered away by the atmosphere from astronomical source observations, is applied to the skydip responsivities.

Skydip Δ values (equation (4.7)), which are adjusted to account for the above scaling and correction factors are denoted by Δ^*. Using the demodulated Jupiter responsivities (see §3.4.1.1) in conjunction with the Δ^* skydip values, the degeneracy between R_s and T_B is broken by maximizing the joint likelihood of the Jupiter and skydip measurements. The likelihood of the i^{th} Jupiter measurement is calculated using

$$\mathcal{L}_i^J = \frac{1}{\sigma_i\sqrt{2\pi}} e^{-\frac{(m_i-[R_0(1+\beta(T_{elec}-T_0))])^2}{2\sigma_i^2}}, \tag{4.9}$$

where R_0 and β are fitted, and $m_i \pm \sigma_i$ are the Jupiter responsivity measurements R_J with corresponding random errors. Including all of the source measurements,

$$\mathcal{L}^J = \prod_{i=1} \mathcal{L}_i^J. \tag{4.10}$$

The likelihood of the j^{th} skydip measurements is calculated using

$$\mathcal{L}_j^s = \frac{1}{\sigma_j\sqrt{2\pi}} e^{-\frac{\left(m_j-[R_0(1+\beta(T_{elec}-T_0)])\cdot T_B\left(PWV,\ T_{ground}\right)\right)^2}{2\sigma_j^2}}, \tag{4.11}$$

where R_0, β and T_B are fitted, and $m_j \pm \sigma_j$ are the fitted value of Δ^* with corresponding random errors. Including all of the skydip measurements,

$$\mathcal{L}^s = \prod_{j=1} \mathcal{L}^s_j, \tag{4.12}$$

and the joint likelihood of the Jupiter and skydip measurements is defined to be

$$\mathcal{L} = \mathcal{L}^J \mathcal{L}^s. \tag{4.13}$$

By simultaneously maximizing the likelihood of the Jupiter and skydip measurements, the absolute value of the demodulated responsivity R_0 and the percentage change in responsivity as a function of enclosure temperature β are determined for each total power assembly detector diode. These values are then used to calculate the demodulated responsivity of the QUIET Q-band total power assembly detector diodes as a function of the temperature of the electronics using equation (4.6). The brightness temperature of the Chajnantor sky is also determined from the simultaneous likelihood fit[3].

For the total power assembly detector diodes, typical values of R_0 are in the range $0 < R_0$ [mV/K] < 3 with a mean error of $\sim$4% (for each individual measurement), and typical values of β are in the range $1< \beta$ [%/K] < 4 with a mean error of $\sim$30% (for each individual measurement) for a reference temperature of the electronics of $T_0 = 25^\circ$ Celsius.

[3]This brightness temperature is further used to determine the averaged data time-stream skydip responsivities for the polarization detector diodes, using equation (4.7).

4.2.2.3 Polarization Calibration Overview

- Taurus A, the brightest extrasolar polarized radio source that QUIET observes, provides the absolute calibration for the demodulated responsivity of the polarization detectors. 54 central polarimeter Tau A measurements, obtained over the course of the Q-band observing season, are used to set the absolute scale of the demodulated responsivity for the central polarimeter. Each non-central polarimeter observes Tau A at least once over the course of the Q-band observing season.

- Weekly Moon raster scans and a single end-of-the-season polarizing wire-grid measurement (both simultaneously measuring the averaged and demodulated responsivities for the detector diodes of the whole array) provide relative demodulated responsivities for each polarization detector with respect to the reference diode of the Q-band array.

- The absolute calibration of the central polarimeter is accomplished solely using Tau A measurements; absolute calibration of non-central detectors is accomplished using their individual Tau A measurements, and the relative Moon and wire-grid measurements referenced to the mean value of the reference diodes' absolute Tau A measurements.

- In order to determine short-timescale fluctuations in the responsivity with respect to the temperature of the electronics, the more frequent skydip responsivity measurements are employed, using the averaged data time-stream with the conversion factor discussed in §4.2.2.1 to scale the responsivities to that appropriate for the demod-

ulated data time-stream. Using the scaled averaged data time-stream responsivities is reasonable, as we do not expect averaged and demodulated data time-streams to vary differently in time from one another.

4.2.2.4 Polarization Responsivity Model

For the polarization detectors, absolute calibration measurements from Tau A and relative calibration measurements from the Moon/wire-grid (normalized to the Tau A result) are used to set the absolute scale of the demodulated responsivity. Short time-scale tracking of the demodulated responsivity is obtained from skydip measurements.

As described in §4.2.1 the variation in responsivity as a function of the temperature of the electronics is the same for the averaged and demodulated time-streams: the skydip measurements from the averaged data time-stream of the polarization detectors is used to determine the value of β (equation (4.8)).

The amplitude of the demodulated responsivity (R_0) for each polarization detector diode is determined at the reference temperature T_0 (see §4.2.1) using Tau A, Moon and wire-grid data. The value of R_0 for a detector diode on the central polarimeter, with its 54 polarized Tau A measurements, is determined entirely by Tau A observations using

$$R_0 = \frac{\sum_{i=1}^{54} w^i \left(R_T^i + \beta \left(T_{elec} - T_0\right)\right)}{54}, \tag{4.14}$$

where R_T^i is the i^{th} (of 54) Tau A central polarimeter demodulated responsivity measurements of the season, and w^i is the weight of the i^{th} Tau A measurement, given by

$$w^i = \frac{\left(\sigma^i\right)^2}{\sum_i \left(\sigma^i\right)^2}, \tag{4.15}$$

where σ^i is the uncertainty in the fitted amplitude of the Tau A measurement (see §3.4.1.2). For non-central polarimeters, a combination of the small number of individual Tau A observations are used, along with relative Moon and wire-grid measurements to express the magnitude of the demodulated responsivity at the reference temperature T_0, given by

$$R_0 = \frac{\sum_{i=1}^{N_T} \mathbf{R}_T^i + \sum_{j=1}^{N_M} \mathbf{R}_M^j + \mathbf{R}_W}{N_T + N_M + N_W}, \text{ with} \tag{4.16}$$

$$\begin{aligned} \mathbf{R}_T^i &= w^i \left(R_T^i + \beta \left(T_{elec} - T_0\right)\right), \\ \mathbf{R}_M^j &= w^j \left(R_M^{rel\ j} + \beta \left(T_{elec} - T_0\right)\right) R_0^{ref}, \\ \mathbf{R}_W &= w^k \left(R_W^{rel} + \beta \left(T_{elec} - T_0\right)\right) R_0^{ref}, \end{aligned} \tag{4.17}$$

where R_T^i is the i^{th} (of N_T) non-central detector Tau A demodulated responsivity measurement, $R_M^{rel\ j}$ is the j^{th} (of N_M) relative demodulated Moon responsivity measurement of the season, R_W^{rel} is the single ($N_W = 1$) relative demodulated wire-grid measurement, R_0^{ref} is the mean weighted value of the demodulated responsivitiy of the reference diode[4] (from equation (4.14)), and w^i, w^j, and w^k respectively define the weights of the Tau A,

[4] See §3.4.

Moon and wire-grid measurements[5].

Using the acquired values of R_0 (given by equations (4.14) and (4.16)) and β, the demodulated responsivity as a function of the temperature of the electronics for each polarization detector diode is obtained using equation (4.6). For the polarization detector diodes, typical values of R_0 are in the range $1 < R_0\ [\mathrm{mV/K}] < 4$ with a mean error of $\sim$4% (for each individual measurement), and typical values of β are in the range $0 < \beta\ [\%/\mathrm{K}] < 4$ with a mean error of $\sim$25% (for each individual measurement) at the reference temperature of the electronics of $T_0 = 25^\circ$ Celsius.

4.2.2.5 Implementation of the Q-Band Responsivity Model

The salient responsivity parameters are the absolute demodulated responsivity, R_0, and the variation with respect to the temperature of the bias electronics, β. These parameters are used to calibrate the demodulated responsivity of each detector diode approximately every 30 seconds, using the closest temporal temperature measurement of the electronics[6].

The demodulated responsivity of the Q1 detector diode from a typical polarimeter over the course of the entire Q-band season, calculated using the responsivity model, is shown in Figure 4.2 (a). The value of the demodulated responsivity steadily decreases over the Q-band observing season, which coincides with an approximate 1K downward drift in the temperature of the electronics. An example of a demodulated data time-stream divided by

[5] Defined in the same manor as equation (4.15), using the error on the responsivity obtained from the fit.

[6] Although it is possible to calculate the responsivity of each detector diode as frequently as every second, the fluctuations in the electronics temperature are well described by a sampling every 30 seconds.

a constant demodulated responsivity, and the demodulated responsivity calculated every 30 seconds using the responsivity model is shown in Figure 4.2 (b). Ideally, if there is no variation in enclosure temperature, the demodulated signal should be a constant over each CES, with the only variation in the signal coming from white noise.

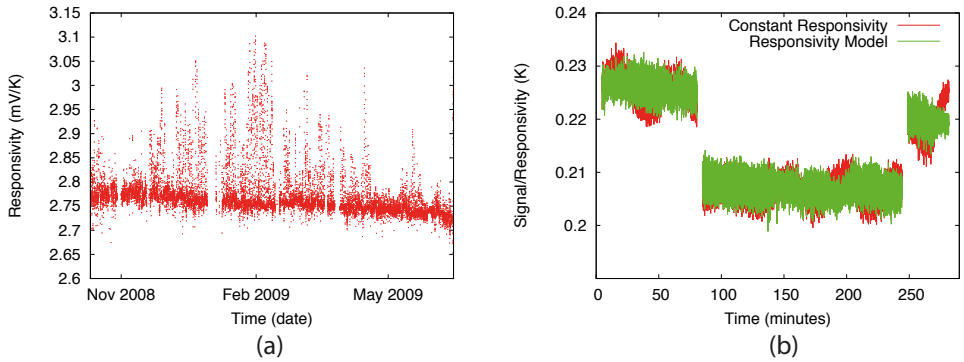

Figure 4.2: (a) Demodulated responsivity over the course of a full season for a typical detector diode using the responsivity model. Larger spikes in the responsivity correspond to brief periods where the temperature of the electronics lost regulation. (b) Demodulated time-ordered data for a typical detector diode for four CES scans, divided by 1) the mean demodulated responsivity of each CES, and 2) the demodulated responsivity from the responsivity model. The demodulated data time-stream shown in (b) is an example of a time-period where significant enclosure temperature variation ($\sim$2 K) is experienced, and is not typical of most of the QUIET data (normally $<$ 1 K variation throughout a CES); it is selected to show the ability of the model to correct the data. The model is not capable of removing all enclosure temperature dependencies, and there is a small amount of hysteresis observed in (b). This occurs because the temperature of the electronics used to bias the detector diodes varies slightly across the electronics boards.

4.2.3 Responsivity Calibration of the W-band Array

Although it was initially assumed that the responsivity models employed for the Q-band receiver would also be used for the W-band receiver, three major differences between the two receivers dictate the need for new models:

1. A revised version of the LNA bias boards produced for the W-band receiver effectively eliminates the dependence of the responsivity on the temperature of the electronics: the temperature of the electronics no longer dominates fluctuations in the responsivity and produces a negligible effect on the averaged and differenced data time-streams.

2. In the W-band frequency range, the optical depth of the atmosphere is much more susceptible to atmospheric changes in PWV; the brightness temperature of the sky increases linearly with PWV, at a rate of $\sim 30\%$ per mm PWV[7]. Variations in the averaged data time-stream (observed with the W-band array) are dominated by fluctuations in the PWV at the site; a fluctuation in PWV from 0 to 3 mm effectively doubles the observed brightness temperature of the atmosphere at the site. Analysis demonstrates that the difference between the amount of PWV directly in the line of sight of the QUIET instrument compared to that measured from the APEX weather station results with a non-systematic scatter in the responsivity measurements of the averaged data time-stream.

[7] See Figure 3.1, which shows the difference in the optical depth over the two frequency bands. In the Q-band frequency range, the optical depth varies very little between 0.25 and 3 mm PWV. In the W-band frequency range, the optical depth approximately doubles when the PWV is changed from 0.25 to 3 mm.

3. The effect of compression (§2.3.4.4) is observed in the W-band demodulated data time-stream for Moon calibration measurements (the Moon has a $\sim$1 K polarization temperature) and in the averaged data time-stream for all calibration measurements, even the skydips (the temperature of the sky, in the QUIET W-band frequency band, ranges between $\sim$5-30 K depending on the amount of PWV in the atmosphere at the site). This makes the demodulated Moon and total power calibration measurements unreliable, and they are therefore not used in the W-band responsivity models. The effect of compression is visible in all detector diodes when the PWV at the site is greater than 5 mm; a data cut is imposed on any data that is taken when the PWV at the site is greater than 3mm.

In order to determine which sources can be used for polarized W-band responsivity calibration, the relative responsivity of each of the Tau A, wire-grid, and skydip measurements with respect to the reference diode (diode Q1 of polarimeter 45) is calculated over the course of the observing season. These relative responsivity values are then compared to one another, to determine consistency. Figure 4.3 (a), (b) and (c) respectively show the relation between relative skydip and relative Tau A responsivities, relative skydip and relative wire-grid responsivities, relative Tau A and relative wire-grid responsivities. If the skydip, Tau A, and wire-grid data are consistent with one another, plotting the relative responsivity of one calibrator against another should result with a linear relation (with slope of unity). From this analysis it is clear that the skydips (averaged data time-stream) are affected by compression, given that the larger relative responsivities result in larger deviations from

a slope of unity. That is, the skydips are unreliable as a W-band calibration source.

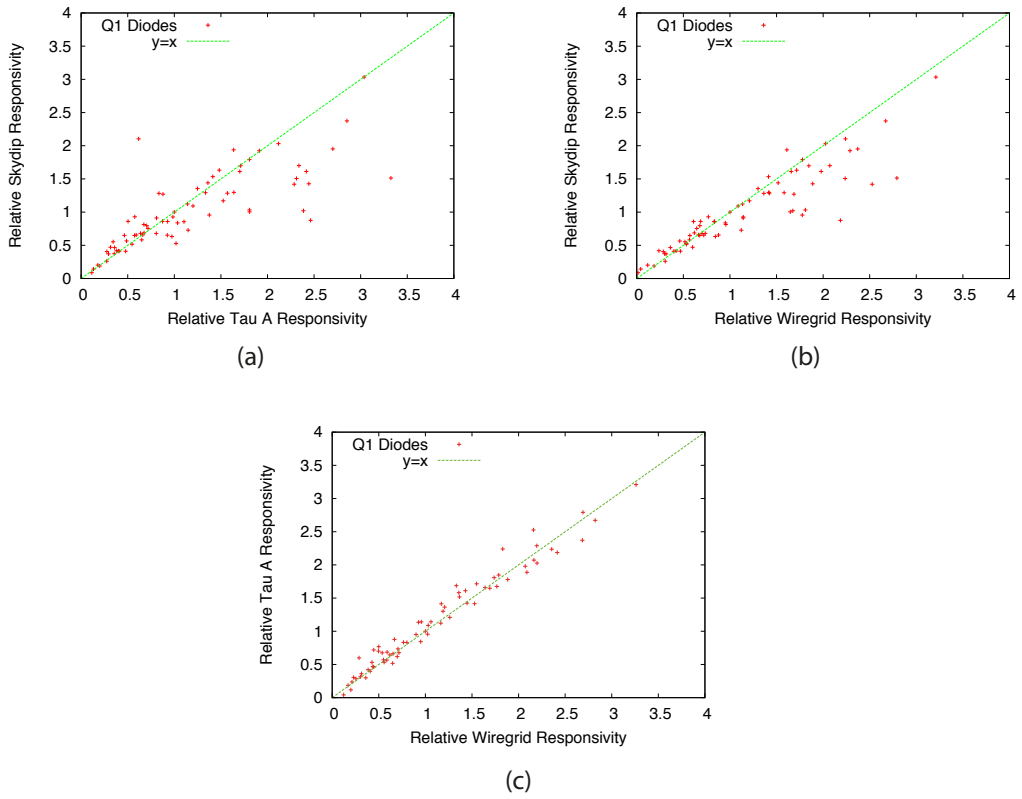

Figure 4.3: (a) Relative responsivity of Tau A measurements vs. those of skydips; (b) Relative responsivity of wire-grid measurements vs. those of skydips; (c) Relative responsivity of wire-grid measurements vs. those of Tau A. All plots also show a linear function with slope of unity.

Given that fluctuations in the temperature of the electronics produce negligible effects on the responsivities of the QUIET W-band detector diodes, and that fluctuations in PWV at the site produce a non-systematic scatter in the responsivities of the QUIET W-band detector diodes, it is not important to track short time-scale variations of the W-band responsivities (unlike the responsivity of the Q-band detector diodes, which can vary $\sim$5-10% over a few hours). For this reason, the responsivities of the (total power assembly)/polarization W-band detector diodes are modeled simply using the (Jupiter/RCW 38/Venus)/((Taurus A)/wire-grid) observations.

4.2.4 W-Band Responsivity Calibration

A general outline of the responsivity calibration strategy for the W-band array is given below. Table 4.1 summarizes the W-band calibration sources used to obtain the W-band responsivity models, the frequency of observation of each source with the central and non-central detectors, whether it is used to calibrate total power assembly detectors diodes or polarization detector diodes, and whether it is used as an absolute or relative calibrator.

4.2.4.1 Total Power Assembly Calibration

Similar to the Q-band responsivity calibration, responsivity measurements for demodulated Jupiter, RCW 38 and Venus observations provide the absolute calibration for the total power assembly detector diodes. Jupiter is used as the principal calibrator, with

Source	Frequency of Observation	Central (Non-Central) {TPA} Horn Measurements	(TP)/ Pol.	Abs./ Rel.	Used in W-band Responsivity Model
Jupiter	weekly	1 (27) {135}	TP	abs.	Yes
RCW 38	weekly	0 (0) {121}	TP	abs.	Yes
Venus	weekly	0 (0) {14}	TP	abs.	Yes
Tau A	daily	119 (1-6) {0}	pol	abs.	Yes
Wire-grid	once; end-of-season	1 (1) {1}	both	rel.	Yes
Moon	weekly	72 (72) {72}	both	rel.	no (compression)
Skydips	$\sim$ every 1.5 hours	6625 (6625) {6625}	both	rel.	no (compression)

Table 4.1: Summary of W-band Responsivity Model Calibration Sources. For each source, the frequency of observation, the number of observations performed with the central (non-central) {total power assembly} detectors, whether the source is used for total power or polarization calibration, whether the source is used as a relative or absolute calibrator, and whether or not the source is able to be used in the W-band responsivity models are given. At the time of writing, analysis of the Jupiter/(RCW 38)/Venus measurements is incomplete, and the number of useful measurements is subject to change.

RCW 38 and Venus being used as consistency cross-checks. 135 Jupiter measurements, obtained over the course of the W-band observing season (roughly one every seven days), are used to set the absolute scale of the demodulated responsivity. Due to compression in the response to the total power calibration sources, no variations in the responsivity are tracked on timescales shorter than the frequency of Jupiter observations ($\sim$1 week). Fixes to the revised LNA bias card effectively eliminate any dependence that the temperature of the electronics has on the responsivity of the QUIET W-band detector diodes, and hence $\beta = 0$ for all detector diodes. Typical values of the total power assembly detector diode demodulated responsivities range from 0.5–5 $\frac{\mathrm{mV}}{\mathrm{K}}$ with a mean statistical error (for each individual detector diode) of $\sim$25%.

4.2.4.2 Polarization Calibration Overview

- The W-band polarized responsivity model uses absolute demodulated Tau A and relative demodulated wire-grid measurements (normalized to Tau A). No variations in the polarization detector responsivity calibration are tracked on timescales shorter than the Tau A observation frequency ($\sim$every second day). The demodulated responsivity profile of the central Q1 detector diode is scaled to non-central detector diodes, using Tau A and wire-grid measurements. At the time of writing, W-band analysis is still underway and the model described is preliminary.

4.2.4.3 Polarization Responsivity Model

The profiles of the demodulated responsivity for the four central detector diodes over the course of the W-band observing season are shown in Figure 4.4. A sinusoidal oscillation, with a period of one year, is observed for each of the four diodes. The Tau A responsivities are fit using the following functions, in order to determine which function best described the observed trend in the data:

- $R_1(t) = A_0$,
- $R_2(t) = A_0 + A_1 t$,
- $R_3(t) = A_0 + A_1 t + A_2 \sin(A_3 t + A_4)$,

where t is the time and A_i are parameters for the fits. The reduced χ^2 of function $R_3(t)$ is a factor of $\frac{1}{2}-\frac{1}{3}$ smaller than for functions $R_1(t)$ or $R_2(t)$, and $R_3(t)$ is used to model

the demodulated responsivity profile of the W-band detector diodes. ($R_3\,(t)$ will hereafter be referred to as $R_{fit}\,(t)$). Since the observed oscillation is on the time-scale of one year, the $R_{fit}\,(t)$ function is slowly varying. For the purposes of capturing this long-timescale variation, the Tau A measurements made roughly every 48 hours are sufficient.

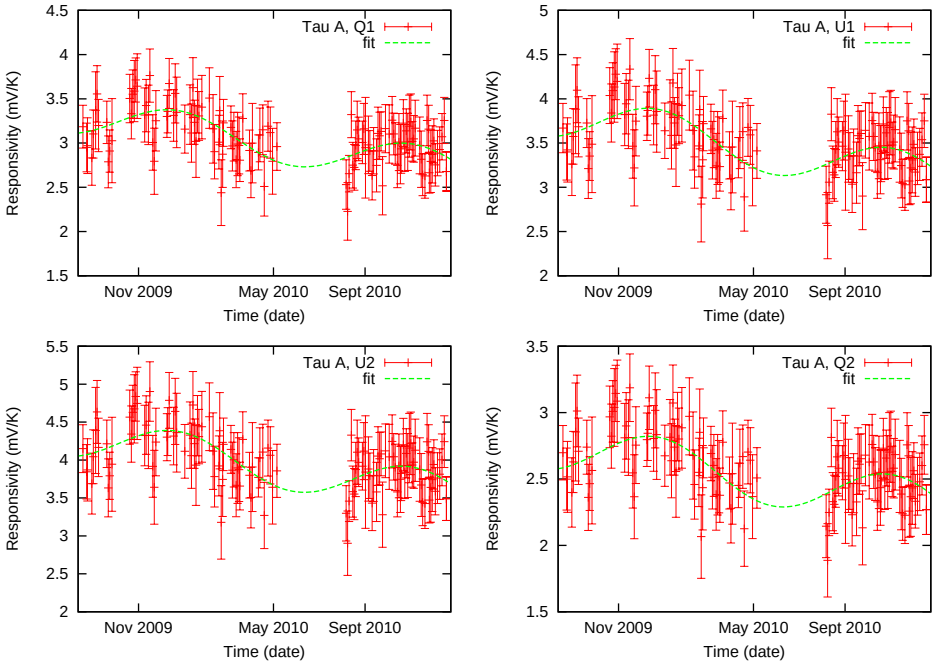

Figure 4.4: Demodulated responsivities as a function of time for the central polarimeters detector diodes. There is a noticeable gap in the Tau A measurements over the course of the W-band season (May 5 2010 – August 6 2010), due to Tau A falling below the observing horizon of the QUIET instrument. The best fit to the data, using a linear-sinusoidal fit, is also shown.

For the central polarimeter, there are 119 Tau A measurements and one wire-grid measurement. The set of Tau A and wire-grid measurements for the Q1 diode of the central

detector are modeled using the linear-sinusoidal fit to the data, $R_{fit}(t)$. For each non-central polarimeter, there are between one and six Tau A measurements and one wire-grid measurement.

The demodulated responsivity profile of a non-central detector diode Y (with N Tau A and wire-grid measurements) is normalized to the demodulated responsivity profile of the reference diode of the array. The i^{th} demodulated responsivity measurement for a non-central diode Y at time t_i is

$$Y_i(t_i) \pm \sigma_{Y_i}(t_i). \tag{4.18}$$

For each responsivity measurement Y_i, a scaling factor to $R_{fit}(t)$ is determined using

$$S_i = \frac{R_{fit}(t_i)}{Y_i(t_i)}. \tag{4.19}$$

After the scaling factors S_i for each of the N demodulated responsivity measurements Y_i are determined, the overall scaling factor S is determined using

$$S = \sum_i w_i S_i(t_i), \tag{4.20}$$

where the weight of each measurement is determined using a standard least-squares error formula given by

$$w_i = \frac{(\sigma_{Y_i}(t_i))^2}{\sum_j \left(\sigma_{Y_j}(t_j)\right)^2}. \tag{4.21}$$

Once a scaling factor S is determined for a non-central detector diode Y_i, the Q1 profile of the central detector diode is scaled to the non-central detector diode. That is, for a non-central diode Y with scaling factor S,

$$R_Y(t) = SR_{fit}(t_i). \tag{4.22}$$

4.3 Polarization Angles

In §3.4, the methods by which the polarization angle is extracted from the Moon, Tau A, and the wire-grid measurements are described. For the Q-band array the polarization angle of each detector diode is obtained from Moon measurements. The less precise Tau A and wire-grid polarization angle measurements are used as cross-checks (for each case, the differences between the polarization angles determined from the cross-check sources and the Moon are described by an approximate 3% mean standard deviation). A histogram of the polarization angles for the Q1, U1, U2, and Q2 diodes is shown in Figure 4.5. At the time of writing, the polarization angle calibration for the W-band array is incomplete and therefore omitted.

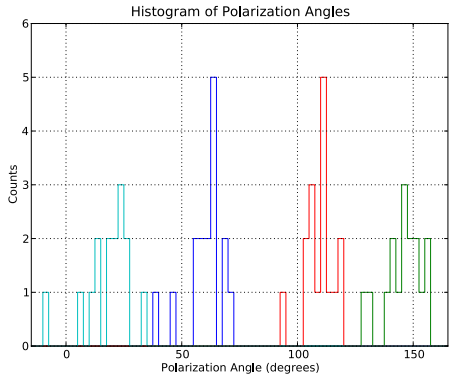

Figure 4.5: Histogram of detector diode polarization angles. Q1 (Q2) diodes are shown in blue (green), and U1 (U2) diodes are shown in red (light blue). The mean standard deviation of the polarization angles is $\sim 0.3°$, determined by the average error of each polarization angle. The bin size for the shown histograms is 2.5°.

4.4 $\mathbf{I} \rightarrow \mathbf{Q}/\mathbf{U}$ Leakages

Due to instrumental imperfections, some of the Stokes parameter $\mathbf{I}$ is transformed into Stokes $\mathbf{Q}/\mathbf{U}$ polarizations; the addition of these Stokes $\mathbf{Q}/\mathbf{U}$ polarizations is referred to as $\mathbf{I} \rightarrow \mathbf{Q}/\mathbf{U}$ leakage. The two main sources of $\mathbf{I} \rightarrow \mathbf{Q}/\mathbf{U}$ leakage come from differential loss and crosstalk[8]. Differential loss occurs if the septum polarizer has different transmission amplitudes for its two output orthogonal linear polarizations. Crosstalk occurs if the two output ports of the septum polarizer are imperfectly isolated; this results with a fraction of the signal being reflected off of the first stage amplifier in the polarimeter and back out to the septum polarizers output port. While most of the reflected radiation from crosstalk is sent back out of the cryostat, a portion of it couples to the polarimeters other

[8]Phase-switch imbalance would also be a major source of $\mathbf{I} \rightarrow \mathbf{Q}/\mathbf{U}$ leakage, but it is effectively eliminated by the process of double-demodulation (§2.3.2).

input port.

For the Q-band array, the differential loss effect is the dominant source of $\mathbf{I} \rightarrow \mathbf{Q}/\mathbf{U}$ leakage; crosstalk and other instrument imperfections contribute to second order. $\mathbf{I} \rightarrow \mathbf{Q}/\mathbf{U}$ leakage is extracted from Moon and Tau A observations (see §3.4). For the Q-band array, leakage values are of the order of 1.0% (0.2%) for the Q (U) detector diodes (the fact that the Q detector diodes have larger leakage values than the U detector diodes is predicted from the properties of the Q-band septum polarizer OMTs). This effect is not corrected for, but is accounted for in our systematic errors. Figures 4.6 (a) and (b) respectively show histograms of $\mathbf{I} \rightarrow \mathbf{Q}/\mathbf{U}$ leakages for the Q and U detector diodes. At the time of writing, the $\mathbf{I} \rightarrow \mathbf{Q}/\mathbf{U}$ leakage calibration for the W-band array is incomplete and therefore omitted.

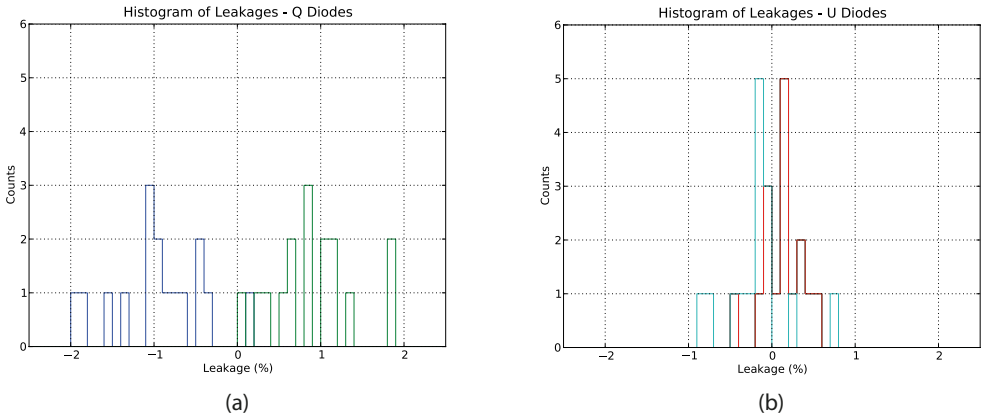

Figure 4.6: (a) Histogram of Q-diode leakages for the Q-band array. Q1 (Q2) diodes are shown in blue (green). (b) Histogram of U-diode leakages for the Q-band array. U1 (U2) diodes are shown in red (light blue). For each pair of detector diodes (Q1/Q2, or U1/U2) the signal for one of the Q/U diodes has a positive amplitude and the signal for the other is negative; this is why the Q1/Q2 (or U1/U2) diode leakages seen in (a) (or (b)) have opposite signs. The orientation of the polarization signal from the differential loss is closely aligned with the instrumental frame of the Q diodes, and the resulting leakages are much larger for the Q diodes than the U diodes. The bin size for these histograms is 0.1%.

4.5 Beam Profiles and Window Functions

For the Q-band array, the beams of the total power assembly and polarization detectors are respectively modeled using two-dimensional elliptical Gaussians to the Jupiter and Tau A measurements. Using these measurements, the beams are best defined for the central detector (Tau A measurements are performed every few days) and the total power assembly detectors (Jupiter measurements are performed every week); the non-central polarization detectors are measured less frequently and are less precisely known. A two-dimensional elliptic Gaussian is used to model the elongation and rotation angle of the beam; mea-

surements yield an average elongation of 1.4%$\pm$0.6%, with the error coming from the variance in elongation between polarimeters (the dominant portion) and statistical error. From the analysis, the average full-width at half-maximum (FWHM) of the beams for the QUIET Q-band detectors is determined to be $27'.3 \pm 0'.1$ (the error quoted here is statistical error) for the central polarimeter and total power assembly detectors. Because the non-central (not including total power assembly detectors) polarimeters are observed less frequently, the associated error on their FWHM is $\pm\ 1'.5$.

The window functions, which describe the effect of the finite resolution of the instrument on the power spectra, are calculated using the central polarimeter and total power assembly detectors. The beam profile and window function for the central polarimeter are shown in Figure 4.7. At the time of writing, the beam calibration for the W-band array is incomplete and therefore omitted.

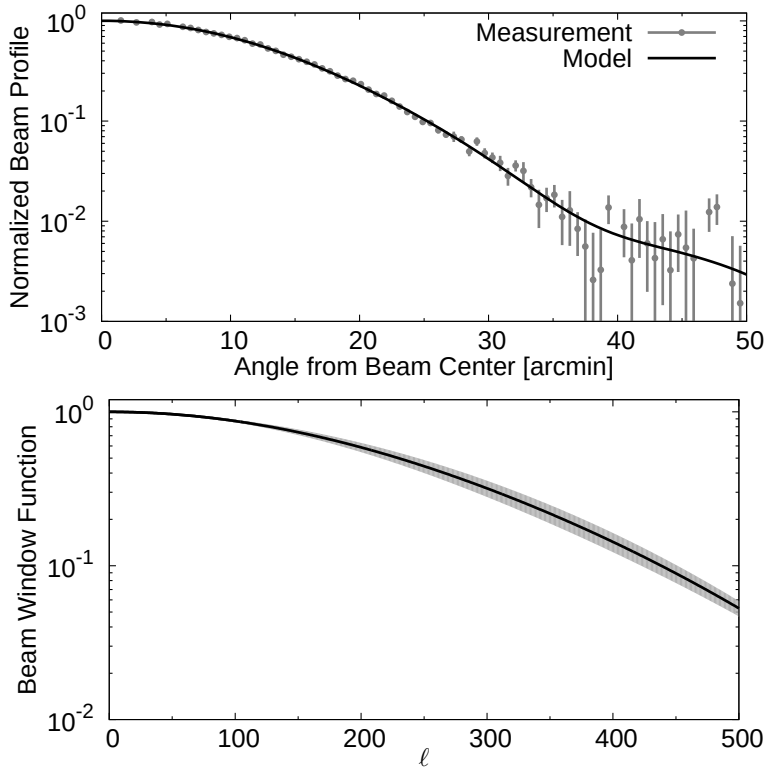

Figure 4.7: Top panel: Polarization beam profile created from Tau A observations using the central polarimeter. The data are over-plotted with the expansion in Gauss-Hermite polynomials. Bottom panel: Beam window function for the central polarimeter. One-sigma errors are shown by the gray band. Both figures courtesy of Immanuel Buder.

4.6 Pointing Solution

The location of any source is defined by its geocentric apparent right ascension and declination coordinates. The pointing model is used to accomplish the conversion from these coordinates (at the altitude and longitude of the QUIET site) to the instrument azimuth, elevation and deck angle; this requires knowledge of the geodetic latitude and longitude of the site, the distance from the center of the earth, and the radial distance from the rotation axis of the earth.

4.6.1 Determining the Apparent Positions of Celestial Sources

In order to implement a pointing model, a data set of apparent (observed) and ephemeris (actual) positions is amassed from the Q-band observing season measurements. The data set includes Jupiter, Venus, and Galactic field G-2 (see Figure 3.3). For each source observation, a flat-sky $1^\circ \times 1^\circ$ mini-map is created by binning the filtered[9] averaged data time-stream in to $2' \times 2'$ pixels, centered around the expected position of the source. Using this mini-map, the apparent position of each individual measurement is estimated by finding the brightest pixel; the uncertainty in this procedure is estimated to be $3'$. This data is used to determine the pointing solution for the telescope.

[9]The averaged data time-stream is filtered by subtracting off constant offsets from every four-second time segment.

4.6.2 Pointing Model Parameters

In order to build a model for the pointing of the telescope, the effects of atmospheric refraction, flexure, azimuth and elevation axis tilts, and collimation offsets need to be accounted for. The above effects are accounted for using a seven-parameter pointing model (with exception to atmospheric refraction, which is corrected for using data from the QUIET weather station) which are given in the description of the various effects below:

- *Atmospheric Refraction* – Refraction of light in the atmosphere causes sources to appear slightly higher than their true elevation. This effect is shown in Figure 4.8 (a). Using the relative humidity and ground temperature at the site from the QUIET weather station, the conditions in the higher atmosphere at the time of observation are modeled and an elevation offset is estimated. Typical elevation offsets due to atmospheric refraction are of the order of $0.5'$.

- *Flexure* – A traditional radio telescope usually consists of a single-point elevation axis support and a large counter-weight. The force of gravity causes a sag on either side of the axis and results in an elevation that is lower than requested. The QUIET mount is supported at two points (the azimuth screw and the deck hinge, Figure 4.8 (b)), thus eliminating most of the sag experienced by a single-point elevation axis support system. Nevertheless, a small amount of flexure in the deck platform and azimuth bearing remains; this is modeled using a flexure parameter k_f.

- *Azimuth and Elevation Axis Tilts, Deck Offset* – The azimuth axis of the telescope

is not perfectly aligned with the geodetic longitude and latitude of the GPS timing board. This occurs for two reasons: the azimuth axis is not exactly aligned with local gravity; irregularities in the azimuth bearing of the mount and a varying centre of gravity of the instrument on the deck platform. This results with an azimuth axis tilt described by ψ and Θ, parameters which define its orientation and magnitude. The elevation axis is supposed to lie in the plane of the azimuth "ring". In practice, there is a small angle between the azimuth axis "ring" and the elevation axis and this is accounted for with an elevation axis tilt parameter Θ_E. The QUIET mount uses the defined reference ("zero") deck value from the CBI experiment, and a deck offset parameter ΔD is used to define a desired reference ("zero") deck value for the QUIET experiment to that of the CBI experiment.

- *Collimation Errors* – If the optical axes of the telescope and receiver are perfectly aligned, the center of the source remains in the same location as the deck rotates (for the center of the receiver). In practice, the center of the source traces a circle as the deck is rotated, and this offset is referred to as a collimation offset. Two collimation offset correction parameters are required: ϕ_C and Θ_C, parameters that define the orientation and magnitude of the collimation offset.

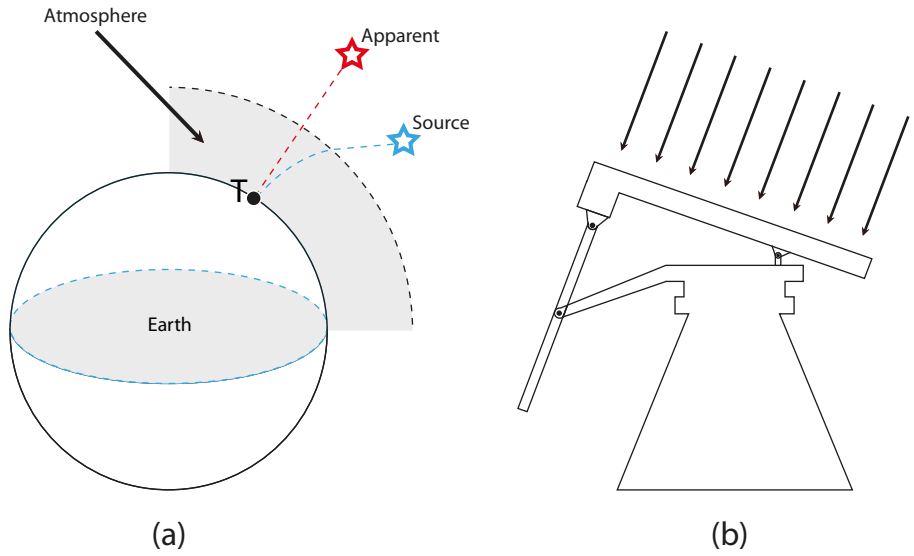

Figure 4.8: (a) Illustration of atmospheric refraction (the proportions in this figure are exaggerated). The telescope, at point T, observes the source at its apparent, rather than true elevation. (b) Illustration of how the two-point mount support helps reduce the amount of flexure on the telescope.

4.6.3 Estimation of Mount Model Parameters

The full set of mount model parameters (α) is estimated using a standard Markov Chain Monte Carlo (MCMC) method using the likelihood equation

$$-2\mathcal{L}(\alpha) \propto \sum_{i,j} \Delta r_i(\alpha) N_{ij}^{-1} \Delta r_j(\alpha), \tag{4.23}$$

where $\Delta r(\alpha)$ is the pointing error for observation i when using α as a mount model, and N is the corresponding covariance matrix. Using this likelihood equation, 10 independent

MCMC chains sample the posterior surface, without using any priors. Each MCMC chain is run for 20000 samples, and the Gelman-Rubin statistic is computed for each chain to check that conversion has taken place. The final parameter estimate is taken as the sample with the highest likelihood. Table 4.2 gives the resulting mount model parameters from the likelihood fit for the Q-band observing season[10]. Using the aforementioned mount model parameters, the error in the pointing is found to have an RMS error of $3.5'$ and a bias of $1'$.

Mount Model Parameter	Value (degrees)
ΔD	0.3584964 $\pm$ $\sim$0.3
k_f	0.07981 $\pm$ 0.010599
(Θ, ψ)	(0.12156, 258.4085) $\pm$ 0.007658
Θ_E	0.02868 $\pm$ 0.00624655
(Θ_C, ψ_C)	(0.28259, 335.6259) $\pm$ 0.019551

Table 4.2: Estimated Mount Model Parameters

[10]The ΔD value evolved over the course of the season, and the quoted value represents the mean value over the course of the season. The associated error on ΔD at any specific time during the season is $\sim$0.3°. The azimuth tilt and radio collimation parameters ((Θ, ψ) and (Θ_C, ψ_C)) contain both an orientation and magnitude, and the RMS error quoted is for the pair of parameters.

Chapter 5

Data Reduction, Analysis & Systematic Errors

This chapter describes the QUIET data reduction (§5.1) and analysis procedure (§5.2), and quantifies the systematic errors of the QUIET experiment (§5.3).

5.1 Data Reduction

Data reduction is divided into three components: a pre-processing of the data (§5.1.1); various cuts implemented to remove contaminated data (§5.1.2), and a post-process filtering of the data (§5.1.3).

5.1.1 Pre-Processing Data

When 800 kHz samples are accumulated by the FPGA (§2.4.7), the 14% of data nearest to the phase-switch transition are not included due to signal instability during this transition; this is shown in Figure 5.1. Furthermore, a small non-linearity in the analog-to-digital conversion process caused by the ADC electronics boards, obfuscates some of the data: the transfer function (giving the output bit value for each input voltage received) contains step-like discontinuities, and these observed non-linearities (of magnitude 1-20 bits) occur every 1024 bits in the ADC. This "glitching" affects approximately 14% of the data, though the effect is able to be corrected for using a pre-processing algorithm: if elements from the true differenced data time-stream are denoted as x_i, and the values from the differenced data time-stream calculated at an ADC "glitch" are denoted by y_i, then

$$y_i \equiv f(x_i) = x_i + \Delta f(x_i), \tag{5.1}$$

where $f(x_i)$ is a function describing the non-linearity of the ADC glitch, and $\Delta f(x_i)$ is a small correction term. A schematic representing the non-linearity seen in equation (5.1) is shown in Figure 5.2; an example of a differenced data time-stream with a glitch, and the algorithm-corrected differenced data time-stream is shown in Figure 5.3. It can be seen in Figure 5.3 that the "glitching" algorithm does not perfectly correct the data. The possible residual from ADC "glitching" results in an effect similar to $\mathbf{I} \rightarrow \mathbf{Q}/\mathbf{U}$ leakage; this contributes at most an additional 3% effect on the $\mathbf{I} \rightarrow \mathbf{Q}/\mathbf{U}$ leakage, and this is taken into account in the systematic errors (§5.3).

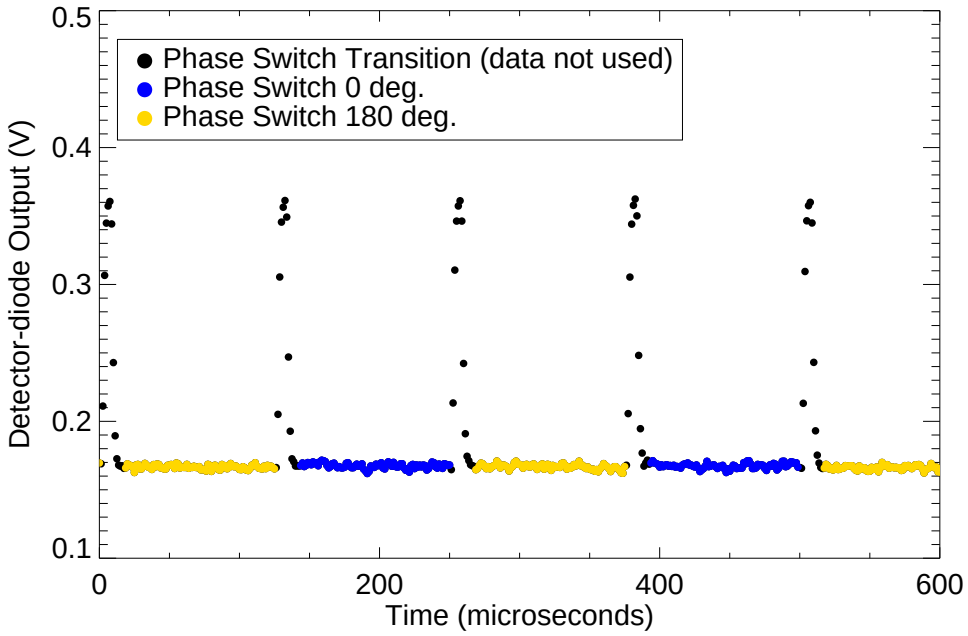

Figure 5.1: Output (Volts) of a QUIET detector diode. When a phase-switch is toggled between its two states (0°, 180°), it produces an unwanted spike in the detector diode data; this data, marked by black points in this figure, makes up $\sim$14% of the total data collected and is removed from the data set. Figure courtesy of Immanuel Buder.

Static data cuts, also part of the pre-processing procedure, are explained in detail in §5.1.2.

5.1.2 Data Cuts

Several data cuts are employed to remove contaminated data from the Q-band observing season data; these include: static cuts, those which are tied to specific events known to contain sources of contamination; duration cuts, where the duration of the CMB observation is insufficient to obtain noise characteristics of the detector diodes (for observations

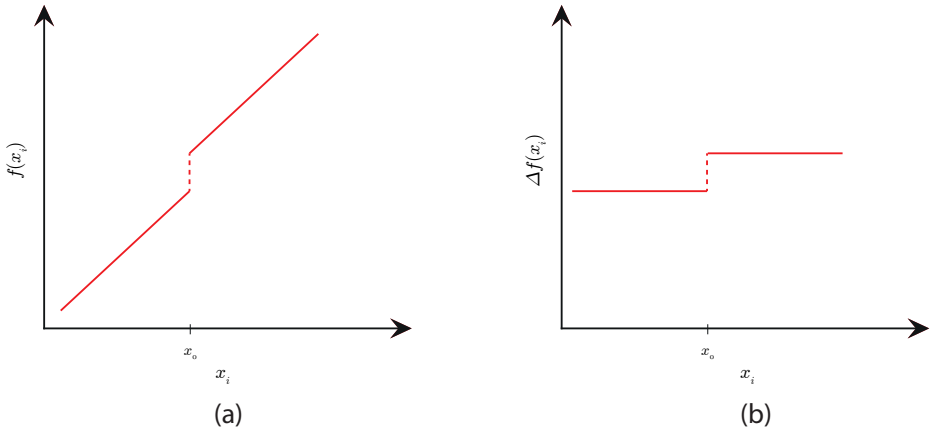

Figure 5.2: A schematic representing the non-linearity caused by the ADC electronics boards. (a) shows the glitch in terms of the "true" ($f(x_i)$) and measured (x_i) values. (b) shows the adjustment term required to correct the differenced data time-stream.

of less than 1000 s in length); weather cuts, where the effect of poor weather is observed in the differenced data time-stream; phase switch cuts, periods of time when electrical shorts of the phase switch PIB board (§2.4.3) result with a subset of detectors malfunctioning; "glitch" cuts, where the pre-processing "glitching" algorithm is insufficient in correcting the differenced data time-stream; sidelobe cuts, where spurious radiation is suspected to have leaked into the sidelobes of the QUIET beam; FFT cuts, where the χ^2 of the model fit to the FFT of the CES surpasses a certain threshold; and min-max cuts, where large "spike" outliers are found in the differenced data time-stream. All of the aforementioned cuts are performed at the CES level. For a given CES, if a polarimeter diode A is flagged with one (or more) of the aforementioned contaminations, the entire CES for the polarimeter diode A is cut.

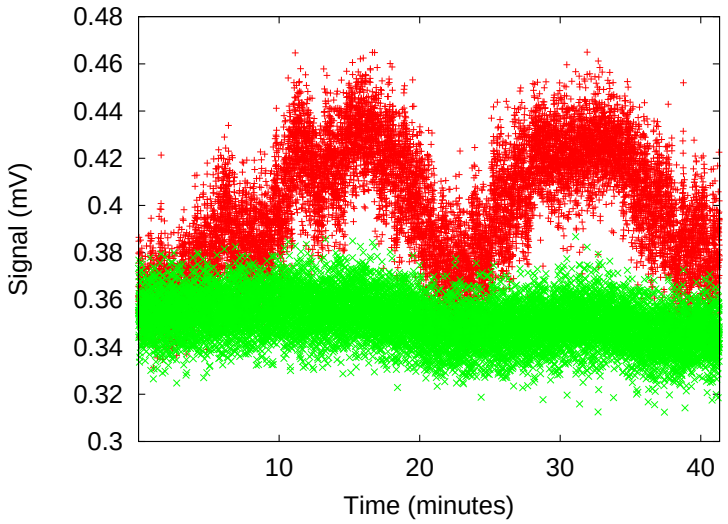

Figure 5.3: Differenced data time-stream affected by a non-linear ADC "glitch" (red), and the same differenced data time-stream that has been corrected by the ADC "glitching" algorithm. The "glitching" algorithm is unable to completely remove the erratic effects from the "glitch"; this is taken into account for in the systematic errors.

A CMB field observation consists between one and several CES scans; a CES Y of a CMB field observation X is denoted as CMB observation $X.Y$. A *CES-diode* is the name give to the data of a CES from a particular detector diode. A summary of the data cuts, including the percentage cut by each process, is given in §5.1.2.7.

5.1.2.1 Static Cuts

Several static cuts are implemented over the duration of the Q-band observing season. The majority of these cuts come from:

1. An imbalance in the biases sent to the phase-switches during the first 125 CMB observations;

2. A poor noise spectrum in the Q1 diode of RQ04, and a detector malfunction in polarimeter RQ16 (all diodes are affected) rendering them useless for the season;

3. Periods of time when tests are performed to determine the source of the "glitching" in the data: a switching of two preamplifier cables for a period of two days (CMB observations 329-342); and a switching of the short, rigid and grounded AIB cables with the prototype AIB cables used in laboratory testing (CMB observations 563-596). Data is cut during these two time periods due to a lack of calibration data taken during the changed state of the experiment;

4. A period of time when the ADC card that manages the signals from MAB 2 blew a fuse, rendering the data acquired from polarimeters on MAB 2 useless (CMB observations 632.5 and 633-636);

5. Mechanical failures associated with the operation of the deck, affecting CMB observations 937, 951.1, and 953-955.

A summary of the static data cuts over the duration of the Q-band observing season (some of which overlap with one another) are given in Table 5.1

5.1.2.2 Weather Cuts

Occasionally, the quality of observations at the site is significantly degraded due to poor weather conditions; this occurs more frequently during the hotter and wetter summer

Static cut	Polarimeters affected	CMB observations cut	% of data cut
Phase-switch imbalance	all	1-125	2.4
Malfunctioning detector diodes	RQ16, Q1 of RQ04	all	9.2
Preamplifier/AIB cables swapped	all	329-341	
ADC fuse blown	RQ07-09, RQ12-13, RQ16	632.5, 633-636	3.6
Mechanical failures	all	563-596	
Total			14.6

Table 5.1: Summary of Static Data Cuts

months. A weather cut is imposed on the data at two timescales, 10 s and 30 s: the 10 s timescale is selected due to the similarity in time scale with that of the azimuth scans; the 30 s time scale is selected due to the characteristics of typical weather patterns at the site. The method by which these cuts are imposed (for each time scale) is the following:

1. For each polarimeter detector diode, the differenced data time-stream is binned into blocks of data of length of the time scale, and the standard deviation of each data block, denoted by σ, is computed;

2. A CES, lasting from $\sim$40-90 minutes, has a calculated standard deviation for each of the 240-540 (80-180) binned data blocks for the 10s (30s) time scale. For each polarimeter diode and CES, the standard deviation of these standard deviations is computed, which is denoted by Σ_{CES}, for each diode;

3. For each polarimeter diode, the mean (μ_{CES}) and standard deviation (σ_{CES}) of the Σ_{CES} values are calculated;

4. If, for a single CES, more than 70% of the Σ_{CES} values are outside of $5\sigma_{CES}$ of μ_{CES}, the CES is cut.

Since it is required that 70% of CES-diodes must be flagged in order for the weather cut to be implemented, this avoids falsely implementing the weather cut due to other effects acting on small sub-sections of the array. Figure 5.4 shows a histogram of the Σ_{CES} values for each of the detector diodes on polarimeter RQ09 for CMB field CMB-1; these results are typical for the Q-band receiver.

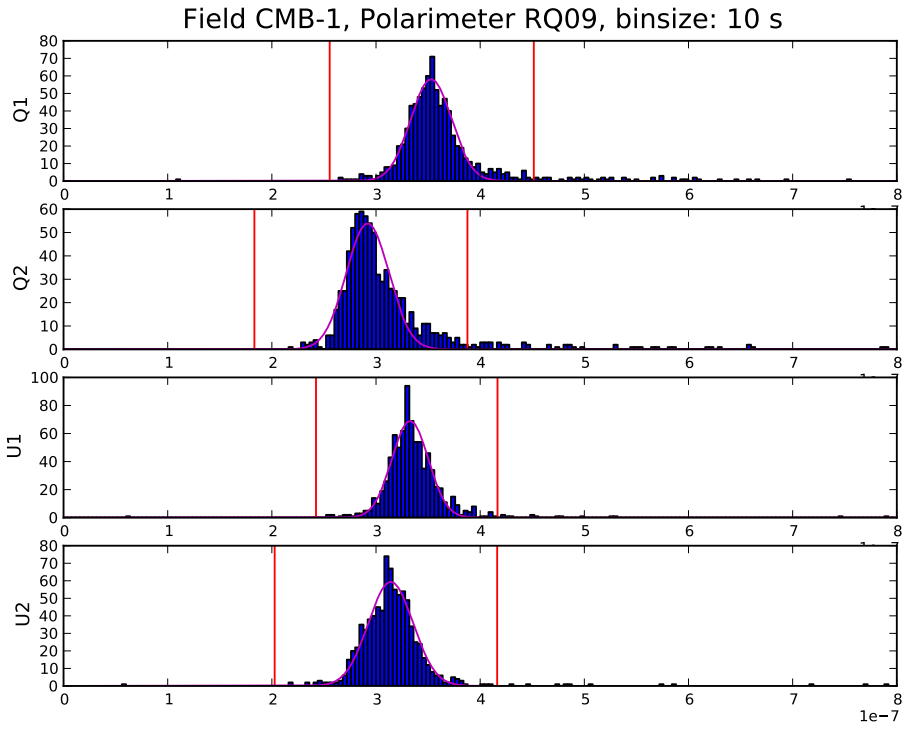

Figure 5.4: Histogram of the Σ_{CES} values for each of the detector diodes on polarimeter RQ09 for CMB field CMB-1. The red lines denote the $\pm 5\sigma_{CES}$ values.

5.1.2.3 Phase Switch Cuts

During the observing period of December 2009 - February 2009, electrical shorts are occasionally observed on the phase-switch AIB board (PIB) stationed directly outside of the cryostat, due to high humidity at the site. The phase-switches are normally biased with a current in the range 0.34 mA to 0.36 mA, and these electrical shorts can cause the bias current of polarimeters RQ11 and RQ12 to spontaneously jump, sometimes doubling the bias current sent to the polarimeters. The noise spectra from data during these periods (for polarimeters RQ11 and RQ12) contains high knee-frequencies, and the data is not used for analysis. Due to the protection circuitry on the MABs (§2.4.1), the biases that are able to reach the phase-switches are limited, and the bias jumps do not cause component failures. If the phase-switch current is found to be outside of the normal range of operation (less than 0.20 mA, or greater than 0.38 mA), the CES-diode is cut.

5.1.2.4 Sidelobe Cuts

Before the apertures in the bottom ground-screen are closed and the upper ground-screen is installed on the mount (§2.2.1.2), the receiver is occasionally subject to spurious radiation leaking into the sidelobes of the beam. During the Q-band observing season, if the Sun is at specific azimuth and elevation regions, a significant increase in the χ^2 of the noise in the map is noticed when the mount scans through specific azimuth and elevation coordinates. A cut for this "Sun-in-the-sidelobes" effect is employed when the mount is within a distinct range of coordinates and the Sun is concurrently within a separate distinct range of coordinates.

5.1.2.5 FFT Cuts

Given the CES for a particular diode, the fast Fourier transform (FFT) of the diode is produced, and the χ^2_{FFT} of the detector diodes' data to the noise model (§4.1.3) is calculated in the 0-0.2 Hz and 0.2-7 Hz range, using

$$\chi^2_{FFT} = \sum_{\nu} \frac{F(\nu) |f_\nu|^2}{P(\nu)}, \tag{5.2}$$

where $F(\nu)$ is the combined filter function, f_ν are the Fourier coefficients of the differenced data time-stream, and $P(\nu)$ is the expected noise spectrum. The mean and variance of the filter function $F(\nu)$, are given by

$$\begin{aligned} \mu &= \sum_{\nu} F(\nu), \\ \sigma^2 &= \sum_{\nu} F(\nu)^2, \end{aligned} \tag{5.3}$$

and the agreement between the fit and the data is quantified as:

$$N_\sigma = \frac{\chi^2_{FFT} - \mu}{\sigma}. \tag{5.4}$$

The χ^2_{FFT} to the 0-0.2 Hz range is calculated before the FFT filters are applied (§5.1.3), and the χ^2_{FFT} to the 0.2-7 Hz range is calculated after the FFT filters are applied. For a given CES-diode, if the χ^2_{FFT} in either of the 0-0.2 Hz or 0.2-7 Hz regions is greater than 4σ, the CES-diode is cut. Although a high-pass filter is applied to the data at frequencies lower that $\sim$0.25 Hz (§5.1.3), the FFT cut in the 0-0.2 Hz range is essential, as the χ^2

of the 0-0.2 Hz range shows a significant correlation with high χ^2s to the CMB maps themselves, and the FFT cut in the 0-0.2 Hz range serves as a simple way to discard data with significant contamination.

5.1.2.6 Min-Max Cuts

The min-max cut is used to identify spikes in the differenced data time-stream. For each CES-diode, the mean and standard deviation of the differenced data time-stream are computed, and the deviation from the mean are computed for each data point. If the deviation of the mean is greater than 7.0 times the standard deviation, the CES-diode is cut.

5.1.2.7 Summary of Data Reduction

A summary of the data cuts employed during the Q-band season, and the percentage of data from each process is given in Table 5.2. A summary of the number of CMB observing hours for each CMB field remaining after data cuts are implemented is given in Table 5.3.

Cut type	Percentage of data cut (percent)
Static	14.6
Scan Duration	5.6
Weather	14.0
Phase-switch	0.6
Glitch	4.6
Sidelobe	6.5
FFT	14.8
Total (including overlap from different cuts)	27.1

Table 5.2: Summary of Data Cuts – Some of these cuts overlap with one another, so the percentages for each individual cut do not add up to the total percentage of data cut.

CMB field	Observing hours	Cut efficiency (%)	Analysis hours
CMB-1	905	84.3	765
CMB-2	703	70.0	492
CMB-3	837	61.4	514
CMB-4	223	74.2	165
Total	2668	72.9	1936

Table 5.3: Summary of CMB Observing Field Integration Times and Cut Efficiencies

5.1.3 Filtering

After the data is been pre-processed, the differenced data time-stream of the CES for each detector diode is Fourier-transformed and the resulting spectra is fitted to the noise model given in §4.1.3. The pipeline employs a high- and low- pass filter to the data, at $\sim$0.25 Hz (2.5 times the scan frequency, which varies depending on the elevation of the mount for the specific observation) and 4.5 Hz respectively. The high-pass filter is designed to suppress scan-synchronous signals, atmospheric fluctuations and $1/f$ noise; the low-pass filter is designed to remove high-frequency spikes, caused by aliasing of the 60 Hz power line noise and imperfections of the electronics boards. The high- and low- pass filtering only removes a small amount of signal, as only two scan harmonics are removed from the high-pass filter, and the beam roll-off at higher frequencies makes it such that very little signal remains in the region where the low-pass filter is implemented. Figure 5.5 (a) shows the Fourier-transform of the differenced data time-stream from a polarimeter diode, and Figure 5.5 (b) show the filtered Fourier-transform of the differenced data time-stream from the same polarimeter diode.

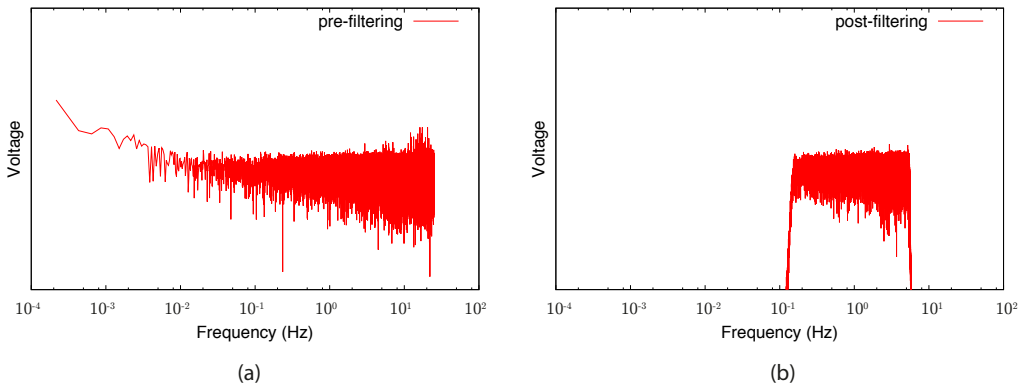

Figure 5.5: Fourier transform of the differenced data time-stream of a typical diode over the duration of a CES: (a) before applying filtering; (b) after applying filtering.

5.2 Data Analysis

After the data is pre-processed, filtered and data cuts are imposed, the time-ordered data from all of the polarization (total power assembly) detector diodes is combined to construct **Q** and **U** polarization maps (**I** temperature maps) for the four CMB fields that QUIET observes. These maps are then used to estimate power spectra and cosmological parameters. A description of the map-making procedure is given in section §5.2.1, and the power spectrum and cosmological parameter estimation is discussed in §5.2.2.

5.2.1 Map Making

The time-ordered data **d** is transformed into a map using a maximum likelihood method; the same process is used to turn differenced total power detector data into a Stokes **I** temperature map, and differenced polarimeter detector data into Stokes **Q** and **U** polarization maps. The maximum likelihood map **m** is related to the matrix that represents the pointing, **P**, and the noise in the time-ordered data, $\mathbf{n}'$, by

$$\mathbf{d} = \mathbf{P}\mathbf{m} + \mathbf{n}'. \tag{5.5}$$

The noise $\mathbf{n}'$ can be split into two components; a correlated component that is a linear combination of orthogonal base functions, and a pure white noise component:

$$\mathbf{n}' = \mathbf{F}\mathbf{a} + \mathbf{n}, \tag{5.6}$$

where the vector **a** contains the amplitudes of the orthogonal base functions, **F** is the matrix that contains the values of the corresponding base functions along the time-ordered data, and **n** represents white noise. Assuming that the white noise and correlated noise are independent of one another, the total noise covariance matrix $\mathbf{N}$ can be expressed as

$$\mathbf{N} = \left\langle \mathbf{n}' \left(\mathbf{n}'\right)^T \right\rangle = \mathbf{F}\mathbf{N_a}\mathbf{F^T} + \mathbf{N_N}, \tag{5.7}$$

where $\mathbf{N_N} = \left\langle \mathbf{n}\mathbf{n}^T \right\rangle$ is the white noise covariance matrix[1], and $\mathbf{N_a} = \left\langle \mathbf{a}\mathbf{a}^T \right\rangle$ is the covariance amplitudes of the orthogonal basis **a**. The maximum likelihood of the data **d**

[1]The white noise covariance matrix $\mathbf{N_N}$ is assumed to be diagonal, but it need not be uniform.

can be written as

$$\mathbf{P}\left(\mathbf{d}\right) = P\left(\mathbf{d}|\mathbf{m},\mathbf{a}\right) P\left(\mathbf{a}|\mathbf{m}\right) P\left(\mathbf{m}\right) \tag{5.8}$$

where $P\left(1|2\right)$ is the conditional probability of 1 under condition 2. Since the CMB sky is deterministic, $P\left(\mathbf{m}\right)$ is constant, and $P\left(\mathbf{a}|\mathbf{m}\right) = P\left(\mathbf{a}\right)$. $P\left(\mathbf{a}\right)$ is furthermore assumed to be Gaussian, and is expressed as

$$P\left(\mathbf{a}\right) = \left(2\pi \det \mathbf{N_a}\right)^{-\frac{1}{2}} \exp\left(-\frac{1}{2}\mathbf{a}^T {\mathbf{N_a}}^{-1}\mathbf{a}\right). \tag{5.9}$$

With the map **m** and the amplitudes of the basis functions **a** fixed, the likelihood of the data is given by the white noise distribution

$$P\left(\mathbf{d}|\mathbf{m},\mathbf{a}\right) = \left(2\pi \det \mathbf{N_N}\right)^{-\frac{1}{2}} \exp\left(-\frac{1}{2}\mathbf{n}^T {\mathbf{N_N}}^{-1}\mathbf{n}\right), \tag{5.10}$$

where **n** = **d - Fa - Pm**. By taking the inverse logarithm of the likelihood (equation (5.8)), a formula for the χ^2 of the data is determined:

$$\begin{aligned} \chi^2 &= -2\ln P\left(\mathbf{d}\right) \\ &= -2\ln\left(P\left(\mathbf{d}|\mathbf{m},\mathbf{a}\right) P\left(\mathbf{a}\right)\right) \\ &= \left(\mathbf{d}-\mathbf{Fa}-\mathbf{Pm}\right)^T {\mathbf{N_N}}^{-1}\left(\mathbf{d}-\mathbf{Fa}-\mathbf{Pm}\right) + \mathbf{a}^T {\mathbf{N_a}}^{-1}\mathbf{a} + C_0, \end{aligned} \tag{5.11}$$

where C_0 is a constant. Minimizing the χ^2 in equation (5.11) with respect to the map **m**, a formula for **m** is obtained:

$$\mathbf{m} = \left(\mathbf{P}^T {\mathbf{N_N}}^{-1}\mathbf{P}\right)^{-1} \mathbf{P}^T {\mathbf{N_N}}^{-1}\left(\mathbf{d}-\mathbf{Fa}\right), \tag{5.12}$$

which is an unbiased and minimum-variance map. Furthermore, if the noise in the underlying map is understood and Gaussian, **m** becomes

$$\mathbf{m} = \left(\mathbf{P}^T \mathbf{N}_\mathbf{N}^{-1} \mathbf{P}\right)^{-1} \mathbf{P}^T \mathbf{N}_\mathbf{N}^{-1} \mathbf{d}, \tag{5.13}$$

where the noise covariance matrix of the time-ordered data, $\mathbf{N_m}$, is

$$\mathbf{N_m} = \left(\mathbf{P}^T \mathbf{N}_\mathbf{N}^{-1} \mathbf{P}\right)^{-1}. \tag{5.14}$$

These equations become slightly more complex with the addition of filters, and the resulting equations can be found in literature [41] [42].

5.2.2 Power Spectra and Cosmological Parameter Estimation

Given the unbiased map **m** and its noise covariance matrix $\mathbf{N_m}$, the CMB power spectra $\mathcal{C}_b^{XX}$ are calculated for the temperature and polarization spectra ($\mathcal{C}^{TT}$, $\mathcal{C}^{EE}$, and $\mathcal{C}^{BB}$), as well as their cross-spectra ($\mathcal{C}^{TE}$, $\mathcal{C}^{TB}$, and $\mathcal{C}^{EB}$)[2], in multipole moment bins b using a Newton-Rhapson method [43]. If the likelihood function is continuous and has a maximum, then it can be locally approximated by a Gaussian near the peak. This Gaussian approximation is determined by truncating the natural logarithm of the likelihood function

[2]The cross-spectra are not analyzed in this thesis.

about the multipole moments C_b to second order δC_b, hence

$$\ln \mathcal{L}\left(C+\delta C\right)=\ln \mathcal{L}\left(C\right)+\sum_{b}\frac{\partial \ln\left(C\right)}{\partial C_b}\delta C_b+\frac{1}{2}\sum_{bb'}\frac{\partial^2 \ln\left(C\right)}{\partial C_b \partial C_{b'}}\delta C_b \delta C_{b'} \tag{5.15}$$

Once the Gaussian peak of the likelihood has been estimated, it is possible to solve directly for the δC_b that maximize the likelihood (rather than making multiple evaluations of the likelihood) using

$$\delta C_b=-\sum_{b'}\left[\frac{\partial^2 \ln\left(C\right)}{\partial C_b \partial C_{b'}}\right]^{-1}\frac{\partial \ln\left(C\right)}{\partial C_{b'}}. \tag{5.16}$$

The first and second derivatives[3] are given by

$$\frac{\partial \ln \mathcal{L}\left(C\right)}{\partial C_{b'}}=\frac{1}{2}\mathrm{Tr}\left[\left(\mathbf{m}\mathbf{m}^T-\mathbf{C}\right)\left(\mathbf{C}^{-1}\mathbf{C}_{,b'}\mathbf{C}^{-1}\right)\right], \tag{5.17}$$

and

$$\begin{aligned}-\frac{\partial^2 \ln \mathcal{L}\left(C\right)}{\partial C_b \partial C_{b'}} \equiv & \mathcal{F}_{bb'} \\ = & \frac{1}{2}\mathrm{Tr}\left[\left(\mathbf{m}\mathbf{m}^T-\mathbf{C}\right)\left(\mathbf{C}^{-1}\mathbf{C}_{,b}\mathbf{C}^{-1}\mathbf{C}_{,b'}\mathbf{C}^{-1}-\frac{1}{2}\mathbf{C}^{-1}\mathbf{C}_{,bb'\mathbf{C}^{-1}}\right)\right] \\ & +\frac{1}{2}\mathrm{Tr}\left(\mathbf{C}^{-1}\mathbf{C}_{,b}\mathbf{C}^{-1}\mathbf{C}_{,b'}\right),\end{aligned} \tag{5.18}$$

where Tr is the trace, $\mathbf{C}$ is the total covariance matrix, $\mathbf{C}_{,b}$ denotes the partial derivative of $\mathbf{C}$ with respect to C_b, and $\mathcal{F}_{bb'}$ is the curvature matrix. Given that the function is not

[3] See [43] for details.

perfectly Gaussian, iterations are needed to find the peak that corresponds to

$$\frac{\partial \ln \mathcal{L}(C)}{\partial C_b} = 0. \tag{5.19}$$

By taking the ensemble average[4] of the curvature matrix (assuming that theory is correct in stating that the signal and noise are independent with zero mean, $\langle \mathbf{m}\mathbf{m}^T \rangle = \mathbf{C}$), the first term in equation (5.18) disappears and only the second term, the *Fisher matrix*, remains[5]. Equation (5.18) is simplified to

$$\mathcal{F}_{bb'} = \frac{1}{2}\mathrm{Tr}\left(\mathbf{C}^{-1}\mathbf{C}_{,b}\mathbf{C}^{-1}\mathbf{C}_{,b'}\right). \tag{5.20}$$

This makes the estimator of a_i quadratic in the data $\mathbf{d}$, and gives the result

$$\delta C_b = \frac{1}{2}\sum_{b'} \mathcal{F}^{-1}_{bb'} \mathrm{Tr}\left[\left(\mathbf{m}\mathbf{m}^T - \mathbf{C}\right)\left(\mathbf{C}^{-1}\mathbf{C}_{,b'}\mathbf{C}^{-1}\right)\right]. \tag{5.21}$$

Once the resulting power spectra are computed, the cosmological parameters θ can be computed using a brute-force exploration of the pixel-space likelihood using

$$\mathcal{L}(\theta) \propto \frac{-\frac{1}{2}\mathbf{d}^T\mathbf{C}^{-1}(\theta)\,\mathbf{d}}{\sqrt{|\mathbf{C}(\theta)|}}, \tag{5.22}$$

[4]By averaging over sufficiently large volumes, the measured statistic (volume average) is equivalent to the ensemble average (statistical average).

[5]While not perfectly Gaussian, the likelihood is sufficiently Gaussian, which makes this a very good approximation.

where $\mathbf{C}(\theta)$ is the covariance matrix parameterized by θ, evaluated with a smooth spectrum, C_b The scalar-to-tensor ratio r, and the degree of fit of the E-mode power spectrum to the Λ-CDM model q are obtained using this exploration of the pixel-space likelihood, and are seen in §6.2.

5.3 Systematic Errors

The PCL pipeline is used to determine the systematic errors for the QUIET experiment (the computational efficiency of the PCL pipeline allows many iterations of the data analysis to be performed). Figure 5.6 shows the systematic errors related to the Q-band observations for both the E- and B- mode power spectra, along with their statistical error, and compares these results to the expected power from the Λ-CDM model. The systematics error (for each effect) is determined by simulating and propagating calibration uncertainties throughout the full analysis pipeline, and evaluating the difference in the E- and B-mode power spectrum when different conditions/(analysis methods) are used. The predominant sources of error are statistical errors; a detailed study of the systematic errors shows that for almost all of the E- and B- mode multipole bins ℓ, the systematic errors are generally an order of magnitude less than the statistical error for the bin. The systematic errors that are examined in this analysis are the following:

1. *Beam Window Function*: the beam window functions (§4.5) are well defined using the central polarimeter data (Tau A observations) and the paired total power assembly detector data (Jupiter observations). The difference between the beam window function of the central polarimeter to those of the paired total power detectors is

statistically significant: this effect is due to the difference in locations between the central detector and the detectors on the outer edge of the array. A systematic error is assigned based on the difference between the central polarimeter and total power assembly detectors beam window function.

2. *Pointing*: residuals in the pointing of the telescope lead to distortions in the maps created. A systematic error is assigned based on the pointing difference between two independent models; a fiducial model used for the published analysis, and a second model based on a different set of calibration observations.

3. *Responsivity of Detector Diodes*: the responsivity (§4.2.1) of the detector diodes fluctuates as a function of the electronics bias temperature. These fluctuations occur on short ($\sim$0.5 hour) and long ($\sim$24 hour) timescales. The responsivity is corrected to account for these temperature fluctuations of the electronics. A systematic error is assigned based on the difference between employing or not employing the temperature-corrected responsivity model; this is an upper-limit systematic, as this effect is corrected for. If the calculated responsivity correction for a detector diode is zero, this implies that the detector diode is insensitive to temperature fluctuations of the electronics, and requires no correction.

4. *Polarization Angle of Detector Diodes*: the polarization angles of the detector diodes are measured using various calibration sources. For the final analysis, measurements from the Moon are used, with the Tau A and wire-grid measurements being used as cross-checks. A systematic error is assigned based on using the Tau A and wire-grid measurements to determine the polarization angle of the detector diodes

rather than the Moon.

5. $\mathbf{I} \rightarrow \mathbf{Q}/\mathbf{U}$ *Leakage*: The $\mathbf{I} \rightarrow \mathbf{Q}(\mathbf{U})$ leakage for the detector diodes is $\sim$1.0 % (0.2 %) for the Q (U) detector diodes. This effect is not corrected for in the analysis, but a systematic error is assigned based on these values. The effect of leakage is not corrected for because the effect is very small and does not affect the results of our experiment. In future experiments, where the leakage might effect the ability to distinguish power in the B-mode spectrum, the effect will be corrected for.

6. *Sun in the Sidelobes*: Data cuts are imposed to remove any data that is known to have spurious radiation leaking into the sidelobes of the beam from the Sun. It is possible however that some of this contamination has not been removed from the Q-band observing season data. Full-season maps for each detector diode in Sun-centered coordinates are produced (corresponding to the data set after data cuts are implemented) and these maps are used to add contamination to full-pipeline CMB simulations. The excess power measured in the simulations is used as the systematic uncertainty.

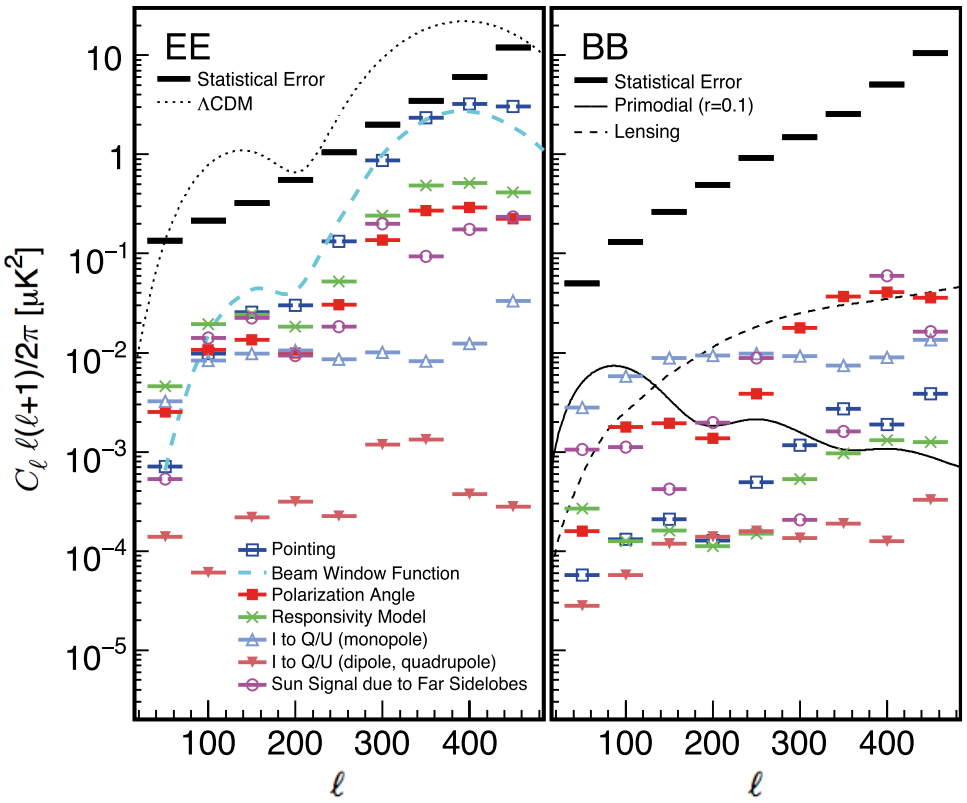

Figure 5.6: A plot of the power level of the E- and B- mode systematic errors, plotted with the power level of the E- and B- mode statistical error and the power level of the E- and B- mode Λ-CDM model [44].

Chapter 6

Results

The analysis and results from the QUIET Q-band observing season (2008 October –2009 June) are presented in this chapter.

The task of measuring CMB polarization is difficult: in order to accurately measure the faint polarization signal on the sky (the CMB is polarized of the order of 1 part in 10^6 of the temperature of the sky), thousands of observing hours must be collected in order to be able to detect the signal through the inherent noise of the instrument and atmosphere. The procedure for transforming time-ordered data into celestial maps, and obtaining the resulting power spectra and the cosmological parameters is described in §5.2. Before power spectra and cosmological parameters are calculated, a stringent set of tests are performed on the data to ensure that any significant source of contamination is removed from the data set. These tests are performed before looking at the power spectra and cosmological parameters, and we call this analysis method *blind analysis*. Blind analysis is performed

by evaluating *null tests*, which are described in §6.1. The results of the analysis for the Q-band observing season are presented in §6.2.

6.1 Null Tests

The most important factors in measuring very faint and noisy signals is to perform observations with high-sensitivity detectors and to remove significant sources of contamination from the data set. Null tests can be employed if the observed signal is expected to be constant over the duration of the measurement. Null tests consist of dividing the data into two equal halves (data sets A and B) using some metric[1], obtaining a differenced signal from the two halves (data set $C = B - A$) and checking that the differenced signal is consistent with noise. Figure 6.1 demonstrates the process by which a null map is obtained using data sets A and B.

The removal of contaminated data using null tests is an iterative process: If the null map produced from a null test is inconsistent with noise, further data cuts are implemented to ensure that contamination sources are removed from the data. This process is repeated until the produced null map is consistent with noise. The Q-band observing season consists of 2668 hours of CMB observations using an array of 17 polarimeters. When examining a large data set such as this, many null tests need to be designed specifically to test for systematic errors that we are concerned about, to ensure that any significant contamination

[1]This can be achieved by dividing the signal in time, dividing the signal by independent receivers, or by other means.

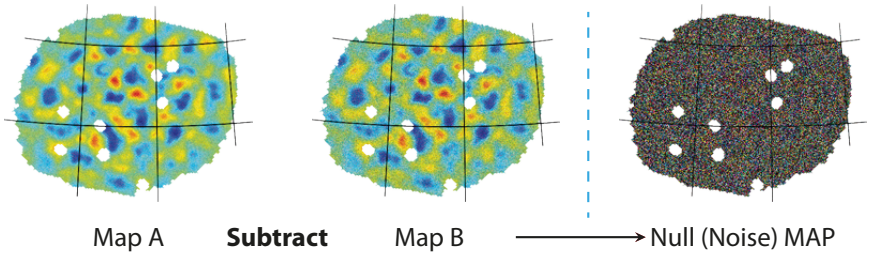

Figure 6.1: Illustration of how a null map is constructed. If data sets A and B are equivalent (with the exception of noise), the resultant differenced map should be consistent with noise. In the example shown, map A and map B are E-mode maps generated using observations from CMB field CMB-1. Map images courtesy of Hans Kristian Eriksen.

is removed before analysis on the resulting power spectra and cosmological parameters is performed.

6.1.1 Expected Statistics From Null Tests $(\mathcal{N}(0,1))$

The null test suite divides the Q-band season data by temporal intervals, spatial intervals, by subsets of polarimeters in the array, by weather conditions at the site, and by the temperature of the electronics used to bias the array. This suite of null tests is chosen to test for as many different systematic errors as possible, and 21 independent null tests are performed[2]. An equal amount of data (in terms of observing hours) is used to construct maps A and B for each null test; if a specific null test does not have an equal number of observing hours for the construction of maps A and B, the lower number of observing

[2]The number of null tests is based on the number of tests we believe are essential to convince ourselves that we have removed any significant sources of contamination. For our array and observing season, 21 independent tests are considered.

hours is used for both maps.

Before outlining the suite of null tests performed, the theory of how the null tests are used, and what statistical results should be observed from them, is explained. A typical null test from the Q-band analysis is show in Figure 6.2. One can see that the E- and B-mode power spectra multipole moments are consistent with zero signal. By definition, the null power for a multipole moment divided by its error is denoted by χ (and called a *chi value*); if the χ values from the power spectrum are consistent with noise, they should be described by a number drawn from a normal distribution of mean $\mu = 0$, and standard deviation $\sigma = 1$ (a distribution of $\mathcal{N}(0, 1)$).

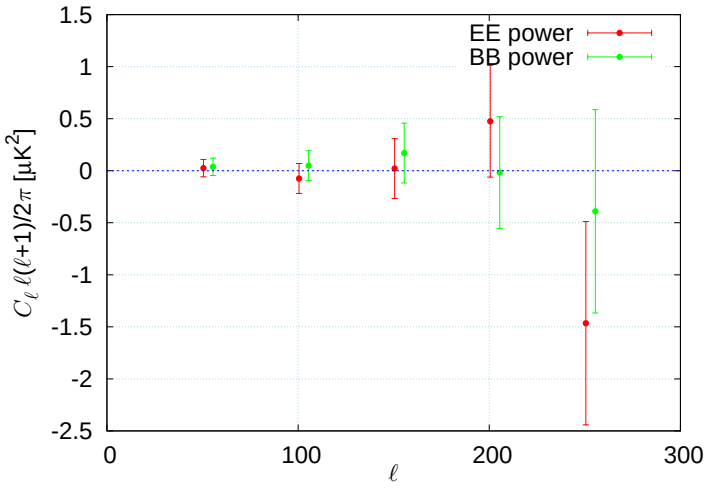

Figure 6.2: Typical null power spectra from a Q-band null test (for the E- and B- mode differenced maps).

Given that the χ values from the null power spectra should be drawn from a $\mathcal{N}(0, 1)$

distribution, two statistical results should be observed:

1. When plotted as a normalized histogram, the χ values should fill out a normal distribution of $\mathcal{N}(0,1)$ (shown in Figure 6.3 (a)).

2. The square of the χ values (χ^2), should be drawn from a standard chi-squared distribution with the appropriate number of degrees of freedom. The quantity *probability-to-exceed* (PTE) is defined to be the normalized fraction of the area under the chi-squared distribution that is greater than the calculated χ^2 value (shown in Figure 6.3 (b)). The PTEs of the χ^2 values should be uniformly distributed; it is equally likely for an individual χ^2 value to be lower or higher than the expected value. The PTE of the χ^2 values for each CMB observing field (the sum of the χ^2 values from the the E- and B- mode null tests) should also be uniformly distributed.

The 21 independent null tests are performed on each of the four CMB fields that QUIET observes, giving a statistical data set of 840 χ-values; this gives a sufficiently large data set to observe the statistical results discussed above.

6.1.2 Null Suite

The temporal null suite is designed to investigate the effects of possible contamination due to differing observing conditions at the site (i.e. between the summer and winter months), and the performance and consistency of the data received from the array as a function of time. The temporal null suite consists of five null tests, dividing the observing season by:

1. interleaved CESs (*interleaved*, splitting up odd and even CESs);

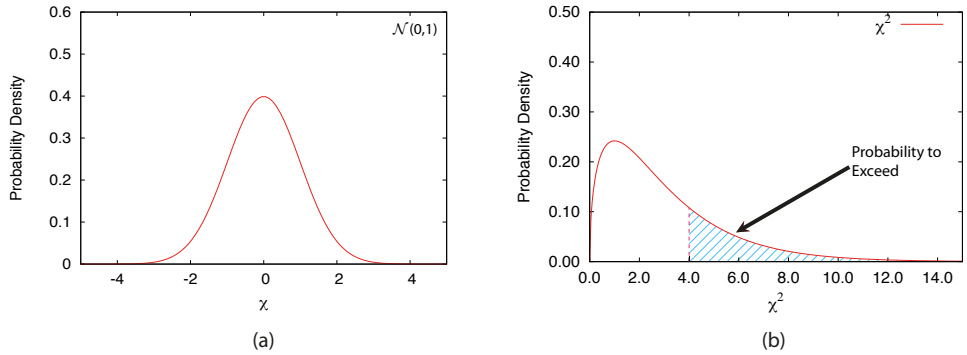

Figure 6.3: (a) When normalized, the χ values from the QUIET null suite should produce a normal distribution $\mathcal{N}(0,1)$. (b) An example chi-squared distribution, with $k = 3$ degrees of freedom. If the calculated χ^2 value obtained for a multipole point of a power spectrum was $\chi^2 = 4$, the PTE would be the ratio of the shaded area (in blue) to the total area under the chi-squared distribution. The probability-to-exceed for a χ^2 value of 4 for a chi-squared distribution with three degrees of freedom is PTE$\sim$0.262.

2. the first and third quarters of the season and the second and fourth quarters of the season (*quart*);

3. the first half of the season and the second half of the season (*season*);

4. the first and fourth quarters of the season and the second and third quarters of the season (*tandem*);

5. times where there was possible contamination leaking in to the sidelobes of the QUIET beam from the Sun and times when there was not (*sidelobes*).

The spatial null suite is designed to investigate the effects of contamination sources present at specific spatial coordinates: the topography of the site changes with azimuth and elevation and spurious radiation may be able to leak into the sidelobes of the QUIET

beams at specific azimuth, elevation and deck coordinates. The spatial null suite consists of four null tests, dividing the observing season by:

1. observations in the defined azimuth in the direction east of the QUIET site and observations in the defined azimuth direction west of the QUIET site (*pointaz*);

2. observations at the defined deck angle of 45° and observations not at the defined deck angle of 45° (*pointdk45*);

3. observations at the defined deck angle of 90° and observations not at the defined deck angle of 90° (*pointdk90*);

4. observations in the defined elevation angle of $43° < \theta < 64°$ and observations in the defined elevation angle of $64° < \theta < 85°$ (*pointel*).

The polarimeter null suite is designed to investigate the consistency of data quality between polarimeters in the array, and to ensure that each polarimeter detector diode is functioning properly. Testing the consistency of data quality between the polarimeters in the array also verifies that the QUIET pointing model is performing to the standard we expect[3]. The polarimeter null suite consists of nine null tests, dividing the observing season by (see Figure 2.22 in §2.4.1):

1. odd and even numbered polarimeters (*polalt*, see Figure 2.22);

2. the polarimeters with the highest central frequencies and the polarimeters with the lowest central frequencies (*polfreq*);

[3]If the pointing model is not performing to the standard that we expect, the polarimeters that make up the outer ring of the array will not perform as well as the seven central polarimeters of the array.

3. a horizontal division of the polarimeters on the focal plane (*polhorizontal*, polarimeters RQ07-RQ15 and polarimeters RQ00-RQ06);

4. polarimeters on MAB 1 and polarimeters on the other two MABs (*polmab1*);

5. polarimeters on MAB 2 and polarimeters on the other two MABs (*polmab2*);

6. polarimeters on MAB 3 and polarimeters on the other two MABs (*polmab3*);

7. a vertical division of the polarimeters on the focal plane (*polvert1*, polarimeters RQ00, RQ01, RQ03, RQ04, RQ07, RQ08, RQ12, RQ13, and polarimeters RQ02, RQ05, RQ06, RQ09-RQ11, RQ14, RQ15);

8. a second vertical division of the polarimeters on the focal plane (*polvert2*, polarimeters RQ00, RQ03, RQ04, RQ07-RQ09, RQ12, RQ13 and polarimeters RQ01, RQ02, RQ05, RQ06, RQ10, RQ11, RQ14, RQ15);

9. the seven polarimeters in the center of the array and the polarimeters located in the outer ring of the array (*polrad*).

The weather and physical property of the electronics null suite is designed to investigate whether or not the data quality of observations at lower and higher PWV or humidity is consistent with one another, and whether or not the data quality of observations at lower or higher enclosure temperatures is consistent with one another. The weather and physical property of the electronics null suite includes three null tests, dividing the observing season by:

1. low and high humidity, as measured by the APEX weather station (*apexhumidity*)

2. low and high PWV, as measured by the APEX weather station (*apexpwv*)

3. low and high temperature of the bias electronics (*tencreg*).

Table 6.1 summarizes the null test suite.

Null test name	Division	Evaluates
apexhumidity	weather	observing conditions
apexpwv	weather	observing conditions
interleaved	temporal	time-dependence
pointaz	spatial	pointing
pointdk45	spatial	pointing
pointdk90	spatial	pointing
pointel	spatial	pointing
polalt	polarimeter	consistency of data quality
polfreq	polarimeter	consistency of data quality
polhorizontal	polarimeter	consistency of data quality
polmab1	polarimeter	consistency of data quality
polmab2	polarimeter	consistency of data quality
polmab3	polarimeter	consistency of data quality
polvert1	polarimeter	consistency of data quality
polvert2	polarimeter	consistency of data quality
polrad	polarimeter	consistency of data quality
quart	temporal	time-dependence
season	temporal	time-dependence
sidelobe	possible contamination times	possible contamination sources
tandem	temporal	time-dependence
tencreg	electronics bias temperature	observing conditions

Table 6.1: Summary of the 21 null test suite. Each null test evaluates one of the following criteria: *consistency of data quality*, whether the performance of polarimeters in the array is consistent with one another and whether or not any polarimeters malfunctioned; *observing conditions*, whether the quality of the data taken during during different observing conditions (as measured by some metric, such as APEX weather variables or the temperature of the electronics enclosure) is consistent; *pointing*, whether or not the quality of data at different azimuth, elevation and deck angles is consistent; *possible contamination sources*, whether or not data taken at specific times when known possible contamination sources were present is consistent with data taken at times where there is no known possible contamination sources; and *time-dependence*, whether or not the quality of data taken during different temporal periods is consistent.

6.1.3 Results from the Null Suite

The χ and χ^2 distributions obtained from the QUIET null suite are shown in Figure 6.4; Table 6.2 provides the PTE for the χ^2 of each CMB observing field, and for the sum of the four observing fields together.

The top panel of Figure 6.4 shows the χ distribution, which is Gaussian in shape. It can be seen that there is a slight residual bias in the χ distribution; the distribution has, in fact, a mean of $\mu = 0.19$ and standard deviation $\sigma = 1.01$. Analysis determines this bias to have a negligible effect on the E- and B- mode power spectra. This χ-bias is also seen using the PCL pipeline, and can be removed using a cross-correlation technique: for the power spectra, cross-correlations between pointing-division maps are included and auto-correlations are excluded. This eliminates the noise-bias and thus the residual bias as well. The bottom panel of Figure 6.4 shows the χ^2 PTE distribution [44], which is uniform within error.

To our knowledge, QUIET is the only CMB polarization experiment to present the results of their χ distribution from their null suite; the χ distribution is more stringent than the χ^2 distribution, which is (mostly) insensitive to residual noise biases. Given that the χ and χ^2 distribution are consistent with expected results, the summed maps are constructed and the power spectra and cosmological parameters are estimated.

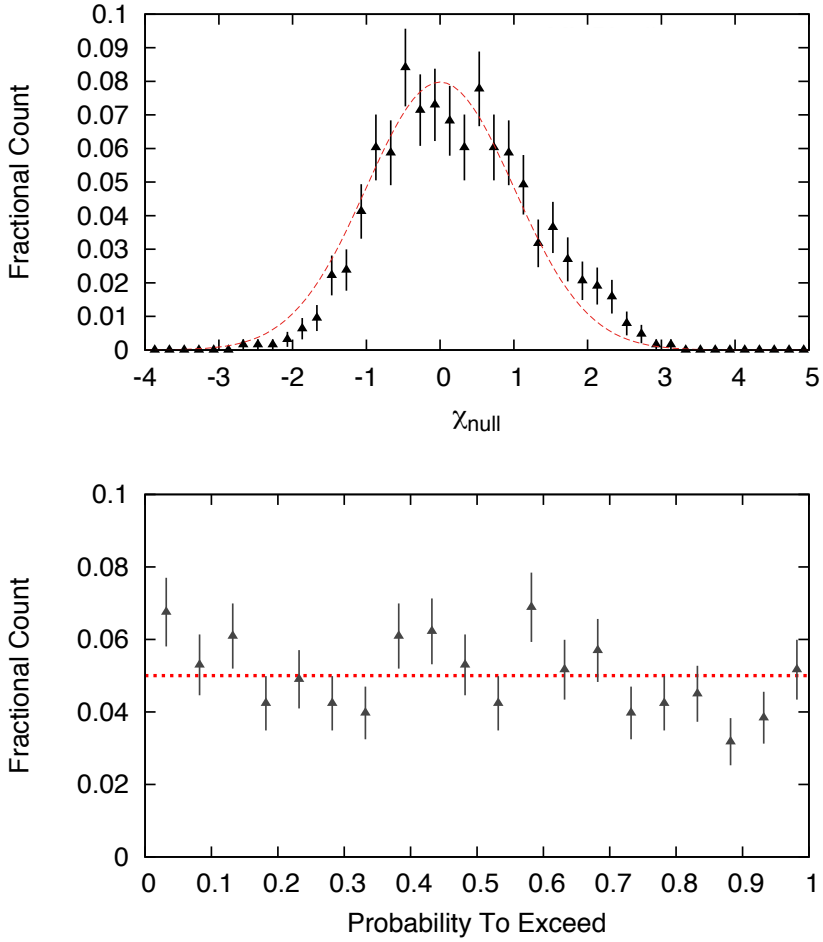

Figure 6.4: Top panel: Histogram of χ-values, given in terms of a fractional count, with the expected normal distribution $\mathcal{N}(0,1)$ normalized to the fractional count (red dashed line). Bottom panel: Histogram of χ^2 PTEs, given in terms of fractional count, with the expected fractional uniform distribution (red dashed line).

CMB field	PTE
CMB-1	0.0655
CMB-2	0.4294
CMB-3	0.2322
CMB-4	0.2827
Total	0.0585

Table 6.2: PTEs for the QUIET CMB Observing Fields (given individually for each field, and for the sum of the four fields together).

6.2 Results from the Q-band Observing Season

6.2.1 Stokes $\mathbf{I}, \mathbf{Q}, \mathrm{U}$ Maps and the TT Power Spectrum

Figure 6.5 (a) shows a Stokes $\mathbf{I}$ map created using the differenced data time-stream from the total power detectors; and Figure 6.5 (b) shows Stokes $\mathbf{Q}$ and $\mathbf{U}$ maps created using the differenced data time-stream from the polarization detectors; all maps are constructed from observations of CMB field CMB-1. After the maps are created (using equation (5.13)), multipole power moments for ℓ-modes of $\ell<15$ are removed[4], and unwanted pixels in the maps are removed during a post-processing step: all 54 compact point sources from the 7-year WMAP catalog [45] are masked out from the $\mathbf{Q}/\mathbf{U}$ polarization maps (these 54 compact point sources are distributed among our observing fields), removing a total of 4% of the observing area from the CMB fields (the masking effect is seen as white areas in the maps shown in Figure 6.5 (b)[5]). The resulting TT (Stokes $\mathbf{I}$) power spectrum is shown in Figure 6.6.

[4]This corresponds to angular scales larger than those QUIET is able to resolve due to the size of the CMB fields it observes, $15^\circ \times 15^\circ$.

[5]In Figure 6.5 this masking is only shown for the $\mathbf{Q}/\mathbf{U}$ polarization maps because these maps are further processed to determine publishable polarization power spectra. In order to obtain publishable temperature power spectra from our data analysis, this masking would have to be performed on the Stokes $\mathbf{I}$ temperature maps as well.

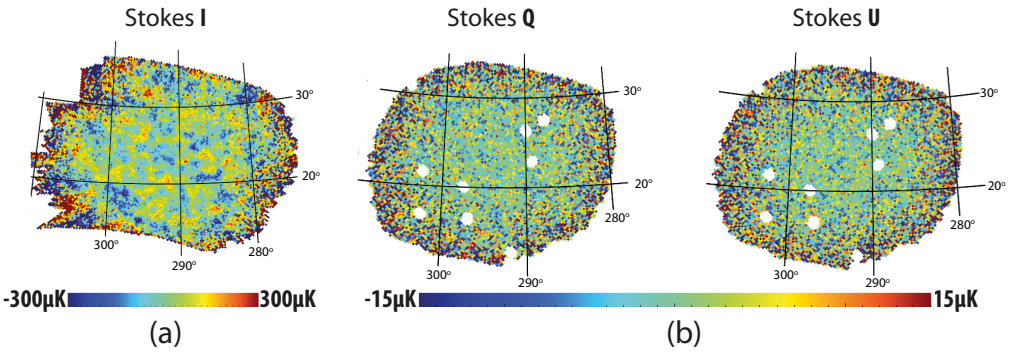

Figure 6.5: Galactic coordinate maps created from observations of CMB field CMB-1. (a) Stokes **I** (temperature) map; (b) Stokes **Q** and **U** polarization maps. All map images courtesy of Hans Kristian Eriksen.

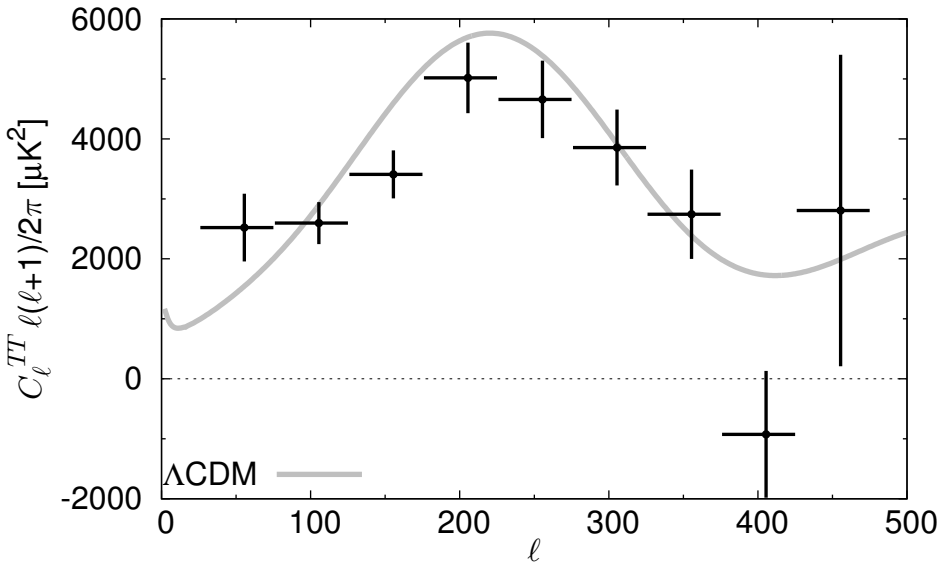

Figure 6.6: TT power spectrum (black), with the expected curve from the Λ-CDM model (grey).

6.2.2 E- and B- Mode Maps, Power Spectra and Cosmological Parameters

Examples of the published E- and B- mode maps are shown in Figure 6.7. In this figure, there is clear structure in the E-mode map, and the B-mode map is consistent with zero signal; the observed noise features in the B-mode map are of the order of the Q-band beam size (27.3′), as is the size of the point-source masking.

Using the four CMB observing fields, the resultant E- and B- mode power spectra are ob-

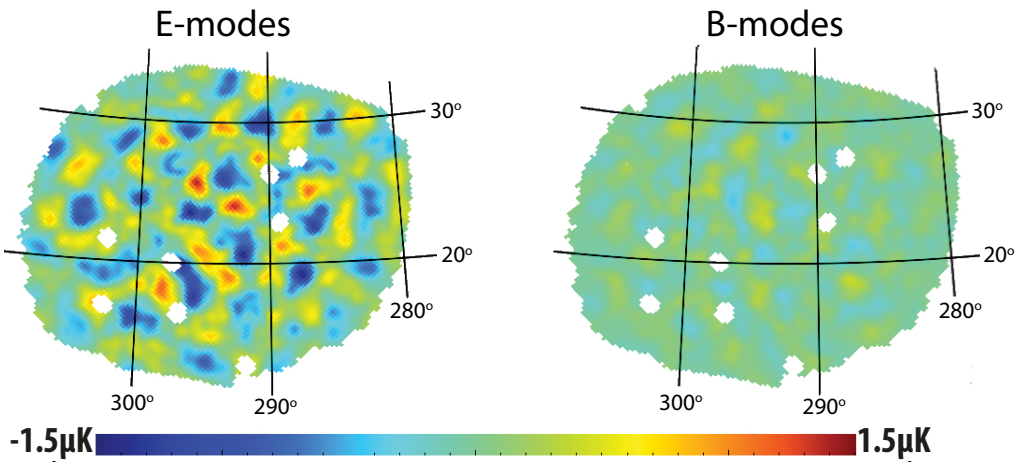

Figure 6.7: E- and B- mode maps created using observations from CMB field CMB-1 [44]. Map images courtesy of Hans Kristian Eriksen.

tained, and are shown in Figure 6.8. These results confirm the only previous detection of the first acoustic peak of the E-mode power spectrum (seen in the interlay of the E-mode power spectrum, between multipole moments of $50 < \ell < 200$) [18], and the B-mode

power spectrum is found to be consistent with noise. The E-mode spectrum is consistent with the Λ-CDM model; the χ^2 from the power spectra result in a PTE of 0.45. By taking the ratio of the power of the B-mode spectrum to the E-mode spectrum in the first three ℓ bins, an upper limit on the tensor-to-scalar ratio is determined[6]. The tensor-to-scalar ratio is found to be $r = 0.52^{+0.97}_{-0.81}$ ($r < 2.4$ at 95% confidence limits), providing one of the best upper limits to date on the B-mode spectrum. Fitting only a free amplitude, q, to the E-mode power spectrum relative to the 7-year best-fit WMAP Λ-CDM spectrum (hence the Λ-CDM spectrum is multiplied by a floating variable q, and the value of q that gives the best agreement with the QUIET Q-band E-mode spectrum is calculated), a value of $q = 0.94 \pm 0.09$ is found[7].

Figure 6.9 shows the QUIET E-mode power spectrum and upper limits on the B-mode power spectrum (95 % confidence limits), compared to that of recent CMB experiments.

6.2.3 Q-band Foreground Analysis

In Q-band, the dominant foreground contamination source is Galactic synchrotron radiation. In order to minimize contribution from foreground contamination, the QUIET observing fields are selected to be far from the Galactic plane (where foreground contamination in strongest); so the amount of foreground radiation is expected to be small. In

[6]Our ability to measure r (§1.4.1) is limited by our ability to resolve power in the B-mode spectrum.

[7]The main science goal of Q-band is to measure polarization power spectra (specifically, the first three peaks of the E-mode spectrum). While this provides valuable information regarding the scalar-to-tensor ratio r, it is not able to compute a full set of Λ-CDM parameters (which require higher ℓ multipole moments, and are best described by the temperature angular power spectrum).

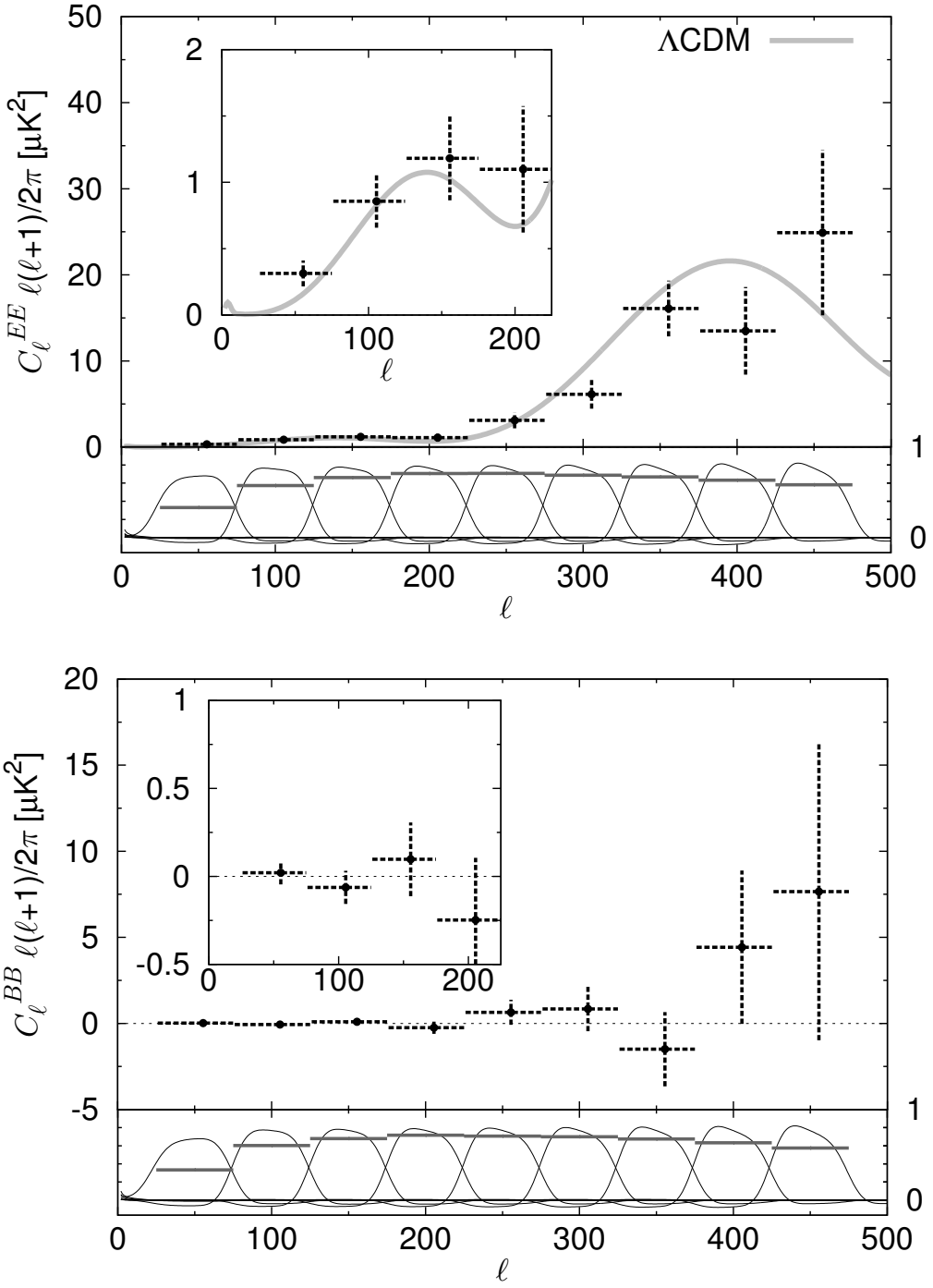

Figure 6.8: E- (top panel) and B- (bottom panel) mode power spectra. The theoretical Λ-CDM curve is also shown for the E-mode power spectra.

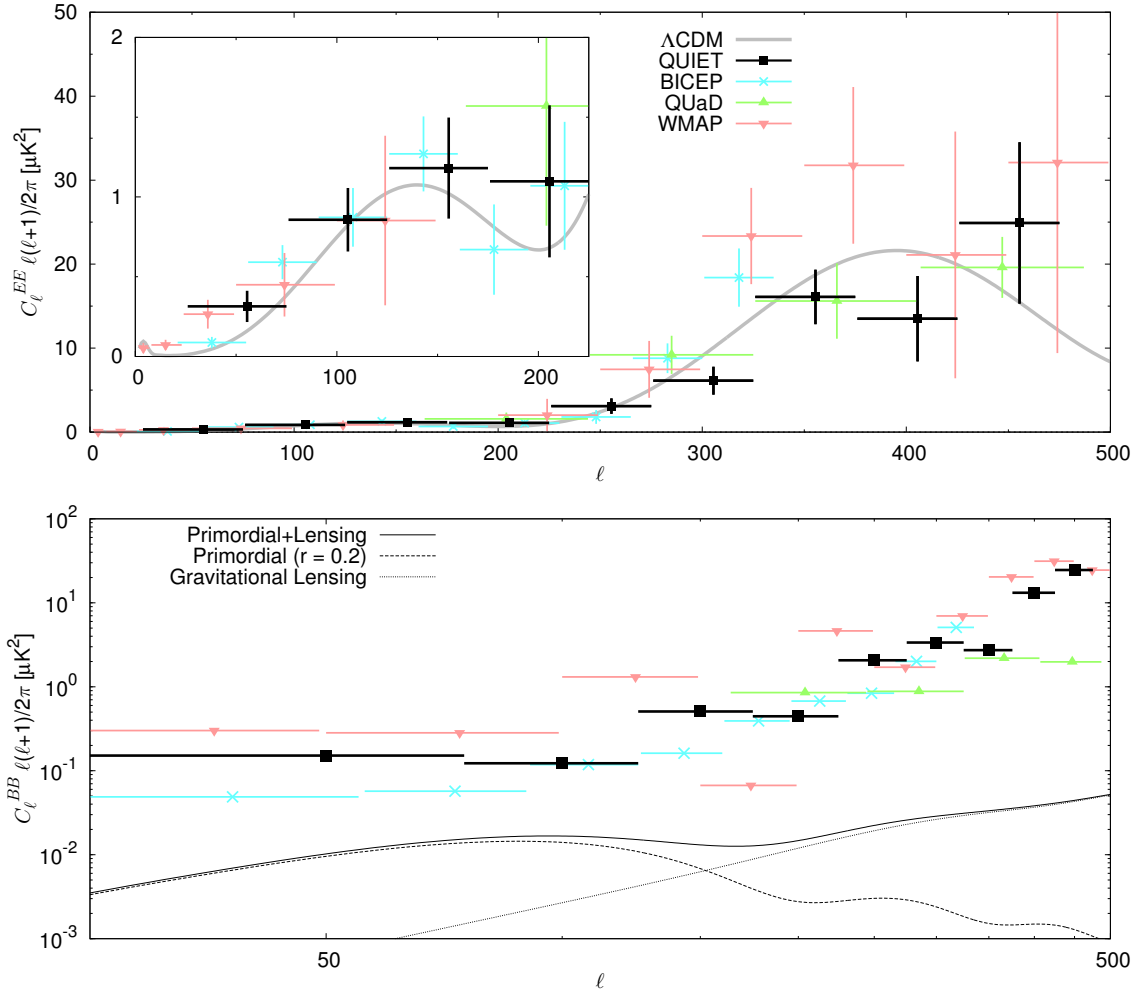

Figure 6.9: The E-mode power spectrum and the upper limits on the B-mode power spectra (95% confidence limits) from the QUIET Q-band observing season (black) shown with the BICEP, QUAD, and WMAP experiments for multipole moments of $\ell < 500$. The top figure shows the E-mode angular power spectrum along with the fit from the E-mode Λ-CDM model. The bottom shows the B-mode angular power spectrum along with the primordial gravitational wave (long-dashed line) B-mode, lensing (short-dashed line) B-mode, and summed (solid line) B-mode Λ-CDM model.

Figure 6.10, the E-mode power spectra is shown for each CMB field [44]. The CMB-1 E-mode band power for the first bin is $0.55 \pm 0.14\ \mu\mathrm{K}^2$, which corresponds to a 3-σ outlier relative to the expected Λ-CDM band power of $0.13\ \mu\mathrm{K}^2$.

In order to estimate the expected amount of Q-band synchrotron radiation in the CMB fields QUIET observes, the WMAP 7-year K-band (23 GHz) map is processed to estimate its band power, $\hat{\mathcal{C}}^{KK}$, as well as the cross-spectra with the QUIET Q-band data, $\hat{\mathcal{C}}^{QK}$. These results, along with the QUIET $\hat{\mathcal{C}}^{QQ}$ band powers, are shown for the ℓ=50 bin in Table 6.3. In the WMAP 7-year $\hat{\mathcal{C}}^{KK}$ band power, there is significant EE power in CMB field CMB-1: for ℓ=50, the band power is $17.4 \pm 4.7\ \mu\mathrm{K}^2$, which is well above the band power signal from the CMB, and we can therefore consider the signal as a pure foreground[8]. A signifiant cross-correlation between the WMAP 7-year K-band data and the QUIET Q-band data is found, confirming that the excess EE power in CMB field CMB-1 is likely due to foreground contamination, and is consistent with a typical synchrotron foreground spectrum. The WMAP $\mathcal{C}^{KK}_{\ell=50}$ result is extrapolated to the QUIET Q-band frequency (assuming a spectral index of β=-3.1 [46]), and the expected band power in $\mathcal{C}^{QK}_{\ell=50}$ and $\mathcal{C}^{QQ}_{\ell=50}$ is calculated to be

$$\begin{aligned} \mathcal{C}^{QK}_{\ell=50} &= 2.57 \pm 0.69\ \mu\mathrm{K}, \\ \mathcal{C}^{QQ}_{\ell=50} &= 0.38 \pm 0.10\ \mu\mathrm{K}. \end{aligned} \tag{6.1}$$

[8] Although WMAP 7-year Q-band data exists (close to the QUIET Q-band frequency), the foreground signal is on the same order of, and difficult to distinguish from, that of the CMB.

The expected synchrotron band power $\mathcal{C}_{\ell=50}^{QQ}$ is close to what we observe with the QUIET Q-band receiver. We therefore conclude that the excess EE power seen in the $\ell = 50$ bin of CMB field CMB-1 is indeed from synchrotron emission. Except for the expected amount of residual power in the first multipole bin ($\ell = 50$) of CMB field CMB-1 (the observing field closest to the Galactic center that QUIET observes), no statistically significant foreground contamination is detected. The foreground measurements performed by the QUIET experiment are the most sensitive measurements of polarized emission made in low emission fields to date.

Field	Spectrum	$\hat{\mathcal{C}}_{\ell=50}^{\mathrm{KK}}$	$\hat{\mathcal{C}}_{\ell=50}^{\mathrm{QK}}$	$\hat{\mathcal{C}}_{\ell=50}^{\mathrm{QQ}}$
CMB-1	EE	$\mathbf{17.4 \pm 4.7}$	$\mathbf{3.30 \pm 0.55}$	$\mathbf{0.55 \pm 0.14}$
	BB	4.8 ± 4.5	0.40 ± 0.41	0.06 ± 0.08
CMB-2	EE	5.5 ± 3.7	0.01 ± 0.56	0.23 ± 0.19
	BB	4.6 ± 3.4	0.18 ± 0.48	-0.11 ± 0.13
CMB-3	EE	0.2 ± 1.9	0.64 ± 0.43	0.10 ± 0.18
	BB	-0.3 ± 2.6	0.33 ± 0.35	0.01 ± 0.13
CMB-4	EE	-5.2 ± 5.1	0.7 ± 1.2	0.65 ± 0.58
	BB	-2.6 ± 5.2	-0.1 ± 1.1	-0.37 ± 0.52

Table 6.3: Band and Cross Powers for the $\ell = 50$ bin (averaged over $\ell = 25$–75) – Power-spectra estimates for the $\ell = 50$ multipole bin for each patch, computed from the WMAP 7-year K-band data and the QUIET Q-band data. The units are $\ell(\ell+1)\mathcal{C}_\ell/2\pi$ ($\mu\mathrm{K}^2$) in thermodynamic temperature. The $\hat{\mathcal{C}}_\ell^{KK}$ and $\hat{\mathcal{C}}_\ell^{QK}$ spectra are respectively calculated by processing the WMAP 7-year K-band data and the cross-spectra of the WMAP 7-year K-band data with the QUIET Q-band data through the QUIET analysis pipeline. The $\hat{\mathcal{C}}_\ell^{QQ}$ spectrum is obtained from QUIET Q-band data. Uncertainties for $\hat{\mathcal{C}}_{\ell=50}^{KK}$ and $\hat{\mathcal{C}}_{\ell=50}^{QK}$ include noise only. For $\hat{\mathcal{C}}_{\ell=50}^{QQ}$ they additionally include CMB sample variance as predicted by ΛCDM. Values in bold are more than $2\,\sigma$ away from zero.

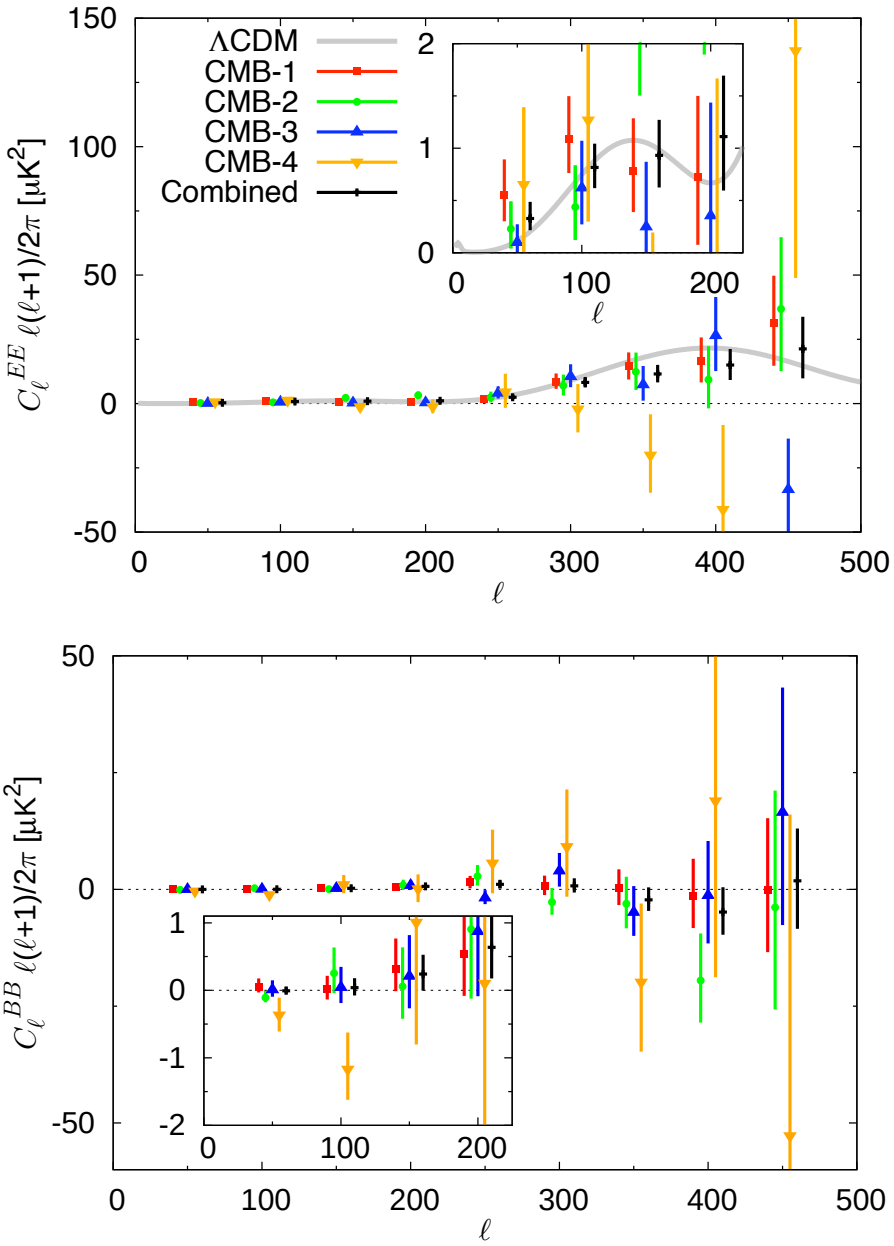

Figure 6.10: CMB power spectra are shown for each CMB field individually. The top and bottom panels show the E-mode and B-mode spectra, respectively. The different error bars for each CMB field mainly reflect the amounts of time each was observed. The theoretical Λ-CDM curve is also shown for the E-mode power spectrum [44]. Both figures courtesy of Immanuel Buder.

6.3 Conclusions and Future Work

The QUIET Q-band observing season (2008 October – 2009 June) consists of 2668 hours of CMB field observations. The 27.3′ beam size (angular resolution) of the Q-band QUIET receiver enables multipole power spectrum measurements in the ℓ range $25 < \ell < 475$, and produced some of the most accurate E- and B- mode power spectrum results to date: the QUIET team confirmed the only previous detection of the first acoustic peak of the E-mode spectrum; set competitive upper limits on the B-mode spectrum ($r = 0.52^{+0.97}_{-0.81}$, with an upper limit on r of 2.4 at 95% confidence); and constrained foregrounds in the four CMB observing fields which QUIET observes. These results were published to the arXiv in December of 2010 and were accepted for publication in *The Astrophysical Journal* in July of 2011.

The QUIET W-band observing season (2009 August – 2010 December) consists of 5367 hours of CMB observations. The 12.2′ beam size of the W-band receiver will enable multipole power spectrum measurements in the ℓ range of $25 \simeq \ell \simeq 1000$. At the time of writing, data analysis is underway, with the intent to publish before the end of the 2011 calendar year. A phase II QUIET telescope, consisting of 500-1500 polarimeters, is also planned.

Bibliography

[1] Capo, F., [*It Happened in New Jersey*], It happened in series, Globe Peguot Press (2003).

[2] Mather, J. C., Cheng, E. S., Cottingham, D. A., Eplee, Jr., R. E., Fixsen, D. J., Hewagama, T., Isaacman, R. B., Jensen, K. A., Meyer, S. S., Noerdlinger, P. D., Read, S. M., Rosen, L. P., Shafer, R. A., Wright, E. L., Bennett, C. L., Boggess, N. W., Hauser, M. G., Kelsall, T., Moseley, Jr., S. H., Silverberg, R. F., Smoot, G. F., Weiss, R., and Wilkinson, D. T., "Measurement of the cosmic microwave background spectrum by the COBE FIRAS instrument," *Astrophysical Journal* **420**, 439–444 (Jan. 1994).

[3] Smoot, G. F., Bennett, C. L., Kogut, A., Wright, E. L., Aymon, J., Boggess, N. W., Cheng, E. S., de Amici, G., Gulkis, S., Hauser, M. G., Hinshaw, G., Jackson, P. D., Janssen, M., Kaita, E., Kelsall, T., Keegstra, P., Lineweaver, C., Loewenstein, K., Lubin, P., Mather, J., Meyer, S. S., Moseley, S. H., Murdock, T., Rokke, L., Silverberg, R. F., Tenorio, L., Weiss, R., and Wilkinson, D. T., "Structure in the COBE dif-

ferential microwave radiometer first-year maps," *Astrophysical Journal Letters* **396**, L1–L5 (Sept. 1992).

[4] Miller, A. D., Caldwell, R., Devlin, M. J., Dorwart, W. B., Herbig, T., Nolta, M. R., Page, L. A., Puchalla, J., Torbet, E., and Tran, H. T., "A Measurement of the Angular Power Spectrum of the Cosmic Microwave Background from L = 100 to 400," *Astrophysical Journal Letters* **524**, L1–L4 (Oct. 1999).

[5] Runyan, M. C., Ade, P. A. R., Bock, J. J., Bond, J. R., Cantalupo, C., Contaldi, C. R., Daub, M. D., Goldstein, J. H., Gomez, P. L., Holzapfel, W. L., Kuo, C. L., Lange, A. E., Lueker, M., Newcomb, M., Peterson, J. B., Pogosyan, D., Romer, A. K., Ruhl, J., Torbet, E., and Woolsey, D., "First results from the arcminute cosmology bolometer array receiver," *New Astronomy Review* **47**, 915–923 (Dec. 2003).

[6] Ruhl, J. E., Ade, P. A. R., Bock, J. J., Bond, J. R., Borrill, J., Boscaleri, A., Contaldi, C. R., Crill, B. P., de Bernardis, P., De Troia, G., Ganga, K., Giacometti, M., Hivon, E., Hristov, V. V., Iacoangeli, A., Jaffe, A. H., Jones, W. C., Lange, A. E., Masi, S., Mason, P., Mauskopf, P. D., Melchiorri, A., Montroy, T., Netterfield, C. B., Pascale, E., Piacentini, F., Pogosyan, D., Polenta, G., Prunet, S., and Romeo, G., "Improved Measurement of the Angular Power Spectrum of Temperature Anisotropy in the Cosmic Microwave Background from Two New Analyses of BOOMERANG Observations," *Astrophysical Journal* **599**, 786–805 (Dec. 2003).

[7] Mason, B. S., Pearson, T. J., Readhead, A. C. S., Shepherd, M. C., Sievers, J., Udomprasert, P. S., Cartwright, J. K., Farmer, A. J., Padin, S., Myers, S. T., Bond,

J. R., Contaldi, C. R., Pen, U., Prunet, S., Pogosyan, D., Carlstrom, J. E., Kovac, J., Leitch, E. M., Pryke, C., Halverson, N. W., Holzapfel, W. L., Altamirano, P., Bronfman, L., Casassus, S., May, J., and Joy, M., "The Anisotropy of the Microwave Background to l = 3500: Deep Field Observations with the Cosmic Background Imager," *Astrophysical Journal* **591**, 540–555 (July 2003).

[8] Jarosik, N., Bennett, C. L., Dunkley, J., Gold, B., Greason, M. R., Halpern, M., Hill, R. S., Hinshaw, G., Kogut, A., Komatsu, E., Larson, D., Limon, M., Meyer, S. S., Nolta, M. R., Odegard, N., Page, L., Smith, K. M., Spergel, D. N., Tucker, G. S., Weiland, J. L., Wollack, E., and Wright, E. L., "Seven-year Wilkinson Microwave Anisotropy Probe (WMAP) Observations: Sky Maps, Systematic Errors, and Basic Results," *Astrophysical Journal Supplement* **192**, 14–+ (Feb. 2011).

[9] Liddle, A., [*An Introduction to Modern Cosmology, Second Edition*], Wiley (May 2003).

[10] Guth, A. H., "Inflationary universe: A possible solution to the horizon and flatness problems," *Physical Review D* **23**, 347–356 (Jan. 1981).

[11] Baumann, D., Jackson, M. G., Adshead, P., Amblard, A., Ashoorioon, A., Bartolo, N., Bean, R., Beltrán, M., de Bernardis, F., Bird, S., Chen, X., Chung, D. J. H., Colombo, L., Cooray, A., Creminelli, P., Dodelson, S., Dunkley, J., Dvorkin, C., Easther, R., Finelli, F., Flauger, R., Hertzberg, M. P., Jones-Smith, K., Kachru, S., Kadota, K., Khoury, J., Kinney, W. H., Komatsu, E., Krauss, L. M., Lesgourgues, J., Liddle, A., Liguori, M., Lim, E., Linde, A., Matarrese, S., Mathur, H., McAllister,

L., Melchiorri, A., Nicolis, A., Pagano, L., Peiris, H. V., Peloso, M., Pogosian, L., Pierpaoli, E., Riotto, A., Seljak, U., Senatore, L., Shandera, S., Silverstein, E., Smith, T., Vaudrevange, P., Verde, L., Wandelt, B., Wands, D., Watson, S., Wyman, M., Yadav, A., Valkenburg, W., and Zaldarriaga, M., "Probing Inflation with CMB Polarization," in [*American Institute of Physics Conference Series*], S. Dodelson, D. Baumann, A. Cooray, J. Dunkley, A. Fraisse, M. G. Jackson, A. Kogut, L. Krauss, M. Zaldarriaga, & K. Smith , ed., *American Institute of Physics Conference Series* **1141**, 10–120 (June 2009).

[12] Liddle, A. R. and Lyth, D. H., [*Cosmological Inflation and Large-Scale Structure*], Cambridge University Press (Apr. 2000).

[13] Natarajan, A. and Schwarz, D. J., "Distinguishing standard reionization from dark matter models," *Physical Review D* **81**, 123510 (Jun 2010).

[14] Sachs, R. K. and Wolfe, A. M., "Perturbations of a Cosmological Model and Angular Variations of the Microwave Background," *Astrophysical Journal* **147**, 73–+ (Jan. 1967).

[15] Hu, W. and White, M., "A CMB polarization primer," *New Astronomy* **2**, 323–344 (Oct. 1997).

[16] Bennett, C. L., Hill, R. S., Hinshaw, G., Nolta, M. R., Odegard, N., Page, L., Spergel, D. N., Weiland, J. L., Wright, E. L., Halpern, M., Jarosik, N., Kogut, A., Limon, M., Meyer, S. S., Tucker, G. S., and Wollack, E., "First-Year Wilkin-

son Microwave Anisotropy Probe (WMAP) Observations: Foreground Emission," *Astrophysical Journal Supplement* **148**, 97–117 (Sept. 2003).

[17] Kovac, J. M., Leitch, E. M., Pryke, C., Carlstrom, J. E., Halverson, N. W., and Holzapfel, W. L., "Detection of polarization in the cosmic microwave background using DASI," *Nature* **420**, 772–787 (Dec. 2002).

[18] Chiang, H. C., Ade, P. A. R., Barkats, D., Battle, J. O., Bierman, E. M., Bock, J. J., Dowell, C. D., Duband, L., Hivon, E. F., Holzapfel, W. L., Hristov, V. V., Jones, W. C., Keating, B. G., Kovac, J. M., Kuo, C. L., Lange, A. E., Leitch, E. M., Mason, P. V., Matsumura, T., Nguyen, H. T., Ponthieu, N., Pryke, C., Richter, S., Rocha, G., Sheehy, C., Takahashi, Y. D., Tolan, J. E., and Yoon, K. W., "Measurement of Cosmic Microwave Background Polarization Power Spectra from Two Years of BICEP Data," *Astrophysical Journal* **711**, 1123–1140 (Mar. 2010).

[19] Castro, P. G., Ade, P., Bock, J., Bowden, M., Brown, M. L., Cahill, G., Church, S., Culverhouse, T., Friedman, R. B., Ganga, K., Gear, W. K., Gupta, S., Hinderks, J., Kovac, J., Lange, A. E., Leitch, E., Melhuish, S. J., Memari, Y., Murphy, J. A., Orlando, A., Pryke, C., Schwarz, R., O'Sullivan, C., Piccirillo, L., Rajguru, N., Rusholme, B., Taylor, A. N., Thompson, K. L., Turner, A. H., Wu, E. Y. S., Zemcov, M., and The QUa D collaboration, "Cosmological Parameters from the QUAD CMB Polarization Experiment," *Astrophysical Journal* **701**, 857–864 (Aug. 2009).

[20] Mauskopf, P. D., Ade, P. A. R., de Bernardis, P., Bock, J. J., Borrill, J., Boscaleri, A., Crill, B. P., DeGasperis, G., De Troia, G., Farese, P., Ferreira, P. G., Ganga,

K., Giacometti, M., Hanany, S., Hristov, V. V., Iacoangeli, A., Jaffe, A. H., Lange, A. E., Lee, A. T., Masi, S., Melchiorri, A., Melchiorri, F., Miglio, L., Montroy, T., Netterfield, C. B., Pascale, E., Piacentini, F., Richards, P. L., Romeo, G., Ruhl, J. E., Scannapieco, E., Scaramuzzi, F., Stompor, R., and Vittorio, N., "Measurement of a Peak in the Cosmic Microwave Background Power Spectrum from the North American Test Flight of Boomerang," *Astrophysical Journal Letters* **536**, L59–L62 (June 2000).

[21] Page, L., Hinshaw, G., Komatsu, E., Nolta, M. R., Spergel, D. N., Bennett, C. L., Barnes, C., Bean, R., Doré, O., Dunkley, J., Halpern, M., Hill, R. S., Jarosik, N., Kogut, A., Limon, M., Meyer, S. S., Odegard, N., Peiris, H. V., Tucker, G. S., Verde, L., Weiland, J. L., Wollack, E., and Wright, E. L., "Three-Year Wilkinson Microwave Anisotropy Probe (WMAP) Observations: Polarization Analysis," *Astrophysical Journal Supplement* **170**, 335–376 (June 2007).

[22] Bischoff, C., Hyatt, L., McMahon, J. J., Nixon, G. W., Samtleben, D., Smith, K. M., Vanderlinde, K., Barkats, D., Farese, P., Gaier, T., Gundersen, J. O., Hedman, M. M., Staggs, S. T., and Winstein, B., "New Measurements of Fine-Scale CMB Polarization Power Spectra from CAPMAP at Both 40 and 90 GHz," *Astrophysical Journal* **684**, 771–789 (Sept. 2008).

[23] Brown, M. L., Ade, P., Bock, J., Bowden, M., Cahill, G., Castro, P. G., Church, S., Culverhouse, T., Friedman, R. B., Ganga, K., Gear, W. K., Gupta, S., Hinderks, J., Kovac, J., Lange, A. E., Leitch, E., Melhuish, S. J., Memari, Y., Murphy, J. A., Orlando, A., O'Sullivan, C., Piccirillo, L., Pryke, C., Rajguru, N., Rusholme, B.,

Schwarz, R., Taylor, A. N., Thompson, K. L., Turner, A. H., Wu, E. Y. S., Zemcov, M., and The QUa D collaboration, "Improved Measurements of the Temperature and Polarization of the Cosmic Microwave Background from QUaD," *Astrophysical Journal* **705**, 978–999 (Nov. 2009).

[24] Larson, D., Dunkley, J., Hinshaw, G., Komatsu, E., Nolta, M. R., Bennett, C. L., Gold, B., Halpern, M., Hill, R. S., Jarosik, N., Kogut, A., Limon, M., Meyer, S. S., Odegard, N., Page, L., Smith, K. M., Spergel, D. N., Tucker, G. S., Weiland, J. L., Wollack, E., and Wright, E. L., "Seven-year Wilkinson Microwave Anisotropy Probe (WMAP) Observations: Power Spectra and WMAP-derived Parameters," *Astrophysical Journal Supplement* **192**, 16–+ (Feb. 2011).

[25] Padin, S., Shepherd, M. C., Cartwright, J. K., Keeney, R. G., Mason, B. S., Pearson, T. J., Readhead, A. C. S., Schaal, W. A., Sievers, J., Udomprasert, P. S., Yamasaki, J. K., Holzapfel, W. L., Carlstrom, J. E., Joy, M., Myers, S. T., and Otarola, A., "The Cosmic Background Imager," *Publications of the ASP* **114**, 83–97 (Jan. 2002).

[26] Chang, S. and Prata, A., "The Design of Classical Offset Dragonian Reflector Antennas With Circular Apertures," *IEEE Transactions on Antennas and Propagation* **52**, 12–19 (Jan. 2004).

[27] Hecht, E., [*Optics 4th edition*], Addison Wesley (2001).

[28] Pozar, D. M., [*Microwave Engineering*], Wiley, 2nd ed. (2004).

[29] Garand, L. and others, "Radiance and Jacobian intercomparison of radiative transfer models applied to HIRS and AMSU channels," *Journal of Geophysical Research* **106**(D20), 24,017–24,031 (2001).

[30] Hill, R. S., Weiland, J. L., Odegard, N., Wollack, E., Hinshaw, G., Larson, D., Bennett, C. L., Halpern, M., Page, L., Dunkley, J., Gold, B., Jarosik, N., Kogut, A., Limon, M., Nolta, M. R., Spergel, D. N., Tucker, G. S., and Wright, E. L., "Five-Year Wilkinson Microwave Anisotropy Probe Observations: Beam Maps and Window Functions," *Astrophysical Journal Supplement* **180**, 246–264 (Feb. 2009).

[31] Smith, C. H., Bourke, T. L., Wright, C. M., Spoon, H. W. W. S., Aitken, D. K., Robinson, G., Storey, J. W. V., Fujiyoshi, T., Roche, P. F., and Lehmann, T., "Mid-infrared imaging and spectroscopy of the southern HII region RCW 38," *Monthly Notices of the RAS* **303**, 367–379 (Feb. 1999).

[32] Hafez, Y. A., Davies, R. D., Davis, R. J., Dickinson, C., Battistelli, E. S., Blanco, F., Cleary, K., Franzen, T., Genova-Santos, R., Grainge, K., Hobson, M. P., Jones, M. E., Lancaster, K., Lasenby, A. N., Padilla-Torres, C. P., Rubino-Martin, J. A., Rebolo, R., Saunders, R. D. E., Scott, P. F., Taylor, A. C., Tittering ton, D., Tucci, M., and Watson, R. A., "Radio source calibration for the VSA and other CMB instruments at around 30 GHz," *ArXiv e-prints* (Apr. 2008).

[33] Weiland, J. L., Odegard, N., Hill, R. S., Wollack, E., Hinshaw, G., Greason, M. R., Jarosik, N., Page, L., Bennett, C. L., Dunkley, J., Gold, B., Halpern, M., Kogut, A., Komatsu, E., Larson, D., Limon, M., Meyer, S. S., Nolta, M. R., Smith,

K. M., Spergel, D. N., Tucker, G. S., and Wright, E. L., "Seven-year Wilkinson Microwave Anisotropy Probe (WMAP) Observations: Planets and Celestial Calibration Sources," *Astrophysical Journal Supplement* **192**, 19–+ (Feb. 2011).

[34] Aumont, J., Conversi, L., Thum, C., Wiesemeyer, H., Falgarone, E., Macías-Pérez, J. F., Piacentini, F., Pointecouteau, E., Ponthieu, N., Puget, J. L., Rosset, C., Tauber, J. A., and Tristram, M., "Measurement of the Crab nebula polarization at 90 GHz as a calibrator for CMB experiments," *Astronomy & Astrophysics* **514**, A70+ (May 2010).

[35] Bischoff, C. A., *Observing the Cosmic Microwave Background polarization anisotropy at 40 GHz with QUIET*, PhD thesis, The University of Chicago (2010).

[36] Newburgh, L. B., *The Q/U Imaging ExperimenT (QUIET): The Q-band Receiver Array Instrument and Observations*, PhD thesis, Columbia University (2010).

[37] Kraus, J. D., [*Radio astronomy*], Cygnus-Quasar Books (1986).

[38] Dumoulin, R. N., "Responsivity calibration of the QUIET Q-Band array," in [*Society of Photo-Optical Instrumentation Engineers (SPIE) Conference Series*], *Presented at the Society of Photo-Optical Instrumentation Engineers (SPIE) Conference* **7741** (July 2010).

[39] Paine, S., "The am Atmospheric Model SMA Technical Memo 152, Revision 3," (2004). http://www.cfa.harvard.edu/sma/memos/152-03.pdf.

[40] Ruze, J., "The effect of aperture errors on the antenna radiation pattern," *Nuovo Cimento* **9** (1953).

[41] Tegmark, M., "How to Make Maps from Cosmic Microwave Background Data without Losing Information," *Astrophysical Journal Letters* **480**, L87+ (May 1997).

[42] Keskitalo, R., Ashdown, M. A. J., Cabella, P., Kisner, T., Poutanen, T., Stompor, R., Bartlett, J. G., Borrill, J., Cantalupo, C., de Gasperis, G., de Rosa, A., de Troia, G., Eriksen, H. K., Finelli, F., Górski, K. M., Gruppuso, A., Hivon, E., Jaffe, A., Keihänen, E., Kurki-Suonio, H., Lawrence, C. R., Natoli, P., Paci, F., Polenta, G., and Rocha, G., "Residual noise covariance for Planck low-resolution data analysis," *Astronomy & Astrophysics* **522**, A94+ (Nov. 2010).

[43] Bond, J. R., Jaffe, A. H., and Knox, L., "Estimating the power spectrum of the cosmic microwave background," *Physical Review D* **57**, 2117–2137 (Feb. 1998).

[44] QUIET Collaboration, Bischoff, C., Brizius, A., Buder, I., Chinone, Y., Cleary, K., Dumoulin, R. N., Kusaka, A., Monsalve, R., Næss, S. K., Newburgh, L. B., Reeves, R., Smith, K. M., Wehus, I. K., Zuntz, J. A., Zwart, J. T. L., Bronfman, L., Bustos, R., Church, S. E., Dickinson, C., Eriksen, H. K., Ferreira, P. G., Gaier, T., Gundersen, J. O., Hasegawa, M., Hazumi, M., Huffenberger, K. M., Jones, M. E., Kangaslahti, P., Kapner, D. J., Lawrence, C. R., Limon, M., May, J., McMahon, J. J., Miller, A. D., Nguyen, H., Nixon, G. W., Pearson, T. J., Piccirillo, L., Radford, S. J. E., Readhead, A. C. S., Richards, J. L., Samtleben, D., Seiffert, M., Shepherd, M. C., Staggs, S. T., Tajima, O., Thompson, K. L., Vanderlinde, K., Williamson, R., and Winstein, B., "First Season QUIET Observations: Measurements of CMB Polarization Power Spectra at 43 GHz in the Multipole Range $25 \leqslant \ell \leqslant 475$," *ArXiv e-prints* (Dec. 2010).

[45] Gold, B., Odegard, N., Weiland, J. L., Hill, R. S., Kogut, A., Bennett, C. L., Hinshaw, G., Chen, X., Dunkley, J., Halpern, M., Jarosik, N., Komatsu, E., Larson, D., Limon, M., Meyer, S. S., Nolta, M. R., Page, L., Smith, K. M., Spergel, D. N., Tucker, G. S., Wollack, E., and Wright, E. L., "Seven-year WMAP catalog (Gold+, 2011)," *VizieR Online Data Catalog* **219**, 20015–+ (Mar. 2011).

[46] Dunkley, J., Spergel, D. N., Komatsu, E., Hinshaw, G., Larson, D., Nolta, M. R., Odegard, N., Page, L., Bennett, C. L., Gold, B., Hill, R. S., Jarosik, N., Weiland, J. L., Halpern, M., Kogut, A., Limon, M., Meyer, S. S., Tucker, G. S., Wollack, E., and Wright, E. L., "Five-Year Wilkinson Microwave Anisotropy Probe (WMAP) Observations: Bayesian Estimation of Cosmic Microwave Background Polarization Maps," *The Astrophysical Journal* **701**, 1804–1813 (Aug. 2009).